1225-0767(ISSN Print)
2287-6715(ISSN Online)
한국연구재단 우수등재학술지

Journal of Ocean Engineering and Technology

Vol. 35, No. 6 (Serial Number 163) December 2021

한국해양공학회지

KSOE

www.joet.org

KSOE The Korean Society of Ocean Engineers

Journal of Ocean Engineering and Technology
한국해양공학회지
Vol. 35 No. 6
(Serial Number 163)
December 31, 2021
www.JOET.org

Editorial Board

Research and Publication Ethics Committee

Published on December 31, 2021
Published by The Korean Society of Ocean Engineers (KSOE)
Room 1302, 13, Jungang-daero 180beon-gil, Dong-gu, Busan, 48821, Korea
TEL: +82-51-759-0656 FAX: +82-51-759-0657 E-mail: ksoehj@ksoe.or.kr URL: http://www.ksoe.or.kr
Printed by Hanrimwon Co., Ltd., Seoul, Korea E-mail: hanrim@hanrimwon.co.kr
ISSN(print) 1225-0767 **ISSN(online)** 2287-6715

This journal was supported by the Korean Federation of Science and Technology Societies (KOFST) grant funded by the Korean government.

Journal of Ocean Engineering and Technology
한국해양공학회지

CONTENTS

Volume 35, Number 6 December, 2021

<Original Research Articles>

<Technical Article>

GENERAL INFORMATION

"Journal of Ocean Engineering and Technology" is the official journal published by "The Korean Society of Ocean Engineers (KSOE)". The ISO abbreviation is "J. Ocean Eng. Technol." and acronym is "**JOET**". It was launched in 1987. It is published bimonthly in February, April, June, August, October, and December each year. Supplement numbers are published at times.

Journal of Ocean Engineering and Technology (JOET) is a medium for the publication of original research and development work in the field of ocean engineering. JOET covers the entire range of issues and technologies related to the following topics:

Ships and offshore platforms: Design of marine structures; Resistance and propulsion; Seekeeping and maneuvering; Experimental and computational fluid dynamics; Ocean wave mechanics; Fatigue strength; Plasticity; Optimization and reliability; Arctic technology and extreme mechanics; Noise, vibration, and acoustics; Concrete engineering; Thermodynamics and heat transfer; Hydraulics and pneumatics;
Coastal civil engineering: Coastal structures; Port and harbor structures; Soil mechanics; Drilling and exploration; Hydraulics of estuary; Seismic engineering; Coastal disaster prevention engineering;
Ocean renewable energy platforms: Offshore wind turbines; Wave energy platforms; Tidal current energy platforms; Floating photovoltaic energy platforms;
Marine robots: Robot sensor system; Autonomous navigation; Robot equipments; Spatial information and communications; Underwater network; Design of underwater vehicles;
Multidisciplinary areas: Design for safety; IT-based design; IT-based production engineering; Welding mechanics; Control engineering; GPS and GIS; Inspection and sensor; Port and logistics; Leisure boat and deep see water; Offshore process systems engineering; Marine metallic materials; Marine organic materials; Marine Composite materials; Materials properties; Corrosion and Anti-corrosion; Tribology;

It contains original research articles, case reports, brief communications and reviews on technial issues. Conference papers, research papers, diploma papers and academic articles can be submitted.

All of the manuscripts are peer-reviewed. **JOET** has a system where two or more peer reviewers must review each submitted paper and it is operated very strictly.

JOET is being indexed in some prominent database such as Korean Citatation Index (KCI), Google Scholar, Science Central, Korea Science and Directory of Open Access Journals (DOAJ).

For correspondences concerning business matters, author needs to contact KSOE Secretariat by email or phone (e-mail: ksoehj@ksoe.or.kr or Tel: +82 51 759 0656). Correspondences for publication matters can be asked via email to the Editor-in-Chief (email: heroeswise2@gmail.com).

KSOE

Journal of Ocean Engineering and Technology 35(6), 393-402, December, 2021
https://doi.org/10.26748/KSOE.2021.071

pISSN 1225-0767
eISSN 2287-6715

Original Research Article

Greenhouse Gas Emission Analysis by LNG Fuel Tank Size through Life Cycle

Eunyoung Park[1] and Jungho Choi[2]

[1]*Researcher, Offshore Industries R&BD Center, Korea Research Institute of Ships&Ocean Engineering, Geoje, Korea*
[2]*Professor, Department of Naval Architecture and Offshore Engineering, Dong-A University, Busan, Korea*

KEY WORDS: LNG bunkering, Greenhouse gas emission, LNG fuel tank, Life cycle, CO_2 emission

ABSTRACT: *As greenhouse gas emissions from maritime transport are increasing, the International Maritime Organization is continuously working to strengthen emission regulations. Liquefied natural gas (LNG) fuel is less advantageous as a point of CO_2 reduction due to the methane leakage that occurs during the bunkering and operation of marine engines. In this study, greenhouse gas emissions from an LNG-fueled ship were analyzed from the perspective of the life cycle. The amount ofmethane emission during the bunkering and operation procedures with various boil-off gas (BOG) treatment methods and gas engine specifications was analyzed by dynamic simulation. The results were also compared with those of other liquid fuel engines. As a result, small LNG-fueled ships without a BOG treatment facility emitted 32% more greenhouse gas than ships utilizing marine gas oil or heavy fuel oil. To achieve a greenhouse gas reduction via a BOG treatment method, a gas combustion unit or re-liquefaction system must be mounted, which results in a greenhouse gas reduction effect of about 25% and 30%. As a result of comparing the amount of greenhouse gas generated according to the BOG treatment method used with each tank size from the perspective of the operating cycle with the amounts from using existing marine fuels, the BOG treatment method showed superior effects of greenhouse gas reduction.*

1. Introduction

With global economic growth, the number of cargo ships required for maritime transportation has increased, resulting in a larger problem of greenhouse gas (GHG) emissions. As the maritime transport sector has become a significant contributor to global GHG emissions, the International Maritime Organization, which is responsible for environmental regulations, has made continuous efforts to reduce GHG emissions from ships (Wada et al., 2021). The Marine Environment Protection Committee (MEPC) has reviewed the emission regulations, including the Energy Efficiency Design Index (EEDI), Energy Efficiency Operating Indicator (EEOI), Energy Efficiency Existing-ship Index (EEXI), Energy Efficiency Performance Indicator (EEPI), and Ship Energy Efficiency Management Plan (SEEMP), and also simultaneously discussed the environmentally friendly frameworks for cargo ships (Ahn et al., 2021).

Liquefied natural gas (LNG) is an environmentally friendly fuel with the unique benefit of reducing CO_2 emissions by 10–20% (Lee et al., 2020). However, the use of LNG as a ship fuel necessitates the process of bunkering, and treatment of boil-off gas (BOG) during bunkering is essential. The currently available BOG treatment methods are venting, use of a gas combustion unit (GCU), and re-liquefaction.

However, BOG treatment or the transport of LNG as an environmentally friendly fuel entails increased methane emissions, although the emissions of conventional pollutants such as NOx and SOx are reduced (Yu et al., 2020). Compared to CO_2, methane leads to an approximately 25-fold higher GHG effect due to its high global warming potential (GWP) (Jang et al., 2021). Despite efforts to minimize the release of methane into the atmosphere, the following scenarios of potential leakage are possible (Herdzik, 2018).

(1) Pipeline leakage upon connection or separation during the LNG loading/unloading operations
(2) Leakage from the LNG tank during BOG removal
(3) Leakage through the liquefaction system in operation during loading or sailing
(4) Leakage during the gas-freeing operation inside the LNG tank
(5) Leakage during LNG bunkering
(6) Leakage by incomplete combustion when dual fueling or using LNG as fuel

Therefore, the methane emission throughout the entire LNG supply network or the ship engine exhaust gas offsets the benefits of using LNG and makes LNG a less desirable alternative to marine gas oil

Received 23 September 2021, revised 15 October 2021, accepted 25 October 2021
Corresponding author Jungho Choi : +82-51-200-7938, tamnuchoi@dau.ac.kr

(MGO). In other words, the advantages of LNG as an environmentally friendly fuel are reduced (Edfors and Bremberg, 2021). Therefore, it is important to compare the use of LNG fuel with the use of conventional marine fuels in terms of GHG emissions (Winnes and Fridell, 2009). Moreover, the effects of emissions related to marine fuel processing, its GHG emissions, and their correlations should be examined.

From the perspective of the LNG-fueled ships, this study considered the integration of bunkering and operation processes and identified the environmental indicators using for making comparisons with conventional fuels. Indicators for comparison between different fuels need to be provided to enable ship owners and operators to determine potentials on demand. If the perspective is extended to include ship bunkering and operation, the results are likely to be more complex than other conventional results, i.e., follow-up studies with a wider scope and case studies may be required.

Numerous studies have investigated the gases directly emitted by ships. Chang et al. (2013) estimated the GHG emissions by ship type based on the data of the ships treated at ports, taking an approach relying on the characteristics of individual ships. Styhre et al. (2017) analyzed the level of GHG emissions for ships at ports based on annual port data. They also presented the results of dynamic modelling in addition to the actual field measurements. Shao et al. (2018) simulated the influence of temperature variation in the bunkering of LNG-fueled ships on the production of BOG. Shao et al. (2019) used dynamic simulation to identify the optimum ship-to-ship bunkering time and provided a reference guideline of bunkering to minimize BOG production. Lee et al. (2020) performed dynamic simulation to estimate the collected amount of BOG produced during ship-to-ship LNG bunkering and assessed the contribution of each parameter, including temperature variation, transportation rate, and pipe insulation performance. By combining the approaches of the two previously described studies, several simulations and cycle assessments have been conducted to suggest useful environmental indicators. Ryste (2012) applied the screening life cycle assessment (LCA) technique to determine the range of the LNG life cycle and establish the LNG value chain in the interpretation of climate change and related environmental issues. El-Houjeiri et al. (2019) applied the LCA approach to conduct an environmental assessment of the liquefaction, transportation, and re-liquefaction of LNG. Beyond ships, Arteconi et al. (2010) used the LCA approach in an investigation of trailers on land to make a life cycle comparison from the aspects of GHG emissions from diesel and LNG engines.

Nevertheless, there is a general paucity of studies on the long-term assessment of measures for reducing GHG emissions. The prediction of GHG emissions mandates prediction, from operational perspectives, beginning from the preparation stage of fuel use. Thus, indicators are required to determine whether LNG ship fuel is a practical solution in comparison with other fuels from environmental perspectives that complies with emission regulations.

Taking the aforementioned factors into consideration, this study investigated the GHG emissions from methane leakage during bunkering, the GHG emissions associated with the BOG treatment method, and the GHG emissions associated with engine use. The bunkering and operation processes of LNG-fueled ships were integrated so that environmental indicators of GHG emissions could be recommended for the entire life cycle depending on the size of the fuel tank. The results showed that the contribution varies according to fuel tank size, which distinguishes this study from previous studies as more specific conditions were used in this study to describe the GHG emissions that affect the environment from the perspective of ship operation.

2. Simulation Method

2.1 Determination of LNG Bunkering

Fig. 1 shows an overview of the process for the LNG bunkering scenario. The system consists of two LNG storage tanks (bunkering and receiving), an LNG pump, the bunkering pipeline, and the BOG pipeline (Jeong et al., 2017). The LNG pump transports the LNG loaded in the bunkering tank to the receiving tank. The pump as a transportation device is advantageous because it reduces LNG transport time (Sharafian et al., 2019). Safety valves are attached to

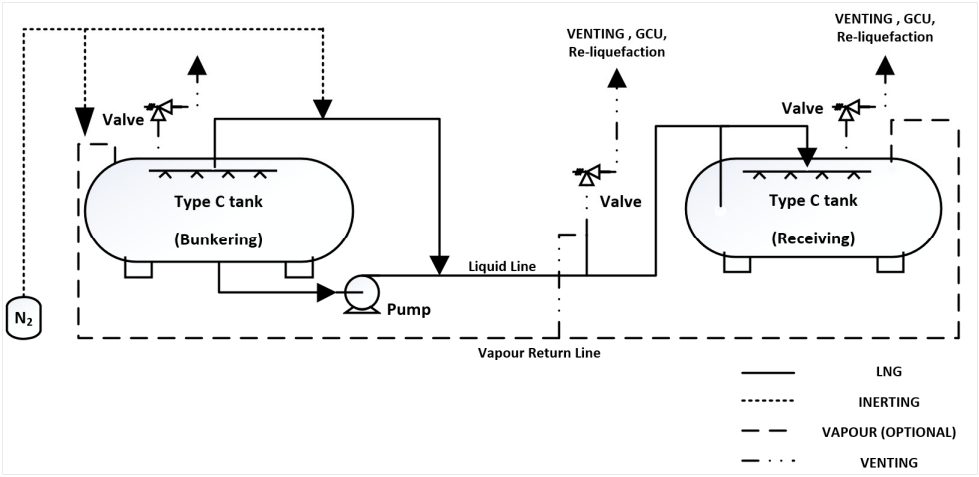

Fig. 1 Schematic of LNG tank-to-tank bunkering

prevent overpressure in the LNG tank, and the corresponding line leads to emission or treatment according to the BOG treatment method.

2.2 Tank Geometry

The fuel tanks eligible for LNG-fueled ships are listed in the International Gas Carrier (IGC) code and the International Code of Safety for Using Gases or Other Low-Flash-Point Fuels (IGF) code. In general, the Type C tank is used. The Type C tank has a maximum allowable working pressure (MAWP) of 700 kPa or higher and is thus regarded as a pressure container (Chorowski et al., 2015). The capacity of the bunkering tank is 500 m^3. The two receiving tanks may have different capacities of 500 m^3 and 1,000 m^3 (Kwak et al., 2018; Jung et al., 2018). Prior to bunkering, the levels of the bunkering tank and the receiving tank are 98% and 10%, respectively. The initial pressure in the bunkering tank is 300 kPa, and the initial temperature is −146.4℃. The pressure and temperature in the receiving tank are 101 kPa and −162.1℃.

The LNG inside the tank is stored at a very low temperature (approximately −160℃) and pressure (100−1,000 kPa). The main components of the LNG in the bunkering and receiving tanks are methane and light hydrocarbons (mainly C1−C4 hydrocarbons) in a mixture with N_2, as presented in Table 1 (Noh et al., 2014).

2.3 LNG Bunkering Pipeline

The LNG transport line connecting the bunkering tank and the receiving tank consists of the liquid line, the vapour return line, and the N_2 line. In the liquid line, transport is mediated through a loading arm or flexible hose (Wood and Kulitsa, 2018). The transport line is often connected to the quick-connect coupling (QC)/disconnect coupling (DC) and the emergency release coupling (ERC) to allow hose separation in an emergency. In addition, to prevent a loss of LNG, each separate section contains a disconnection valve for automatic shutdown. With the exception of the aforementioned devices, the transport line leads the flow of LNG through the pipeline, and the simulation considerate the flow velocity to prevent any additional surge pressure due to friction or cavitation (Lee et al., 2020). The single material of the pipe for transporting cryogenic LNG is stainless steel. The details are presented in Table 2 (Sharafian et al., 2019).

Table 1 Typical composition of natural gas (%)

Composition	Mole composition
Methane	94
Ethane	4.7
Propane	0.8
Butane	0.2
Nitrogen	0.3

Table 2 Specifications of liquid line and vapour return line

Buoy	Liquid line	Vapour return line
Diameter (mm)	200	100
Equivalent length (m)	29	25
Overall heat transfer coefficient, U pipe (W/m^2·℃)	0.0215	35.0
Initial temperature (℃)	25	

2.4 Greenhouse Gas (GHG) Emission by LNG Bunkering Procedure

For LNG bunkering operation, a detailed manual containing the operation procedures, safety and emergency protocols, and maintenance requirements should be provided. The manual should contain the procedures for inerting, gassing up, cooling down, pumping LNG, LNG spraying, vapour return management, draining, purging, and disconnecting, in addition to the validation and risk assessment procedures (Vairo et al., 2020). The procedure in this study was applied based on certain simplified steps of the aforementioned procedures and of the bunkering process suggested in the 2018 guideline of the European Maritime Safety Agency (EMSA). Table 3 describes the steps. The gas emission was interpreted for the loading, line purging, and operating of the IMP Type C tank.

For the loading in Step 1, transport to the receiving tank is performed, and heat ingress occurs due to the temperature difference of the external walls of the tank. The heat ingress through the tank wall causes the production of BOG and increases the tank pressure (Zincir and Dere, 2015). The BOG should be treated appropriately but difficulties exist. Venting, with the advantage of simple release to the atmosphere, could cause problems such as LNG fuel loss, environmental pollution, and increased risks of fire and explosion. Most LNG-fueled ships with the Type C tank lack the addition of a GCU as they are designed based on the concept of maintaining the pressure rise caused by heat ingress. The treatment of BOG using a GCU is problematic from an environmental perspective because the gas from the combustion is released to the atmosphere (Ryu et al., 2016). Moreover, ship owners may be reluctant to perform re-liquefaction, which demands extra space and an initial investment cost.

Data pertaining to CO_2 emission in the BOG treatment in LNG bunkering are insufficient, and the GHG effect is likely to be underestimated. In this study, the level of CO_2 emission according to the BOG treatment method was established through simulation. Venting releases BOG to the atmosphere to control the internal pressure of the tank. In reference to the guideline of the Intergovernmental Panel on Climate Change (IPCC), the 100-year GWP of CH_4 (the main component of BOG) is 25, indicating a 25-fold higher GHG effect than CO_2 (Penteado et al., 2012). The GWP

Table 3 Procedure of LNG bunkering operation

Step	Scenario
Step 1	Loading LNG from the bunkering tank to the fuel tank of the LNG fuelled ship
Step 2	Line purging the LNG bunkering line
Step 3	Operating LNG fuelled ship

indicates the global warming effect of a given GHG in comparison to the effect of CO_2 (Unseki, 2013). For consideration of venting, the GWP was converted to $Emission_{CO_2}$ (kg) using Eq. (1):

$$Emission_{CO_2} = GWP_{CH_4} \cdot m_{CH_4} \quad (1)$$

where GWP_{CH_4} is 25 in 100 years, and m_{CH_4} is the content (kg) of CH_4 in BOG.

In the case of a GCU, the gases are released to the atmosphere through complete combustion ($CH_4 + 2O_2 \rightarrow CO_2 + 2H_2O$) to prevent immediate emission of the GHG. For 1 mole of reactant CH_4, 1 mole of product CO_2 is produced (Dissanayake et al., 1991). The conversion to $Emission_{CO_2}$ (kg) according to Eq. (2) assumes complete combustion by the GCU:

$$Emission_{CO_2} = \frac{n_{CO_2}}{n_{CH_4}} \cdot M_{CO_2} \quad (2)$$

where n_{CO_2} is the number of moles of CO_2 (mol), n_{CH_4} is the number of moles of CH_4 (mol), and M_{CO_2} is the molecular mass of CO_2 (44.01 g/mol).

In the case of re-liquefaction, a technique to liquefy BOG for storage in the cargo tank, the N_2 cycle is used. The devices required for re-liquefaction are a power-supplied compressor, expander, and heat exchanger. The operation of these devices demands a power supply, and a certain amount of CO_2 is produced in the generation of the electricity. The amount of CO_2 produced in generating the power required by BOG re-liquefaction was calculated according to Eq. (3):

$$Emission_{CO_2} = EF_{electric} : SPC_{N_2 Cycle} \cdot m_{BOG} \quad (3)$$

where $SPC_{N_2\,Cycle}$ is the power consumption in using the N_2 cycle as the refrigerant cycle (1.44 kWh/kg_{BOG}), m_{BOG} is the mass of BOG (kg) (Kwak et al., 2018), and $EE_{electric}$ is the CO_2 emission index (0.466 kg CO_2/kWh) (Im et al., 2020).

In Step 2 of the procedure, line purging is the process that follows loading to the receiving tank. The pipe used for LNG loading should be detached from the system at the end of the operation. To remove residual LNG before detaching the pipe, substitution using inert gas is performed. The purging process is necessary for the safe removal of residual LNG, which is flammable and explosive. The release of LNG or NG from the pipe during this process has an effect on the GHG problem. Lowell et al. (2013) stated that there is no effective way to eliminate the methane leakage that occurs during the process, and a loss of approximately 0.03% occurs according to calculation based on the methane inside the tank. This methane can act as a powerful GHG. This study performed conversion according to Eq. (4):

$$Emission_{CO_2} = m_{CH_4} \cdot \rho_{LNG} \cdot GWP_{CH_4} \quad (4)$$

where m_{CH_4} and ρ_{LNG} are the mass of CH_4 inside the tank and the density of the loaded LNG, respectively, and GWP_{CH_4} is 25 in 100 years.

In Step 3, the operating process is the sailing of the LNG-fueled ship, which is equipped with a dual-fuel engine. Despite the use of environmentally friendly fuels, the engine $Emission_{CO_2}$ (kg) as a result of fuel consumption. The CO_2 emission for this step can be estimated using Eq. (5):

$$Emission_{CO_2} = EF_{Engine} \cdot P_{engine} \cdot t_{operating} \quad (5)$$

where P_{engine} is the output of the engine (kW), $t_{operating}$ is the time (h) of sailing of the ship using the fuel loaded in the tank, and EF_{engine} is an indicator of the CO_2 emission (g/kWh) for the respective engine.

BOG, which leads to the GHG effect, results from the combination of the following causes. In bunkering, CO_2 is produced in each procedure due to such varied causes as the heat ingress of the tank and other devices and water level fluctuation. In this study, a dynamic model was developed to analyze the influences of the causes in each procedure according to the amount and composition of the BOG. The GHG effect was estimated after conversion to the equivalent CO_2 emission.

3. Dynamic Simulation

3.1 Aspen Hysys Simulation of LNG Bunkering

Aspen Hysys is a chemical process simulator used in the mathematical modelling of a complete chemical process in unit operation. Hysys allows numerous core calculations of chemical engineering, including mass balance, energy balance, vapour–liquid equilibrium, heat transfer, mass transfer, mass fraction, and pressure drop (Naji et al., 2019). The thermodynamic interpretation of the process was based on the Peng–Robinson state Eqs. (6)–(11), which are known to lead to relatively accurate analyses of the thermodynamic properties of hydrocarbons, including LNG (Lee, 2017):

$$P = \frac{RT}{Vm-b} - \frac{a \circ \alpha}{Vm(Vm+b)+b(Vm-b)} \quad (6)$$

where the parameters a, α, b, and ω are defined as follows:

$$a = 0.45724 \frac{R^2 T_c^2}{P_c} \quad (7)$$

$$b = 0.07780 \frac{RT_c}{P_c} \quad (8)$$

$$\alpha = \left[1 + k\left(1 - T_r^{0.5}\right)\right]^2 \quad (9)$$

$$k = 0.37464 + 1.54226\omega - 0.26992\omega^2 \quad (10)$$

$$T_r = \frac{T}{T_c} \quad (11)$$

where P is pressure, T is temperature, R is the gas constant, and V_m is the mole volume. a and b indicate the energy parameter and the size parameter as a function of the critical temperature and pressure

3.2 LNG Bunkering Input Preparation

For LNG stored as a cryogenic liquid, heat ingress continuously induces BOG (Ryu et al., 2016). To incorporate the increase in vapour pressure inside the tank due to BOG in the modelling, the heat ingress was modeled using Eqs. (12) and (13) (Al-Breiki and Bicer, 2020). For dynamic simulation of the fuel tank, the tank model was constructed in consideration of the heat volume according to the water level (Cadafalch et al., 2015):

$$Q_1 = UA_{\tan k} \cdot (T_{ambient} - T_{\tan k}) \tag{12}$$

$$Q_2 = \frac{Tank\ level}{Tank\ present\ level} \cdot Q_1 \tag{13}$$

where Q_1 and Q_2 are heat ingress (kJ/s), U is the total heat transfer coefficient of each tank (W/m^2·℃), A is the area of tank (m^2), and $TRIANGLET$ is the difference between the surrounding temperature and the internal temperature of the tank (℃). Eq. (13) reflects the increase in heat ingress caused by the increase in the water level of the receiving tank, with 98% as the reference, while real-time changes are taken into account.

The causes of BOG include the increased water level in the tank, the heat ingress due to the input device, and the heat ingress through the pipe from the surrounding environment. The heat ingress due to the water level as the tank is being filled and the heat ingress through the pipe are reflected in Eq. (14):

$$Q_3 = UA_{pipe} \cdot (T_{ambient} - T_{pipe\_in}) \tag{14}$$

where Q_3 is the heat ingress (kJ/s), U is the total heat transfer coefficient of the transport pipeline (W/m^2·℃), A is the area of pipe (m^2), and $TRIANGLET$ is the difference between the surrounding temperature and the internal temperature of the pipe (℃).

The pump used to transport the LNG increases the pressure, and the mechanical energy transferred from the pump shaft is partially lost in the form of heat. The pressure conversion leads to heat ingress, as reflected in Eq. (15) (Lee et al., 2020).

$$Q_4 = \dot{W}_{actual} - \dot{W}_{ideal} = (1-\eta)\ \dot{m}\ (h_{out} - h_{in})_{pump} \tag{15}$$

In the equation, Q_4 is the heat ingress (kJ/s), $\dot{m}$ is the mass flow (kg/s), $(h_{out} - h_{in})_{pump}$ is the specific enthalpy (kJ/kg), and η indicates the efficiency of the pump. The heat ingress is incorporated as follows. The previously described Q_2, Q_3, and Q_4 correspond to the heat ingress that induces BOG, and these factors combine to have an effect on the BOG, which ultimately leads to the GHG effect. To transport the LNG, a pump, as a pressure increasing device, is used, and power is consumed as the cryogenic LNG is transported to the tank. As mentioned previously, a certain amount of CO_2 is produced through the power generation, and the required power supply causes GHG emission. The CO_2 emission via heat ingress of the pump is reflected in Eq. (16):

$$Emission_{CO_2} = P_{pump} \cdot t_{operating} \cdot Electric\ Emission\ Factor \tag{16}$$

where P_{pump} is the power consumed (kW), $t_{operating}$ is the pump operation time (h), and $Electric\ Emission\ Factor$ is the CO_2 emission index per generated power (0.466 kgCO_2/kWh) (Im et al., 2020).

4. Result

4.1 LNG Bunkering CO_2 Emission

Fig. 2 shows the properties of the tank with time through the bunkering process based on a receiving tank size of 500 m^3. The increases in water level and pressure accompanying the loading of LNG are apparent. The increased water level of the tank, pressure increasing device, and piping that induce heat ingress cause the overall heat ingress to increase.

Fig. 3 shows the pressure, heat ingress, and BOG flow according to time during bunkering. As bunkering progresses, the water level of the tank increases, resulting in an increase in the heat ingress related to the transport device and the heat ingress related to the increased water level. The production of BOG attributable to heat ingress thus increases the level of BOG, along with an increase in the internal pressure of the tank. If BOG treatment is not available during the loading of LNG to the receiving tank, the continuous increase in heat ingress leads to a continuous increase in tank pressure. Unless the pressure is controlled, the design pressure is reached, causing the safety valve to operate, which leads to even more production of GHG. For these reasons, treatment of the BOG is essential. Fig. 4 shows the changes with time of the BOG components in the receiving tank that require treatment.

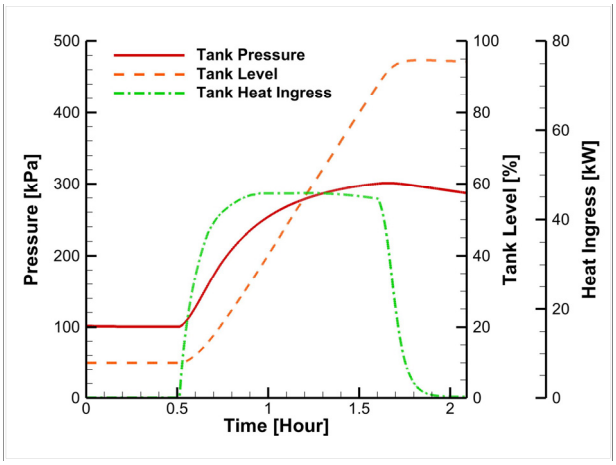

Fig. 2 Changes in tank pressure, level, and heat ingress according to time of bunkering of the receiving tank (500 m^3)

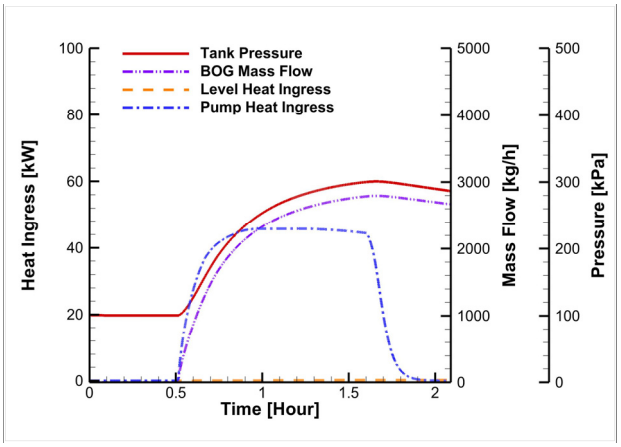

Fig. 3 Changes in tank pressure, level heat ingress, pump heat ingress, and BOG mass flow according to bunkering time of the receiving tank (500 m^3)

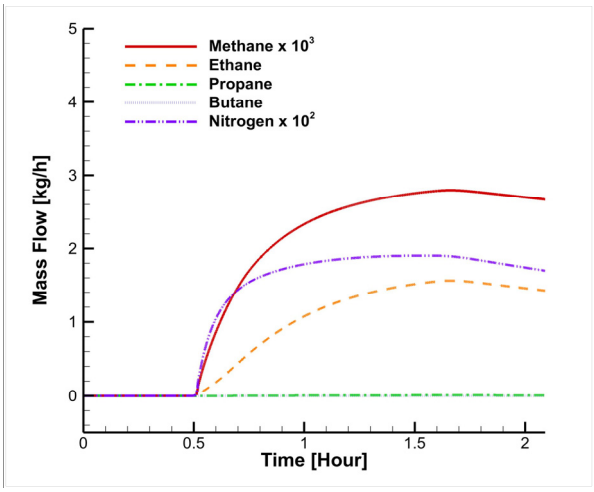

Fig. 4 Changes in BOG composition according to bunkering time of the receiving tank (500 m^3)

Table 4 presents the mass of the BOG components that should be treated to prevent a pressure rise in the receiving tank. The BOG composition in Table 4 differs from the LNG composition in Table 2. The main component is methane, so it may be safely conjectured that the BOG produced during bunkering is pure methane. The three major ways to treat BOG and the corresponding CO_2 conversion of each BOG treatment are shown in Table 5. The method of venting with its atmospheric release causes the highest GHG emission.

Table 4 Composition of BOG of the receiving tank (500 m^3)

	Methane	Ethane	Propane	Butane
Mass of BOG composition (kg)	3676.1	1.8	0.0095	0.00021

Table 5 CO_2 Emission from each BOG treatment method (500 m^3 tank)

	Venting	GCU	Re-liquefaction
CO_2 Equivalent (kg)	91,903	10,086	2,649

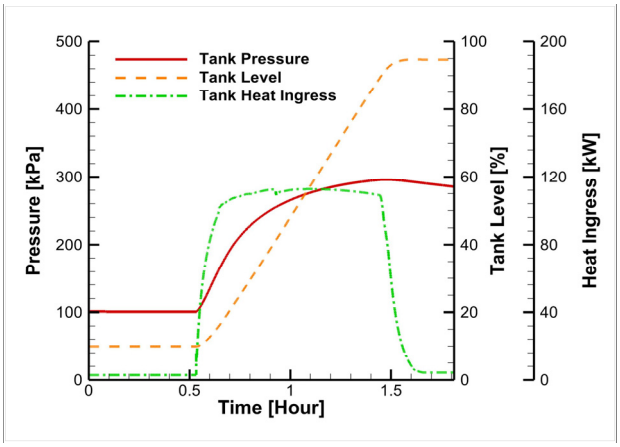

Fig. 5 Changes in pressure, water level, and heat ingress through time for a 1,000 m^3 receiving tank

Fig. 5 shows the changes in pressure, water level, and heat ingress in the 1,000 m^3 receiving tank through time. At the beginning of bunkering, the inflow of cryogenic LNG and the heat ingress due to the compressor device lead to an increase in overall heat ingress. The pressure and water level also show a trend of increase.

As shown in Fig. 6, the heat ingress values related to the water level and the compressor device and the BOG flow increase with time. The transported flow increases with operation of the pump, which in turn increases the pump heat ingress, and the consequent rise in water level increases the level-related heat ingress. It is also apparent that the amount of BOG to be treated increases with the resulting increase in tank pressure. Fig. 7 shows the amount of BOG to be treated according to time for the receiving tank. Methane, the most abundant component, requires the highest level of treatment, and the amount of methane to be treated increases as the volume increases.

The amount of methane to be treated for the receiving tank in LNG bunkering is approximately 6,000 kg, as shown in Table 6. The content of methane is the highest content among the BOG components, and it is even higher in comparison to the LNG composition. This allows the

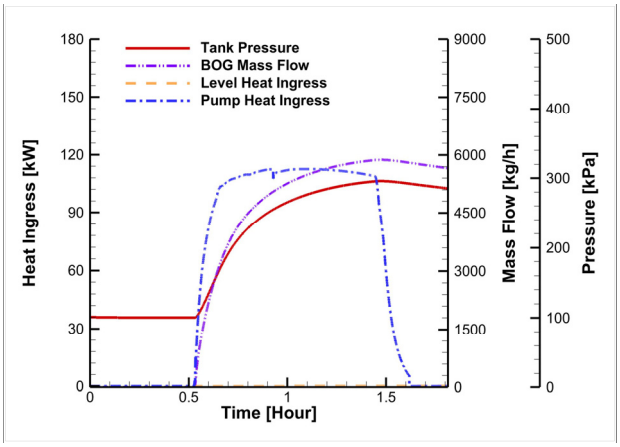

Fig. 6 Changes in tank pressure, level heat ingress, pump heat ingress, and BOG mass flow according to time with the 1,000 m^3 receiving tank

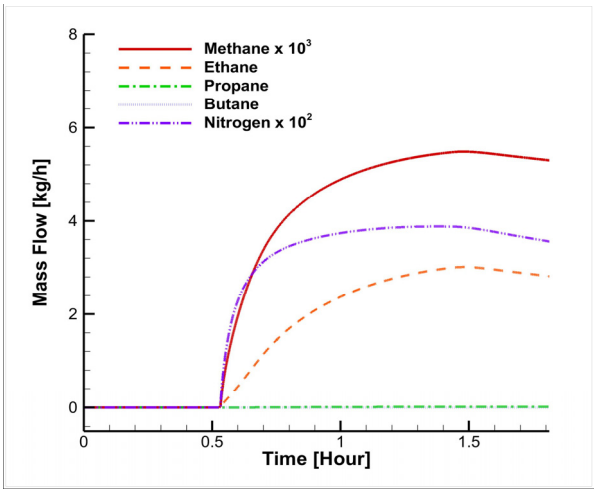

Fig. 7 Changes in BOG composition according to time with the 1,000 m^3 receiving tank

assumption that the BOG is composed entirely of methane. As methane is the main GHG, its treatment is indispensable. Table 7 presents the result of quantifying the CO_2 emission in accordance with each BOG treatment method. Compared to venting, GCU and re-liquefaction, which release CO_2 through combustion, are more advantageous, reducing the GHG at a rate of 50% or higher.

Table 6 BOG composition of the receiving tank (1,000 m^3)

	Methane	Ethane	Propane	Butane
Mass of BOG composition (kg)	5974.6	3.0	0.015	0.00033

Table 7 CO_2 emission from each BOG treatment method (1,000 m^3 tank)

	Venting	GCU	Re-liquefaction
CO_2 Equivalent (kg)	149,365	16,393	4,314

4.2 LNG Line Purging

Ships using LNG as fuel emit a large amount of GHG during the line purging process for disconnecting the bunkering line, as well as in bunkering. After a 98% filling of the receiving tanks, line purging is performed, and methane and CO_2 are released, as shown in Table 8.

Table 8 GHG emission during line purging

Procedure	Tank capacity	CH_4 mass (kg)	CO_2 Equivalent (kg)
Line purging	500	60.6	1514.3
	1,000	121.1	3028.7

4.3 Operating

The engine selected for the LNG-fueled ship was the Hyundai 5H22CFP, which is a dual-fuel engine. The GHG emission for the ship's fuel consumption based on the fuel type is as follows: 630 g CO_2e/kWh for MGO, 620 g CO_2e/kWh for heavy fuel oil (HFO), and 412 g CO_2e/kWh for LNG (El-Houjeiri, Hassan et al., 2019; Jang et al., 2021). The CO_2 emission varied according to the tank size and the BOG treatment method, as shown in Table 9. The fuel consumption is the amount of fuel required by the selected engine to the consumption at which a trace amount of LNG remains inside the tank (heel), i.e., 10% from the 98% filling of the receiving tank. The operation time per tank size can be estimated based on the engine use. When the tank size is larger, the sailing time is larger, which is a benefit from the operational perspective; however, the BOG increases due to the heat ingress related to the water level and the compressor device. This increases the amount of BOG to be treated and ultimately leads to CO_2 emission. Among the BOG treatment methods, venting results in the highest level of GHG emission, and the variation among methods becomes more apparent as the fuel tank size decreases. The use of LNG is known to reduce CO_2 emissions, but the results in this study showed a GHG emission increase of approximately 32% when using venting for BOG treatment in LNG-fueled ships in comparison to the use of the conventional fuels (MGO/HFO). Therefore, to maximize the advantages of LNG as an environmentally friendly fuel, GCU or re-liquefaction, with a reduction effect of approximately 25–30%, seems appropriate for BOG treatment.

5. Discussion

This study investigated the impact of LNG fuel tank size on the generation of GHG in terms of fuel consumption and gas emission in varying conditions and in accordance with BOG treatment methods. Furthermore, the problems associated with using LNG as an

Table 9 GHG emission generated during LNG-fueled ship operation

Tank Capacity	Fuel consumption $\times 10^3$ (kg/h)	Operating time (h)	BOG or CO_2 mass by procedure $\times 10^2$ (kg)			GHG emission of marine engine (g/kWh Engine)				
			Bunkering BOG	Line purging CO_2	Operating CO_2	Venting	GCU	Re-li	MGO	HFO
500	196	186	39.5	15.1	842	896.1	437.4	432.4	620	630
600	235	223	44.4	18.2	1,010	840.7	436.3	431.6		
700	274	260	49.4	21.2	1,178	820.8	435.5	431.0		
800	313	297	54.4	24.2	1,347	806.0	434.9	430.6		
900	352	334	59.3	27.3	1,515	794.4	434.4	430.2		
1,000	391	372	64.3	30.3	1,684	784.9	434.0	430.0		

environmentally friendly fuel were examined. In particular, the focus was the analysis of CO_2 emission according to changes in BOG production and BOG treatment method. LNG bunkering was described through dynamic simulation, and the entire set of CO_2 indicators, including CO_2 emission during bunkering as well during other procedures, including operation procedures, was defined. The results are summarized below.

(1) With the focus on the analysis of CO_2 emission according to changes in BOG production and BOG treatment method based on fuel tank size, LNG bunkering was described through dynamic simulation and representative CO_2 indicators were determined in consideration of the procedures leading to the generation of GHG during bunkering and during sailing.

(2) From the operational perspective, re-liquefaction is the treatment method that generates the lowest GHG emission if the priority is set as bunkering, whereas venting led to a more clearly distinguished GHG emission in comparison to re-liquefaction as the size of the ship decreased.

(3) From the environmental perspective, the feasibility of replacing HFO or MGO with LNG was verified. The BOG treatment of venting for LNG-fueled ships led to an increase in GHG emission of approximately 32% compared to MGO, implying that the potential of LNG as alternative environmental solution is not ensured.

(4) The BOG treatments of GCU and re-liquefaction led to approximately 25% and 30% reductions in GHG in comparison to HFO and MGO, thus satisfying the criteria for environmentally friendly fuels and supporting the potential of LNG as an alternative environmental solution.

(5) The impact of the BOG treatment method on the GHG emission was shown to be greater than the impact of tank size. From the perspective of EEDI, the lowest GHG emission may be ensured by a larger tank size and the selection of re-liquefaction as the BOG treatment method.

In this study, the fuel tank type was limited to the Type C tank commonly used in LNG-fueled ships. In addition, the GHG emission from the ship was estimated for the two tank sizes and for the gas engine. The estimates were then used to estimate the GHG emission throughout the operation cycle in accordance with the BOG generation and BOG treatment method. Thus, care should be taken in generalizing the results of this work to all ships or engine conditions. To obtain additional significant results, future studies should investigate main carbon-based components other than methane in the set conditions and use an extended scope.

6. Conclusions

This study investigated the GHG emission associated with fuel bunkering and operation procedures for different sizes of the Type C fuel tank. The level of GHG impact was analyzed separately for methane leakage during bunkering, the treatment of BOG generated during bunkering and operation, and with respect to engine use. From the perspective of the operation cycle, the GHG emission was comparatively analyzed against conventional ship fuels with consideration of the BOG treatment method and each tank size. Operators can use the findings in this study to assess environmental alternatives and select the optimum BOG treatment method to minimize GHG emissions from the respective ship.

Funding

This research was funded by the Korea Institute of Marine Science & Technology Promotion (grant number 20200478).

References

Ahn, J., Lee, S., Jeong, J., & Choi, Y. (2021). Comparative Feasibility Study of Combined Cycles for Marine Power System in a Large Container Ship Considering Energy Efficiency Design Index (EEDI). International Journal of Hydrogen Energy, 46(62), 31816−31827. https://doi.org/10.1016/j.ijhydene.2021.07.068

Al-Breiki, M., & Bicer, Y. (2020). Investigating the Effects of Boil-off Gas on Liquefied Energy Carriers During Land Storage and Ocean Transportation. In IOP Conference Series: Earth and Environmental Science, 581(1), 012017. IOP Publishing.

Arteconi, A., Brandoni, C., Evangelista, D., & Polonara, F. (2010). Life-cycle Greenhouse Gas Analysis of LNG as a Heavy Vehicle Fuel in Europe. Applied Energy, 87(6), 2005−2013. https://doi.org/10.1016/j.apenergy.2009.11.012

Cadafalch, J., Carbonell, D., Consul, R., & Ruiz, R. (2015). Modelling of Storage Tanks with Immersed Heat Exchangers. Solar Energy, 112, 154−162. https://doi.org/10.1016/j.solener.2014.11.032

Chang, Y.T., Song, Y., & Roh, Y. (2013). Assessing Greenhouse Gas Emissions from Port Vessel Operations at the Port of Incheon. Transportation Research Part D: Transport and Environment, 25, 1−4. https://doi.org/10.1016/j.trd.2013.06.008

Chorowski, M., Duda, P., Polinski, J., & Skrzypacz, J. (2015). LNG Systems for Natural Gas Propelled Ships. In IOP Conference Series: Materials Science and Engineering, Tucson, AZ, USA, 101(1), 012089.

Dissanayake, D., Rosynek, M.P., Kharas, K.C., & Lunsford, J.H. (1991). Partial Oxidation of Methane to Carbon Monoxide and Hydrogen over a Ni/Al2O3 Catalyst. Journal of Catalysis, 132(1), 117−127. https://doi.org/10.1016/0021-9517(91)90252-Y

Lee, H.J., Yoo, S.H., & Huh, S.Y. (2020). Economic Benefits of Introducing LNG-fuelled Ships for Imported Flour in South Korea. Transportation Research Part D: Transport and Environment, 78, 102220. https://doi.org/10.1016/j.trd.2019.102220

Wada, Y., Yamamura, T., Hamada, K., & Wanaka, S. (2021). Evaluation of GHG Emission Measures Based on Shipping and Shipbuilding Market Forecasting. Sustainability, 13(5), 2760. https://doi.org/10.3390/su13052760

Winnes, H., & Fridell, E. (2009). Particle Emissions from Ships: Dependence on Fuel Type. Journal of the Air & Waste Management Association, 59(12), 1391−1398. https://doi.org/10.3155/1047-3289.59.12.1391

Yu, Y.U., Park, S.H., Jung, D.H., & Lee, C.H. (2020). Improving Liquefied Natural Gas Bunkering in Korea through the Chinese and Japanese Experiences. Sustainability, 12(22), 9585. https://doi.org/10.3390/su12229585

Edfors, J., & Bremberg, R. (2021). Liquid Natural Gas: A Study of the Environmental Impact of LNG in Comparison to Diesel. Retrieved from http://urn.kb.se/resolve?urnurn:nbn:se:lnu:diva-103569

El-Houjeiri, H., Monfort, J.C., Bouchard, J., & Przesmitzki, S. (2019). Life Cycle Assessment of Greenhouse Gas Emissions from Marine Fuels: A Case Study of Saudi Srude Oil Versus Natural Gas in Different Global Regions. Journal of Industrial Ecology, 23(2), 374−388. https://doi.org/10.1111/jiec.12751

Herdzik, J. (2018). Methane Slip During Cargo Operations on LNG Carriers and LNG-fueled Vessels. New Trends in Production Engineering, 1(1), 293-299. https://doi.org/10.2478/ntpe-2018-0036

Im, S., Mostafa, A., Shin, S.R., & Kim, D.H. (2020). Combination of H_2SO_4-acidification and Temperature-decrease for Eco-friendly Storage of Pig Slurry. Journal of Hazardous Materials, 399, 123063. https://doi.org/10.1016/j.jhazmat.2020.123063

Jang, H., Jeong, B., Zhou, P., Ha, S., & Nam, D. (2021). Demystifying the Lifecycle Environmental Benefits and Harms of LNG as Marine fuel. Applied Energy, 292(15), 116869. https://doi.org/10.1016/j.apenergy.2021.116869

Jeong, B., Lee, B.S., Zhou, P., & Ha, S.M. (2017). Evaluation of Safety Exclusion Zone for LNG Bunkering Station on LNG-fuelled Ships. Journal of Marine Engineering & Technology, 16(3), 121−144. https://doi.org/10.1080/20464177.2017.1295786

Jung, D.H., Oh, S.H., Jung, J.H., Hwang, S.C., Sung, H.G., Lee, J.I., & Kim, E.S. (2018). Development of the First LNG Bunkering Barge System in Korea. In Proceedings of the Korean Institute of Navigation and Port Research Conference, 162−163. Korean Institute of Navigation and Port Research.

Kwak, D.H., Heo, J.H., Park, S.H., Seo, S.J., & Kim, J.K. (2018). Energy-efficient Design and Optimization of Boil-off Gas (BOG) re-liquefaction Process for Liquefied Natural Gas (LNG)-fuelled Ship. Energy, 148, 915−929. https://doi.org/10.1016/j.energy.2018.01.154

Lee, H., Choi, J., Jung, I., Lee, S., Yoon, S., Ryu, B., & Kang, H. (2020). Effect of Parameters on Vapor Generation in Ship-to-Ship Liquefied Natural Gas Bunkering. Applied Sciences, 10(19), 6861. https://doi.org/10.3390/app10196861

Lee, S. (2017). Multi-parameter Optimization of Cold Energy Recovery in Cascade Rankine Cycle for LNG Regasification Using Genetic Algorithm. Energy, 118, 776−782. https://doi.org/10.1016/j.energy.2016.10.118

Lowell, D., Wang, H., & Lutsey, N. (2013). Assessment of the Fuel Cycle Impact of Liquefied Natural Gas as Used in International Shipping. The International Council on Clean Transportation.

Naji, S.Z., Abd, A.A., & Hashim, A.S. (2019). Tracking Boil off Gas Generation into Liquefied Natural Gas Supply Chain Using HYSYS Simulator. In IOP Conference Series: Materials Science and Engineering, 579(1), 012019. IOP Publishing.

Noh, Y., Chang, K., Seo, Y., & Chang, D. (2014). Risk-based Determination of Design Pressure of LNG Fuel Storage Tanks Based on Dynamic Process Simulation Combined with Monte Carlo Method. Reliability Engineering & System Safety, 129, 76−82. https://doi.org/10.1016/j.ress.2014.04.018

Penteado, R., Cavalli, M., Magnano, E., & Chiampo, F. (2012). Application of the IPCC Model to a Brazilian Landfill: First Results. Energy Policy, 42, 551−556. https://doi.org/10.1016/j.enpol.2011.12.023

Ryste, J.M. (2012). Screening LCA of GHG Emissions Related to LNG as Ship Fuel (Master's thesis). Institutt for Marin Teknikk, Norwegian University of Science and Technology.

Ryu, J., Lee, C., Seo, Y., Kim, J., Seo, S., & Chang, D. (2016). A Novel Boil-off Gas Re-liquefaction Using a Spray Recondenser for Liquefied Natural-gas Bunkering Operations. Energies, 9(12), 1004. https://doi.org/10.3390/en9121004

Shao, Y., Lee, Y.H., Kim, Y.T., & Kang, H.K. (2018). Parametric Investigation of BOG Generation for Ship-to-ship LNG Bunkering. Journal of the Korean Society of Marine Environment & Safety, 24(3), 352−359. https://doi.org/10.7837/kosomes.2018.24.3.352

Shao, Y., Lee, Y., & Kang, H. (2019). Dynamic Optimization of Boil-off Gas Generation for Different Time Limits in Liquid Natural Gas Bunkering. Energies, 12(6), 1130. https://doi.org/10.3390/en12061130

Sharafian, A., Blomerus, P., & Merida, W. (2019). Liquefied Natural Gas Tanker Truck-to-tank Transfer for On-road Transportation. Applied Thermal Engineering, 162, 114313. https://doi.org/10.1016/j.applthermaleng.2019.114313

Styhre, L., Winnes, H., Black, J., Lee, J., & Le-Griffin, H. (2017). Greenhouse Gas Emissions from Ships in Ports−Case Studies in Four Continents. Transportation Research Part D: Transport and Environment, 54, 212−224. https://doi.org/10.1016/j.trd.2017.04.033

Unseki, T. (2013). Environmentally Superior LNG-Fueled Vessels. Mitsubishi Heavy Industries Technical Review, 50(2), 37−43.

Vairo, T., Gualeni, P., Fabiano, B., & Benvenuto, A.C. (2020). Resilience Assessment of Bunkering Operations for A LNG Fuelled Ship. Proceedings of the 30th European Safety and Reliability Conference and the 15th Probabilistic Safety Assessment and Management Conference. https://doi.org/10.3850/981-973-0000-00-0 output

Wood, D.A., & Kulitsa, M. (2018). A Review: Optimizing Performance of Floating Storage and Regasification Units

(FSRU) by Applying Advanced LNG Tank Pressure Management Strategies. International Journal of Energy Research, 42(4), 1391−1418. https://doi.org/10.1002/er.3883

Zincir, B., & Dere, C. (2015). Adaptation of LNG Fuel System Workout to a Simulator for Training Purpose of Engine Officers. In International Conference on Engine Room Simulators (ICERS12) Proceedings Book, 115−122.

Author ORCIDs

Author name	ORCID
Park, Eun Young	0000-0001-9810-6388
Choi, Jung Ho	0000-0003-1522-6080

KSOE

Journal of Ocean Engineering and Technology 35(6), 403-413, December, 2021
https://doi.org/10.26748/KSOE.2021.067

pISSN 1225-0767
eISSN 2287-6715

Original Research Article

Impact of the Thruster Jet Flow of Ultra-large Container Ships on the Stability of Quay Walls

Taegeon Hwang[1], Gyeong-Seon Yeom[2], Minjang Seo[1], Changmin Lee[1] and Woo-Dong Lee[3]

[1]*Graduate Student, Department of Ocean Civil Engineering, Gyeongsang National University, Tongyeong, Korea*
[2]*General Manager, Civil Zero Defect Team, Civil Business Division, DL E&C, Seoul, Korea*
[3]*Associate Professor, Department of Ocean Civil Engineering, Gyeongsang National University, Tongyeong, Korea*

KEY WORDS: Ultra-large container ship, Thruster, Jet flow, Hydrodynamic force, Coastal structure stability, Fluid–structure interaction

ABSTRACT: *As the size of ships increases, the size and output power of their thrusters also increase. When a large ship berths or unberths, the jet flow produced from its thruster has an adverse effect on the stability of quay walls. In this study, we conducted a numerical analysis to examine the impact of the thruster jet flow of a 30,000 TEU container ship, which is expected to be built in the near future, on the stability of a quay wall. In the numerical simulation, we used the fluid–structure interaction analysis technique of LS-DYNA, which is calculated by the overlapping capability using an arbitrary Lagrangian Eulerian formulation and Euler–Lagrange coupling algorithm with an explicit finite element method. As the ship approached the quay wall and the vertical position of the thruster approached the mound of the quay wall, the jet flow directly affected the foot-protection blocks and armor stones. The movement and separation of the foot-protection blocks and armor stones were confirmed in the area affected directly by the thruster jet flow of the container ship. Therefore, the thruster jet flows of ultra-large ships must be considered when planning and designing ports. In addition, the stability of existing port structures must be evaluated.*

1. Introduction

Increasingly large container ships are being constructed to accommodate increasing shipping volumes. Based on the definition of container capacity by Prokopowicz and Berg-Andreassen (2016), the construction of ultra-large container ships (ULCSs) of 20,000 twenty-foot equivalent units (TEU) or larger is being realized at a higher rate than that of very large container ships (VLCSs) of 10,000–20,000 TEU. Currently (as of August 2021), the largest container ships among the ULCS are of 24,000 TEU, with 36 in operation. The size of the ship is up to 399.9 m in length and 61.5 m in width. The Korea Maritime Institute (KMI) predicted that ULCSs of 30,000 TEU with a length of 493.2 m, width of 64.1 m, and load draft of 17.5 m would be designed in the near future (Jeon, 2015).

As the size of the ship increases, the size of its bow and stern thrusters, which are dynamic positioning systems (DPSs), also increases. The thruster of a ship is generally used as an auxiliary propulsion device to maintain a route in coastal waters with low water depth, waterways with narrow channels such as canals, and seas with strong currents or winds. If no mandatory regulations exist on the use of tugs, ship thrusters can considerably save time and money by enabling lateral movement during berthing and deberthing. The jet flow produced from the thruster, however, directly affects the quay wall while the ship is berthing and deberthing, which should be analyzed.

Studies on ship thrusters focus on their hydrodynamic properties and performance (Bulten and Suijkerbuijk, 2013; Yu and Yang, 2016; Abramowicz-Gerigk and Gerigk, 2020; Feng et al., 2020) and their operation, as well as berthing and deberthing simulation results (Bui et al., 2010; Tran and Im, 2012; Jeong et al., 2012; Benedict et al., 2017; Artyszuk and Zalewski, 2021). To understand the effects of thruster jet flow, flow characteristics around the quay wall (van Blaaderen, 2006; Irene, 2020), pressure (Abramowicz-Gerigk et al., 2018), and bottom scour (van den Brink, 2014; Roelse, 2014; Galal et al., 2016; Galal et al., 2019) have been analyzed. However, the behavior of the quay wall corresponding to the direct action of the thruster jet flow has hardly been discussed. As the size of the ship increases, the size of its thrust and draft considerably increase, thereby exhibiting a more considerable impact on the surrounding waters. Therefore, to build a safe port, the thruster jet flow of large container ships in existing port facilities should be analyzed before designing a new port.

Received 25 August 2021, revised 26 October 2021, accepted 31 October 2021
Corresponding author Woodong Lee: +82-55-772-9126, wdlee@gnu.ac.kr

This study aims to analyze the effect of thruster jet flow on a quay wall for a ULCS of 30,000 TEU, which is expected to be built in the near future. LS-DYNA, which allows for the analysis of fluid–structure interaction (FSI) and the simulation of complex nonlinear problems such as collisions and material shaping, is used to realize numerical simulations. The hydraulic characteristics of the jet flow of the ship thruster as well as the stability of the quay wall caissons, foot-protection blocks, and armor stones are discussed by applying the arbitrary Lagrangian Eulerian (ALE) method, which is selected among the several other FSI analysis methods of LS-DYNA.

2. Numerical Method

In this study, the ALE method of LS-DYNA R12 (LSTC, 2020), which can simultaneously consider the behaviors of the fluid and structure, was applied to simulate the nonlinear mutual interference of the thruster jet flow and the quay wall. LS-DYNA not only specializes in nonlinear analyses such as collision and destruction based on the explicit method, but also facilitates collision analyses between multiple objects as it does not require the contact elements to be created separately.

2.1 LS-DYNA

The ALE method (Santini et al., 1998; Souli et al., 2000; Sedden et al., 2004; Poehlmann-Martins et al., 2005) facilitates a bidirectional nonlinear interaction analysis between fluids and structures without deformation or movement of the computational grid. This method requires a reference coordinate system in addition to the Lagrangian and Eulerian coordinate systems, and it can handle boundary conditions, large deformations, and contact surface problems according to arbitrary motion. The following equation represents the relationship between the material time derivative and the reference configuration time derivative:

$$\frac{\partial f(X_i,t)}{\partial t}=\frac{\partial f(x_i,t)}{\partial t}-(v_i-u_i)\frac{\partial f(x_i,t)}{\partial x_i}=\frac{\partial f(x_i,t)}{\partial t}-w_i\frac{\partial f(x_i,t)}{\partial x_i} \quad (1)$$

where X_i denotes the Lagrangian coordinate system; x_i denotes the Eulerian coordinate system; i denotes the reference coordinate system; and v_i and u_i denote the velocities of the material and space.

In LS-DYNA, the ALE technique method tracks the transfer of energy, mass, and momentum between elements by applying the continuity equation in the finite element method (FEM). The equations for the conservation of mass, momentum, and energy in the ALE methods are given below:

$$\frac{\partial \rho}{\partial t}=(-\rho)\div(v)-(v_i-u_i)\frac{\partial \rho}{\partial x_i} \quad (2)$$

$$\rho\frac{\partial v_i}{\partial t}\equiv\sigma_{i,j}-\rho(v_i-u_i)\frac{\partial v_i}{\partial x_j} \quad (3)$$

$$\rho\frac{\partial e}{\partial t}=\sigma_{ij}\epsilon_{ij}-\rho(v_i-u_i)\frac{\partial e}{\partial x_j} \quad (4)$$

where ρ denotes the density of the material; v_i denotes the velocity of the material; σ_{ij} denotes the stress tensor; ϵ denotes the strain tensor; ϵ denotes the internal energy; u_i denotes the velocity of the mesh; and t denotes the time.

The ALE method was employed to supplement the shortcomings of the Lagrangian and Eulerian methods and to employ only the advantages. The fluid–structure coupling algorithm (FSCA) was applied to the contact surfaces of Lagrangian and Eulerian elements through operator splitting. If a significant element deformation occurred in the Lagrangian stage, the element was corrected by resetting the node position through the smoothing algorithm. In the Eulerian stage, the material properties of the element were transformed after the nodes were reset. During this process, the displacement and velocity of the Lagrangian structure model were substituted into the boundary conditions of the Eulerian fluid model, and the reaction force estimated by the FSCA acted on the elements of the Lagrangian structure model.

2.2 Numerical Condition

2.2.1 Numerical water tank

The container ship and quay wall were placed in a numerical water tank with a length of 85 m, width of 30 m, and height of 50 m, configured as shown in Fig. 1. Radiation boundary conditions were applied to the outer sea and both sides of the water tank, and no flux boundary conditions were applied to the floor and ceiling. For the ship and caisson, the fixed constraint conditions were considered, and for the armor stones on the slope of the mound and the foot-protection blocks on the floor, the free movement conditions were considered. The calculation grid and the calculation time interval of the numerical tank were set considering the Courant–Friedrichs–Lewy (CFL) and diffusive limit (DL) conditions, with the horizontal grid at 1 m and the vertical grid at 0.5 m; further, the initial calculation time interval ($\triangle t$) was 1/100 s. During calculation, $\triangle t$ was automatically varied to satisfy the CFL and DL conditions according to the fluid flow situation.

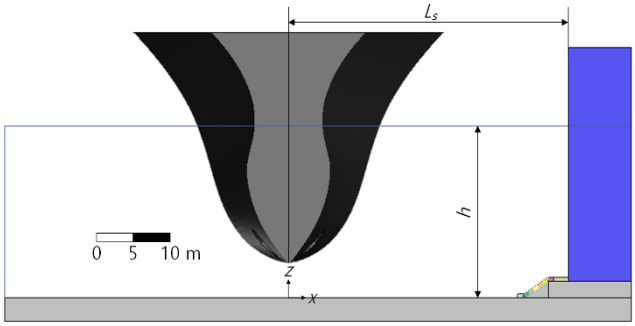

Fig. 1 Numerical water tank including container ship and quay wall used in this study

Table 1 Numerical conditions considered in this study

h (m)	L_s (m)
18 (Δh = -2)	33
20 (Δh = 0)	38
22 (Δh = +2)	43

The berthing distance (L_s) of the ship is based on the horizontal distance of 33 m between the wall of the caisson and the center of the thruster during berthing. The water depth (h) in the port is set considering a load draft of 17.5 m for the ULCS of 30,000 TEU. Table 1 summarizes the nine limited calculation conditions, where the distances to the ship were set as L_s = 33 m, L_s = 38 m, and L_s = 43 m, and the water depth conditions in the port as h = 18 m (low tide level), h = 20 m (mean tide level), and h = 22 m (high tide level).

2.2.2 Ship and thruster

The hull applied to the numerical analysis of this study is shown in Fig. 2. The hull model of the Korea Research Institute of Ships & Ocean Engineering Container Ship (KCS) with a size of 7.2786 m × 1.019 m × 0.6013 m was used. With reference to the KMI data (Jeon, 2015), the basic KCS was enlarged according to the specifications (493.2 m × 64.1 m × 17.5 m) of a ULCS of 30,000 TEU.

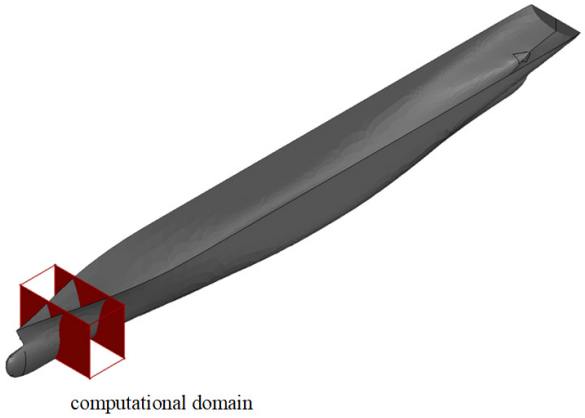

Fig. 2 Hull model of KCS

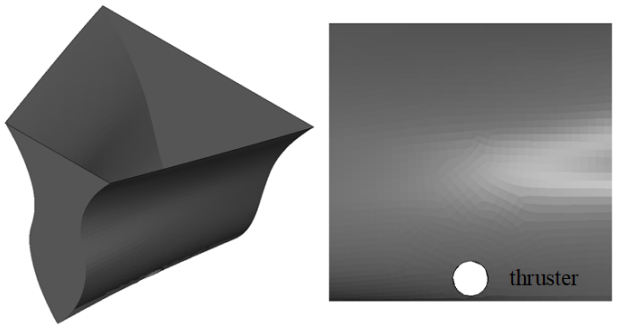

(a) 3D view (b) y-z sectional view

Fig. 3 Computational domain with a bow thruster

The domain shown in Fig. 2 is the section including the bow thruster, which was cut by 30 m and fixed to fit the width of the numerical water tank in Fig. 1. The computational domain, including this bow thruster, is shown in Fig. 3(a). No flux boundary conditions were applied to the hull. In this study, a single thruster with a diameter of 3.75 m was considered, as shown in Fig. 3(b), and the position of the center was 57 m from the bow and 2.58 m from the bottom of the ship, where the diameter and position of the thruster were set by referring to PIANC (2015).

2.2.3 Quay wall

Since this study aimed to examine the stability of the quay wall against the thruster jet flow, a simple quay wall that can minimize the flow change according to the caisson and the shape of the armor stones and foot-protection blocks was considered. The quay wall was in the form of a 30 m high non-perforated caisson mounted on a mound with a height of 2.1 m and a slope of 1:1.5. One row of 2 m × 3 m × 0.5 m concrete heavy-duty blocks was placed on the mound floor at the bottom of the caisson, and seven rows of armor stones, each row with a side length of 3.11 m, were arranged in a regular octagonal shape on the slope of the mound (Fig. 4). The thickness of a foot-protection block and an armor stone was the same at 0.5 m. To reduce the computational load, the thickness of the caisson was limited to 8.5 m, and fixed boundary conditions were considered for the ground, mound, and caisson. Fixed constraint conditions were applied to the foot-protection blocks and armor stones at the water tank boundary and at the toe of the mound indicated in red in Fig. 4. For convenience, the foot-protection blocks installed in one row were numbered from P1 to P9, and the armor stones installed in the six rows (A to F) were numbered from A1 to A39, B1 to B39, C1 to C39, D1 to 39, E1 to 39, and F1 to F39, excluding those under the fixed constraint conditions.

Table 2 summarizes the physical properties of the caisson, foot-protection block, and armor stone. The physical properties provided by Ansys were applied. As for the foot-protection block, which was considered to comprise concrete, a unit weight of 2,300 kg/m^3, Young's modulus of 30,000 MPa, and Poisson's ratio of 0.18 were applied. As for the armor stone, a unit weight of 2,600 kg/m^3, Young's modulus of 30,010 MPa, and Poisson's ratio of 0.234 were applied, based on the Rock Physics Handbook (Mavko et al., 2009). The weight of each foot-protection block was 6,900 kg, and the weight of each armor stone was 731 kg.

Table 2 Material properties used for numerical analysis

Item	B (m) × L (m) × H (m)	Specific weight (kg/m^3)	Young's modulus (MPa)	Poisson ratio
Caisson Foot-protection block	2 × 3 × 0.5	2,300	30,000	0.18
Armor stone	0.75 × 0.75 × 0.5	2,600	30,010	0.234

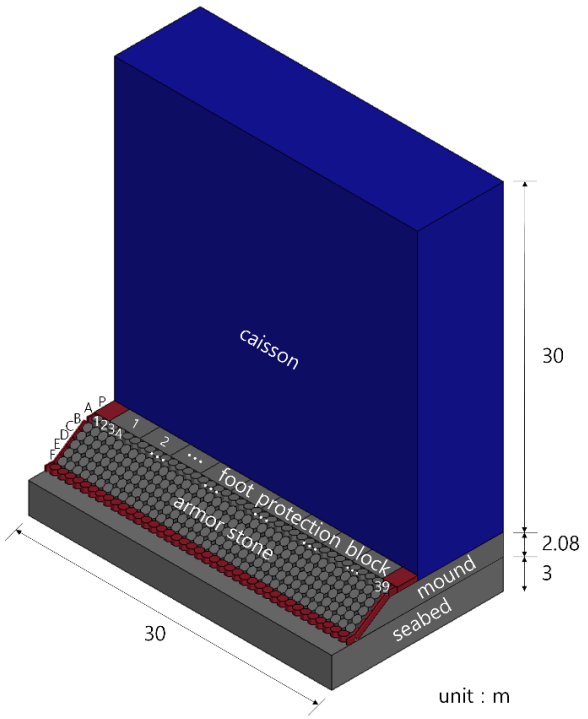

Fig. 4 Schematic of a quay wall with caissons, foot-protection blocks, and armor stones

2.2.4 Thruster flow

The maximum flow velocity of the jet flow generated by the thruster is calculated using Eq. (5), which was proposed by Fuehrer and Romisch (1977):

$$u_0 = 1.59nD\sqrt{K} \tag{5}$$

where n denotes the rotational speed (1/s) of the propeller, D denotes the thruster diameter (m), and K denotes the dimensionless thruster coefficient (0.2–0.5).

Regarding the specifications and performance of the single thruster of the 30,000 TEU ULCS, D is set as 3.75 m, n as 188 RPM, and K as the median value of 3.5, with reference to PIANC (2015) and Rolls-Royce (2013).

2.3 Validation

To validate the numerical model created using LS-DYNA, the propeller wake velocity equation in the Rock Manual (CIRIA et al., 2007) was used, based on the concept illustrated in Fig. 5.

$$u_{p,0} = 1.15\left(\frac{P}{\rho_w D_0^2}\right)^{\frac{1}{3}} \tag{6}$$

$$u_{p,axis}(x) = au_{p,0}\left(\frac{D_0}{x}\right)^m \tag{7}$$

$$u_p(x,r) = u_{p\bullet axis}(x) \bullet \exp\left(\frac{-br^2}{x^2}\right) \tag{8}$$

Here, P denotes the propulsion force of the marine engine (W), D_0 denotes the effective diameter of the propeller (0.7 times the diameter of the propeller with no nozzle), ρ_w denotes the unit weight of the fluid (kN/m^3), and r denotes the vertical distance from the center of the propeller (m). a, b, and m are empirical constants with values of 2.8, 5.2, and 1, respectively.

Fig. 6(a) shows the steady-state thruster flow field obtained using LS-DYNA. The vertical profiles for the a-a' cross-section are compared in Fig. 6(b) for verification (the a-a' section is 15 m away from the center of the thruster).

In Fig. 6(a), the jet flow generated by the thruster shows an upward flow pattern under the influence of floor friction. This accurately represents the typical characteristics of a jet flow, i.e., the distribution range of the propagated flow widens with a decrease in the flow velocity due to fluid viscosity. As seen in Fig. 6(b), the theoretical flow rate reaches its maximum at the thruster center (z = 7 m); however, the maximum flow velocity occurs slightly upward from the center, based on the LS-DYNA simulation results. This can be understood as a phenomenon that occurs as the flow spreads to the upper layer, since the upper part of the outlet opens first in the thruster structure. As a result, the theoretical flow rate generated by the open propeller is symmetric with respect to z = 7 m; however, the flow rate obtained based on the LS-DYNA simulation has an asymmetric structure with the developed upward flow velocity.

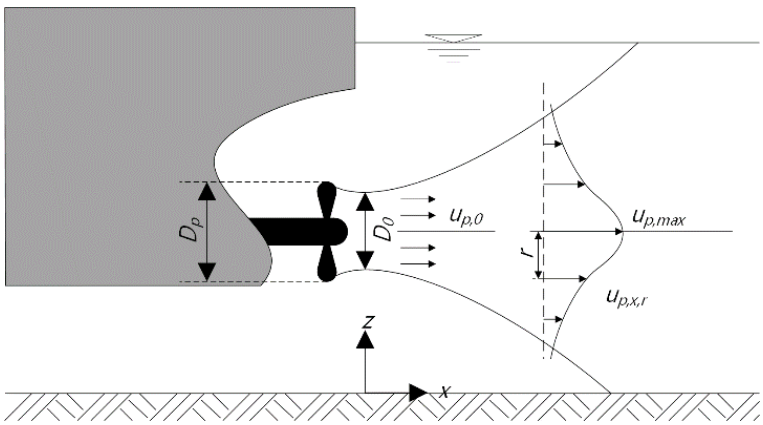

Fig. 5 Conceptual diagram of propeller wake (Reproduced from CIRIA et al., 2007)

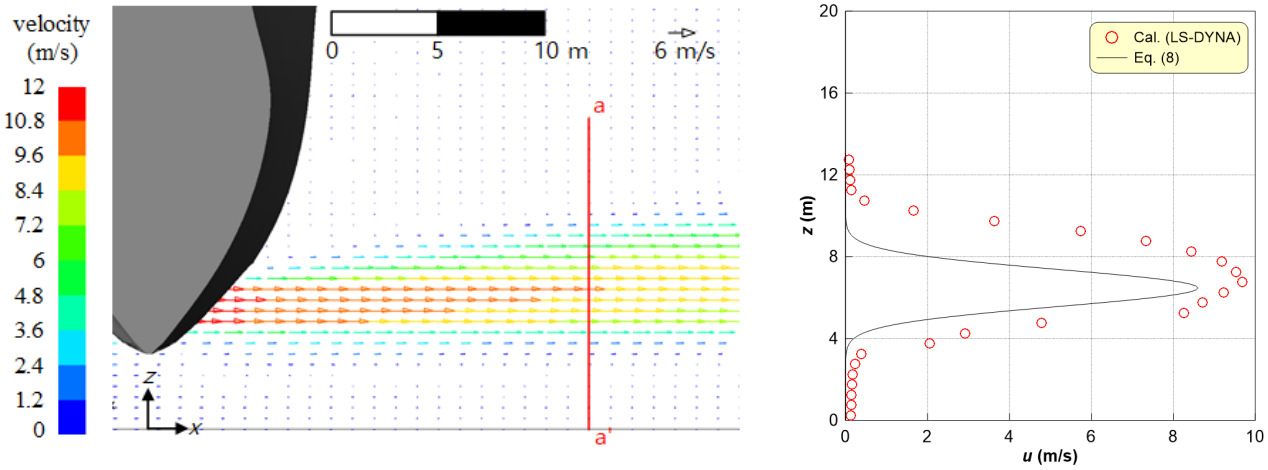

(a) Cross-sectional distribution (b) Vertical profile

Fig. 6 Comparison between numerical simulation and theoretical velocity

Although the maximum flow velocity and flow velocity distribution predicted using LS-DYNA are slightly overestimated compared with the theoretical values, the overall characteristics of the thruster jet flow generated by the ship appear to be accurately reproduced. In addition, Yeom et al. (2009) and Yeom et al. (2017) validated simulation results on the behavioral collision of structures obtained using LS-DYNA. Accordingly, the validity and effectiveness of LS-DYNA were partially confirmed in this study.

3. Numerical Results

3.1 Flow Field

Figs. 7 and 8 show the steady-state flow velocity distribution around the quay wall, which is attributed to the thruster jet flow of the 30,000 TEU ULCS. Fig. 7 shows the flow fields according to the water depth for L_s = 33 m. Fig. 8 shows the flow fields according to the distance to

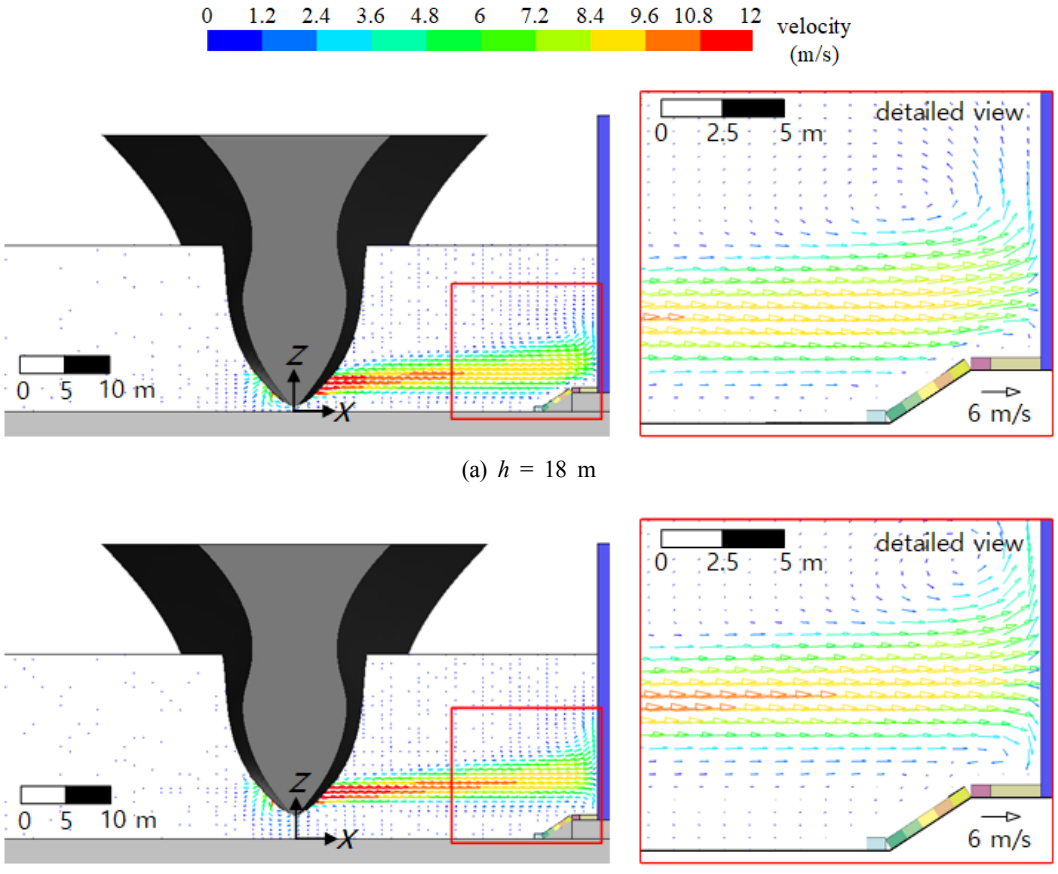

(a) h = 18 m

(b) h = 20 m

Fig. 7 Flow fields corresponding to different water depths (h) in midsection (Continued)

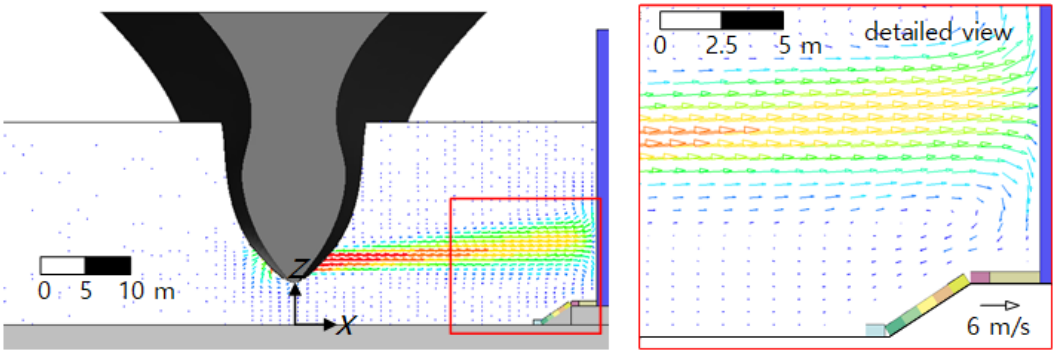

(c) h = 22 m

Fig. 7 Flow fields corresponding to different water depths (h) in midsection

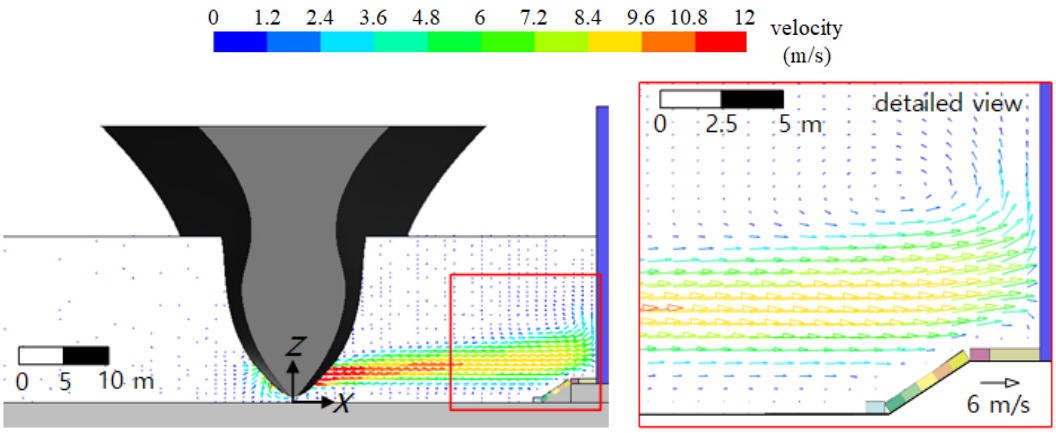

(a) L_s = 33 m

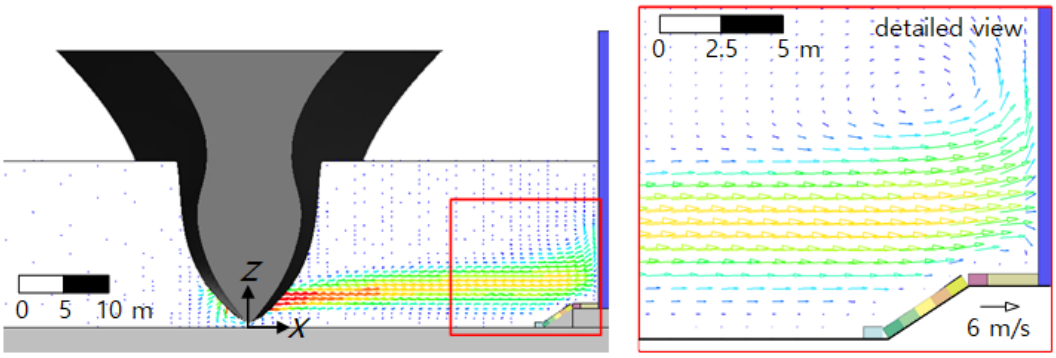

(b) L_s = 38 m

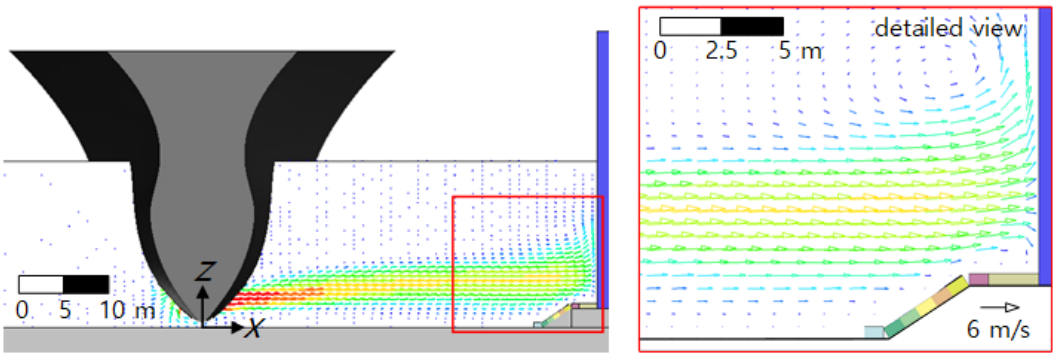

(c) L_s = 43 m

Fig. 8 Flow fields corresponding to different separation distances (L_S) in midsection

the ship under the low-tide condition (h = 18 m).

In Fig. 7(a), at h = 18 m, the direction of the flow toward the water surface is shown on the slope as the thruster jet flow moves directly to the quay wall caisson and mound. In other words, the caisson of the quay wall and the armor stones of the mound slope are directly affected by the thruster jet flow, and the foot-protection blocks placed on the mound floor are affected indirectly. Under the mean- and high-tide conditions, shown in Figs. 7(b)–7(c), the quay wall caisson is directly affected by the thruster jet flow (h = 20 m and h = 22 m), whereas the mound (foot-protection blocks and armor stones) is not significantly affected. In addition, for h = 22 m, a secondary flow that collides with the quay wall caisson and descends may develop.

Based on the thruster jet flow characteristics (Fig. 8) according to the separation distance of the ship, a wider distribution with a decrease in the flow velocity is observed as the propagation distance increases, as suggested in the theoretical flow characteristics of CIRIA et al. (2007). Thus, the larger L_s is, the lower is the impact of the thruster jet flow on the quay wall caisson, foot-protection blocks, and armor stones.

3.2 Stability

3.2.1 Response of structure

Figs. 9 and 10 show the behavior of the foot-protection blocks and the armor stones covering the mound, which constitute the substructure of the quay wall, according to the action of the thruster jet flow of the 30,000 TEU ULCS. Fig. 9 shows the behavioral characteristics according to h for L_s = 33 m. Fig. 10 shows the behavioral characteristics according to L_s for h = 18 m.

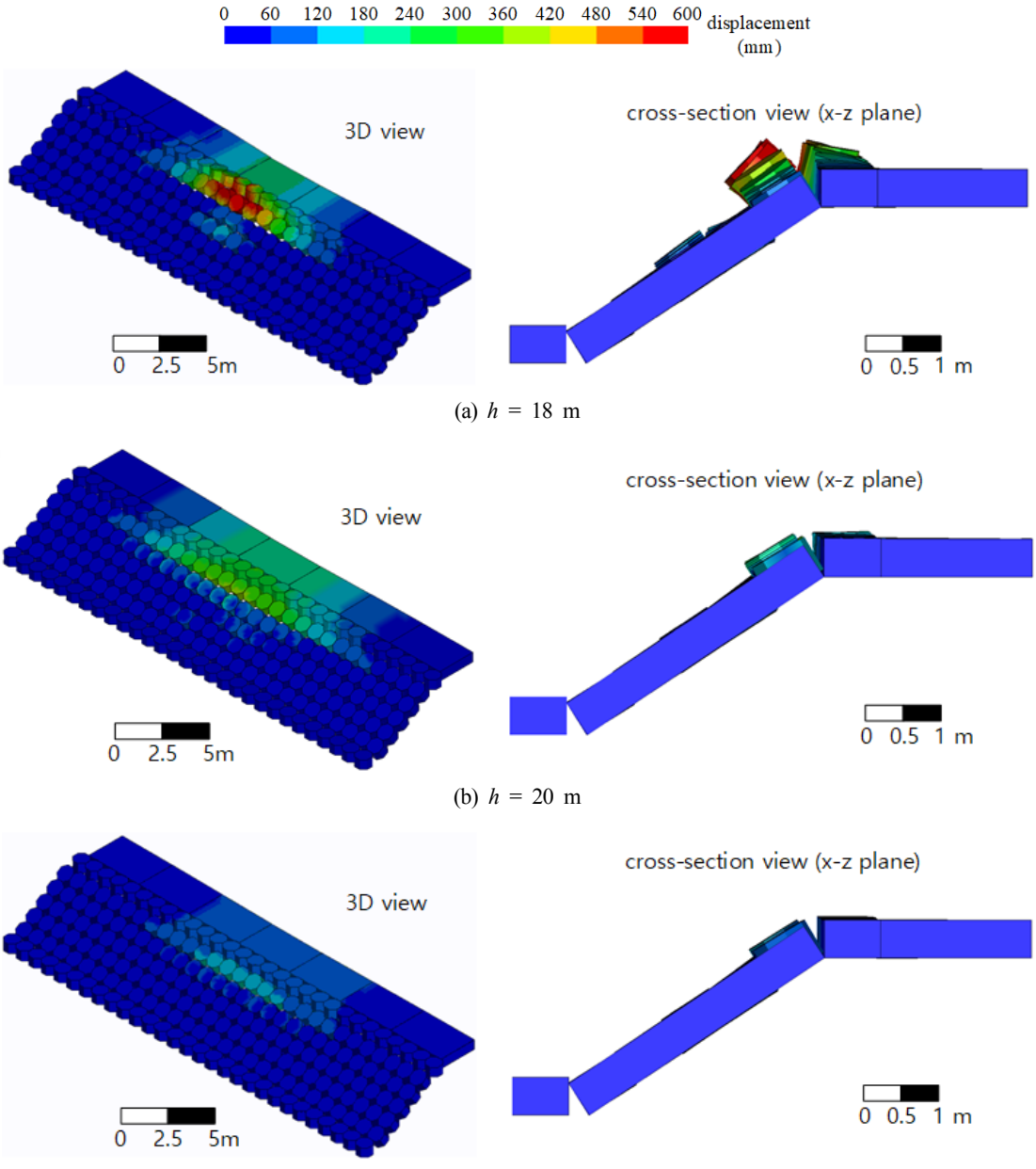

Fig. 9 Arrangement changes of foot-protection blocks and armor stones due with h

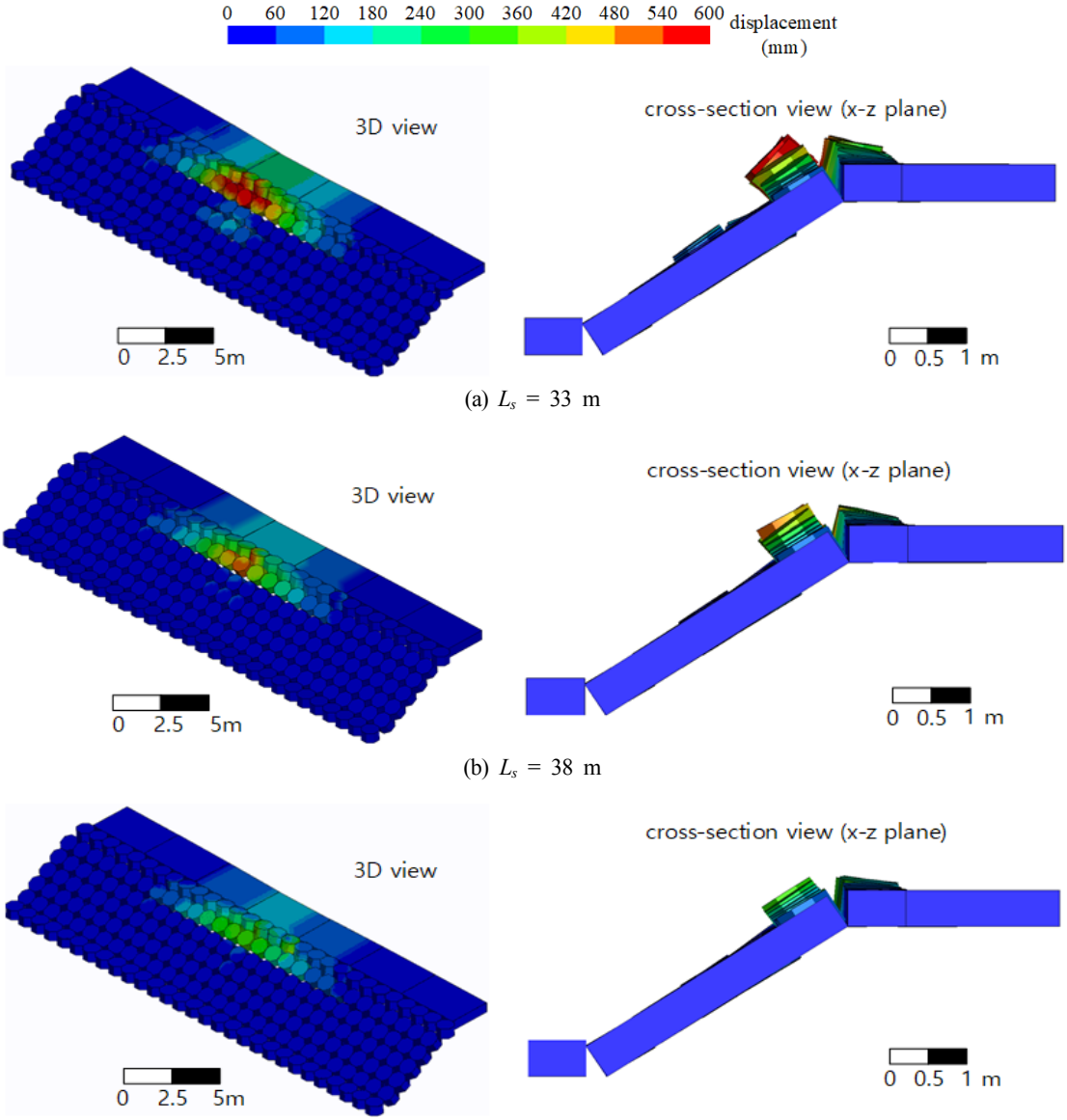

Fig. 10 Arrangement changes of foot-protection blocks and armor stones with L_s

At h = 18 m, as mentioned earlier, as the strong fluid force from the thruster jet flow of the ship acts on the mound shoulder, movement and departure of the armor stones are observed, which even induces movement of the adjacent foot-protection blocks. As the tide rises, the influence of the thruster jet flow is reduced; this reduces the movement of not only the armor stones but also the adjacent foot-protection blocks.

With regard to the behavioral characteristics of the foot-protection blocks and armor stones according to L_s, the larger L_s is, the wider the distribution of the flow acting on the quay wall becomes with decreasing flow velocity; thereby, the movement of the foot-protection blocks and armor stones is reduced, as evident from Fig. 8.

3.2.2 Maximum moving distance

Fig. 11 depicts the change in the moving distances of foot-protection block P5 and armor stone B20, which moved the most among all the foot-protection blocks and armor stones covering the mound, under the action of the thruster jet flow generated by the 30,000 TEU ULCS. Figs. 11(a) and 11(b) present the moving distances of the armor stone and foot-protection block, respectively.

As seen in Fig. 11, as the thruster jet flow is induced by the ship, the armor stone and foot-protection block begin to move, and they move considerably for up to 30 s. However, the movement of the relatively heavy foot-protection block decreases significantly thereafter. The movement of the lighter armor stone slows slightly after 30 s and then decreases significantly after 40 s. Overall, the foot-protection block and armor stone do not move significantly after 50 s. Therefore, in this study, the maximum moving distance (d_{max}) is defined as the moving distance of the foot-protection block and armor stone at 70 s after the generation of the thruster jet flow by the 30,000 TEU ULCS.

Fig. 12 and Table 3 show the d_{max} of P5 and B20, calculated as described above.

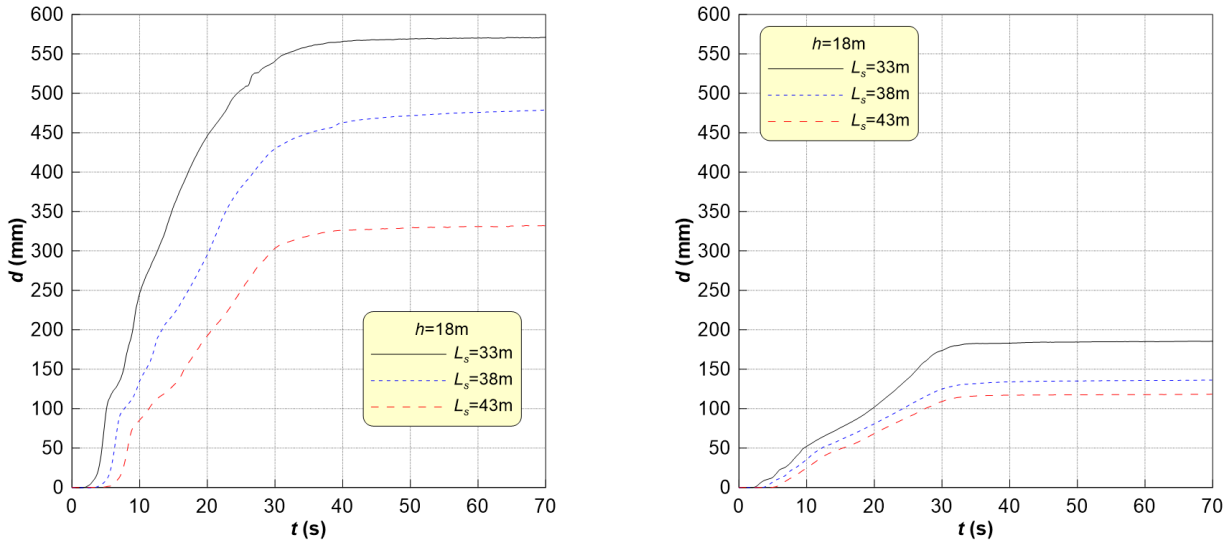

(a) Armor stone (b) Foot-protection block

Fig. 11 Changes in moving distance under thruster jet flow

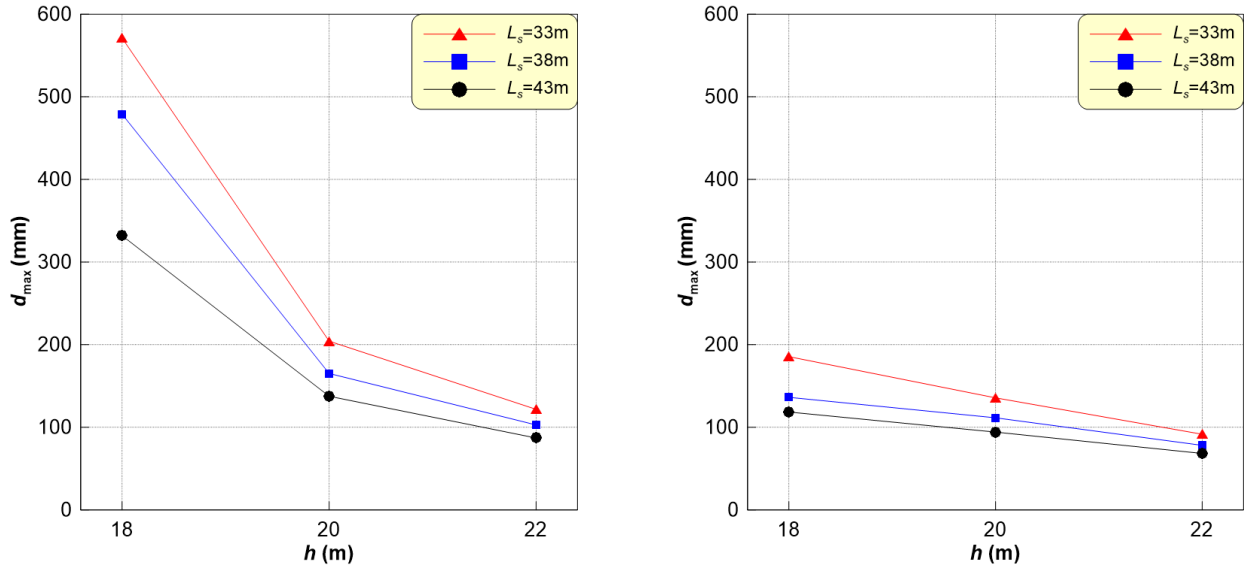

(a) Armor stone (b) Foot-protection block

Fig. 12 Maximum moving distance of an armor stone and a foot-protection block

Table 3 Maximum moving distance of a foot-protection block and an armor stone under thruster jet flow

h (m)	L_s (m)	Foot-protection block			Armor stone		
		F_{max} (kN)	D_{max} (mm)	note	F_{max} (kN)	D_{max} (mm)	note
18	33	96.54	185.44	P5	9.19	571.03	B20
	38	95.25	136.24		7.36	478.86	
	43	92.28	118.39		5.97	331.89	
20	33	116.19	135.59		2.93	204.22	
	38	114.99	111.44		2.74	165.09	
	43	99.99	94.12		2.6	137.5	
22	33	62.27	91.51		1.65	121.67	
	38	58.12	78.09		1.58	102.8	
	43	54.54	68.24		1.31	87	

While Fig. 12 and Table 3 show the numerical analysis results under limited-port conditions, the moving distances of P5 and B20 under the thruster jet flow are the greatest under the low-tide (h = 18 m) and vessel-berthing conditions (L_s = 33 m); in fact, d_{max} was 571.03 mm, which may cause B20 to fall off. The maximum moving distances of the foot-protection block and armor stone show a clear tendency to increase as the tide becomes lower and the separation distance becomes decreases; this is confirmed by the thruster jet flow characteristics and quay wall behavior discussed earlier.

4. Conclusions

In this study, numerical analysis was performed to examine the effect of the thruster jet flow generated by a 30,000 TEU ULCS on the stability of a quay wall. For numerical analysis, LS-DYNA was used, which enables FSI analysis and simulation of complex nonlinear problems such as collisions between multiple objects and material molding. The main numerical analysis results considering the limited computation conditions are as follows:

(1) For h = 18 m and L_s= 33 m, the thruster jet flow generated by a ULCS of 30,000 TEU directly affects the caisson of the quay wall and the armor slopes of the mound slope, and indirectly affects the foot-protection blocks on the mound floor. For h = 18 m and h = 22 m, the entire mound is not directly affected by the thruster jet flow. As the propagation distance increases, the distribution of the thruster jet flow increases, and the flow velocity decreases. Consequently, the effect of the thruster jet flow on the quay wall caisson, foot-protection blocks, and armor stones is reduced as L_s increases.

(2) At h = 18 m, the thruster jet flow generated by the ship directly affects the shoulder of the mound, causing movement and separation of the armor stones and even inducing movement of the adjacent foot-protection blocks. As h increases, the influence of the thruster jet flow is reduced, which considerably reduces the movement of the armor stones and adjacent foot-protection blocks. As L_s increases, the distribution of the flow acting on the quay wall is widened, and the flow velocity decreases; this reduces the movement of the armor stones and adjacent foot-protection blocks.

(3) Foot-protection block P5 and armor stone B20 moved the most under the ship thruster flow. Under L_s = 33 m and h = 18 m, d_{max} was 571.03 mm for B20; such a large d_{max} may even cause separation of the armor stone. For P5, the movement was not as significant, with d_{max} = 185.44 mm.

Based on these results, when the tide is lower and the ship is closer to the quay wall, the berthing or deberthing of the ship using a thruster has more adverse effects the foot-protection blocks and armor stones of the mound, which constitute the substructure of the quay wall. Therefore, when designing a new port, the stability of the port structures, such as those analyzed in this study, should be sufficiently considered. Furthermore, even at existing ports, it is necessary to dredge the waterways and expand and reinforce the berthing piers in line with the increasing sizes of ships, considering the stability of port facilities for accommodating ULCSs. This should be supported by a hydraulic model experiment considering actual port conditions or a numerical analysis, such as that conducted in this study.

Funding

This work was supported by the National Research Foundation of Korea (NRF) grant funded by the Korea government (MSIT) (No. NRF-2021R1A2C4002665).

References

Abramowicz-Gerigk, T., & Gerigk, M.K. (2020). Experimental Study on the Selected Aspects of Bow Thruster Generated Flow Field at Ship Zero-Speed Conditions. Ocean Engineering, 209, 107463. https://doi.org/10.1016/j.oceaneng.2020.107463

Abramowicz-Gerigk, T., Burciu, Z., Gorski, W., & Reichel, M. (2018). Full Scale Measurements of Pressure Field Induced on the Quay Wall by Bow Thrusters − Indirect Method for Seabed Velocities Monitoring. Ocean Engineering, 162, 150−160. https://doi.org/10.1016/j.oceaneng.2018.05.036

Artyszuk, J., & Zalewski, P. (2021). Energy Savings by Optimization of Thrusters Allocation during Complex Ship Manoeuvres. Energies, 14(16), 4959. https://doi.org/10.3390/en14164959

Benedict, K., Fischer, S., Gluch, M., Gluch, M., Schaub, M., Baldauf, M., & Müller, B. (2017). Innovative Fast Time Simulation Tools for Briefing / Debriefing in Advanced Ship Handling Simulator Training and Ship Operation. Transactions on Maritime Science, 6(1), 24−38. https://doi.org/10.7225/toms.v06.n01.003

Bui, V.P., Jeong, J.H., Kim, Y.B., & Kim, D.W. (2010). Optimal Control Design for Automatic Ship Berthing by Using Bow and Stern Thrusters. Journal of Ocean Engineering and Technology, 24(2), 10−17.

Bulten, N.W.H., & Suijkerbuijk, R. (2013). Full Scale Thruster Performance and Load Determination Based on Numerical Simulations. Proceedings of 3rd International Symposium on Marine Propulsors, Tasmania, Australia, 501−509.

CIRIA, CUR, CETMEF. (2007). The Rock Manual: The Use of Rock in Hydraulic Engineering (2nd Ed.). C683, London: CIRIA

Feng, Y., Chen, Z., Dai, Y., Zhang, Z., & Wang, P. (2020). An Experimental and Numerical Investigation on Hydrodynamic Characteristics of the Bow Thruster. Ocean Engineering, 209, 107348. https://doi.org/10.1016/j.oceaneng.2020.107348

Fuehrer, M., & Romisch, K. (1977). Effects of Modern Ship Traffic on Islands and Ocean Waterways and Their Structures. Proceedings of 24th Congress, P.I.A.N.C., Sections 1−3, Leningrad, Russia.

Galal, E.M., Halabia, N.S., & Tolba, E.R. (2016). The Effect of Sea Side Quay Wall Roughness and Inclination on Bed Scour Induced by Ship Bow-Thrusters. Malaysian Journal of Civil Engineering, 28(2), 205−217. https://doi.org/10.11113/mjce.v28.

15971

Galal, E.M., Halabia, N.S., & Tolba, E.R. (2019). Minimizing Bed Scour Induced by Ship Bow Thrusters by Using Quay Wall Flow Deflector. Malaysian Journal of Civil Engineering, 31(2), 17-26. https://doi.org/10.11113/mjce.v31.16115

Irene, C. (2020). Bowthruster-Induced Flow on the Bottom of a Vertical Quay Wall: A Field Measurement (Master's Thesis). Delft University of Technology, Netherlands.

Jeon, H. (2015). The Era of Mega Vessels and Challenges to Ports. PECC International Project Seminar.

Jeong, T.G., Chen, C., Lee, S.G., Lee, J.J., & Huh, Y.B. (2012). A Study on Development of Laptop-Based Pilots' Ship-Handling Simulation Software. Journal of Navigation and Port Research, 36(7), 571−575. https://doi.org/10.5394/KINPR.2012.36.7.571

Livermore Software Technology (LSTC). (2020). LS-DYNA Keyword User's Manual, R12. LSTC.

Mavko, G., Mukerji, T., Dvorkin, J. (2009). Rock Physics Handbook (2nd Edition). Cambridge University Press.

Permanent International Association of Navigation Congress (PIANC). (2015). Guidelines for Protecting Berthing Structures from Scour Caused by Ships (Report No. 180). PIANC. Brussels, Belgium.

Poehlmann-Martins, F., Gabrys, J., & Souli, M. (2005). Hydrodynamic Ram Analysis of Non-Exploding Projectile Impacting Water. Proceedings of the ASME 2005 Pressure Vessels and Piping Conference, Denver, Colorado, USA, 267−273. https://doi.org/10.1115/PVP2005-71658

Prokopowicz, A.K., & Berg-Andreassen, J. (2016). An Evaluation of Current Trends in Container Shipping Industry, Very Large Container Ships (VLCSs), and Port Capacities to Accommodate TTIP Increased Trade. Transportation Research Procedia, 14, 2910−2919. https://doi.org/10.1016/j.trpro.2016.05.409

Roelse, F.P. (2014). Stability of Slope Material Affected by Bow Thrusters at Open Quay Structures (Master's Thesis). Delft University of Technology, Netherlands.

Rolls-Royce. (2013). Marine Products and Systems. Rolls-Royce plc.

Santini, P., Palmieri, D., & Marchetti, M. (1998). Numerical Simulation of Fluid-Structure Interaction in Aircraft Fuel Tanks Subjected to Hydrodynamic Ram Penetration. In 21st the International Council of the Aeronautical Sciences (ICAS) Congress, Melboume, Australia.

Seddon, C., Moodie, K. Thyer, A., & Moatamedi, M. (2004). Preliminary Analysis of Fuel Tank Impact. International Journal of Crashworthiness, 9(3), 237−244. https://doi.org/10.1533/ijcr.2004.0277

Souli, M., Ouahsine, A., & Lewin, L. (2000). ALE Formulation for Fluid-Structure Interaction Problems. Computer Methods in Applied Mechanics and Engineering, 190(5−7), 659−675. https://doi.org/10.1016/S0045-7825(99)00432-6

Tran, V.L., & Im, N. (2012). A Study on Ship Automatic Berthing with Assistance of Auxiliary Devices. International Journal of Naval Architecture and Ocean Engineering, 4(3), 199-210. https://doi.org/10.2478/IJNAOE-2013-0090

van Blaaderen, E.A. (2006). Modelling Bowthruster Induced Flow Near a Quay-Wall (Master's Thesis). Delft University of Technology, Netherlands.

van den Brink, A.J.W. (2014). Modelling Scour Depth at Quay Walls Due to Thrusters (Master's Thesis). Delft University of Technology, Netherlands.

Yeom, G.-S., Mizutani, N., Hur, D.-S., & Lee, W.-D., (2017). Application of a Modified Estimation Formula for Collision Force of Deformed Drifting Containers Under Tsunami Conditions. Journal of Coastal Research, 33(3), 720−730. https://doi.org/10.2112/JCOASTRES-D-15-00226.1

Yeom, G.-S., Nakamura, T., & Mizutani, N. (2009). Collision Analysis of Container Drifted by Runup Tsunami Using Drift Collision Coupled Model. Journal of Disaster Research, Fuji Technology Press, 4(6), 441−449. https://doi.org/10.20965/jdr.2009.p0441

Yu, C., & Yang, C. (2016). Study of Tunnel Thruster Performance and Flow by Quasi Steady Reynolds-Averaged Navier-Stokes Simulation. Journal of Shanghai Jiaotong University (Science), 21(6), 662−671. https://doi.org/10.1007/s12204-016-1779-z

Author ORCIDs

Author name	ORCID
Hwang, Taegeon	0000-0002-4959-3906
Yeom, Gyeong-Seon	0000-0002-3394-6527
Seo, Minjang	0000-0002-1897-3164
Lee, Changmin	0000-0003-4758-4341
Lee, Woo-Dong	0000-0001-7776-4664

KSOE

Journal of Ocean Engineering and Technology 35(6), 414-425, December, 2021
https://doi.org/10.26748/KSOE.2021.079

pISSN 1225-0767
eISSN 2287-6715

Original Research Article

A Review on the Building Wind Impact through On-site Monitoring in Haeundae Marine City: 2021 12th Typhoon OMAIS Case Study

Jongyeong Kim[1], Byeonggug Kang[1], Yongju Kwon[1], Seungbi Lee[2] and Soonchul Kwon[3]

[1]*Graduate Student, Department of Civil & Environmental Engineering, Pusan National University, Busan, Korea*
[2]*Assistant Manager, Technical Department, K-Watercraft, Busan, Korea*
[3]*Vice professor, Department of Civil & Environmental Engineering, Pusan National University, Busan, Korea*

KEY WORDS: Building wind, High-rise buildings, On-site monitoring, Typhoon, Risk analysis

ABSTRACT: *Overcrowding of high-rise buildings in urban zones change the airflow pattern in the surrounding areas. This causes building wind, which adversely affects the wind environment. Building wind can generate more serious social damage under extreme weather conditions such as typhoons. In this study, to analyze the wind speed and wind speed ratio quantitatively, we installed five anemometers in Haeundae, where high-rise buildings are dense, and conducted on-site monitoring in the event of typhoon OMAIS to determine the characteristics of wind over skyscraper towers surround the other buildings. At point M-2, where the strongest wind speed was measured, the maximum average wind speed in 1 min was observed to be 28.99 m/s, which was 1.7 times stronger than that at the ocean observatory, of 17.0 m/s, at the same time. Furthermore, when the wind speed at the ocean observatory was 8.2 m/s, a strong wind speed of 24 m/s was blowing at point M-2, and the wind speed ratio compared to that at the ocean observatory was 2.92. It is judged that winds 2–3 times stronger than those at the surrounding areas can be induced under certain conditions due to the building wind effect. To verify the degree of wind speed, we introduced the Beaufort wind scale. The Beaufort numbers of wind speed data for the ocean observatory were mostly distributed from 2 to 6, and the maximum value was 8; however, for the observation point, values from 9 to 11 were observed. Through this study, it was possible to determine the characteristics of the wind environment in the area around high-rise buildings due to the building wind effect.*

1. Introduction

Overcrowding and high-rise buildings in cities change the airflow pattern in the surrounding areas. Depending on the geometry, arrangement, and height of buildings, strong gusts and eddies are caused, lowering the wind comfort. The wind reflected by buildings is scattered to the surrounding area, causing various phenomena, such as localized gusts and eddies. These phenomena are collectively referred to as building wind. Building wind can always be found around buildings. It hardly causes problems around low-rise buildings, but the social damage caused by it has become an issue because more high-rise buildings have been built and the frequency of extreme weather events has increased. Thus, building wind has been established as a new form of urban pollution.

In countries, such as the United States, Japan, Germany, and the UK, it is mandatory to perform environmental impact assessments, following wind environment assessment guidelines and wind-way regulations, in the planning and design stages of the structure. As an example, the City of London in the UK provides general guidelines to be considered for designing a building in downtown London through the "Wind microclimate guidelines for developments in the city (City of London Corporation, 2019)" and performs preliminary impact assessments for building wind. It conducts wind tunnel tests, computational fluid dynamics (CFD) simulations, and cross-tabulation analyses according to the characteristics of the buildings because it is difficult to apply a unified standard due to the high variability in the field of turbulence. Meanwhile, the building design standards in South Korea suggest the design loads of buildings against the wind load, but do not present criteria for the impact of buildings on the surrounding area (Oh et al., 2020).

Recently, the building wind phenomenon has been recognized as a social problem, and the central and local governments have attempted to prepare measures. Basic research data, however, are still insufficient for preparing countermeasures suitable for the domestic situation. You et al. (2021) evaluated the wind environment around two apartment buildings using wind tunnel tests and CFD analyses. Choi et al. (2019)

Received 15 November 2021, revised 7 December 2021, accepted 8 December 2021
Corresponding author Soonchul Kwon: +82-51-510-7640, sckwon@pusan.ac.kr

compared the wind pressure coefficient and natural ventilation performance according to the apartment layout through CFD, and roughly categorized the characteristics of the wind pressure coefficient (ventilation performance) according to the position. Lee et al. (2021) analyzed the wind pressure characteristics of an open-center elliptical building through a wind tunnel test and compared them with the standards for building structures. In this study, changes in the wind environment in Haeundae due to the building wind effect were quantitatively analyzed by performing on-site monitoring of the building wind near the ground surface in the impact range of the 12th typhoon OMAIS in 2021 for the areas around high-rise buildings.

2. Definition of Building Wind

When the wind hits a building, its turbulence energy increases due to the friction and resistance effects and a high wind speed is generated locally. In addition, when the wind flows along passages or narrow gaps between buildings, the wind speed is increased by the Venturi effect. All the airflows that are generated around buildings are collectively referred to as building wind. The building wind phenomenon significantly varies depending on the geometry and arrangement of buildings or the surrounding conditions, as shown in Fig. 1.

In building and wind dynamics (Kim, 2018), the building wind is defined as follows. Separated flow occurs when the wind is separated to the left and right sides after hitting a building. The wind that passed the corner of the building has a higher wind speed than that at its surroundings. Downslope wind occurs when the wind separated to the left and right sides is sucked into the low-pressure area generated behind the building. Thus, it is fast and headed down on the side of the building. High-rise buildings are the main cause of building wind because the downslope wind generated when the fast wind above the ground hits a high-rise building affects the airflow near the ground surface. In general, as the altitude increases, the wind speed increases exponentially. Therefore, strong downslope wind is highly likely to occur around high-rise buildings. Valley wind is the strong wind formed between buildings due to the overlapping between the separated flow and downslope wind. Moreover, there is backward flow, which flows in the opposite direction to the wind in the sky after a collision with a building; pilotis wind, which flows rapidly along openings, such as pilotis; and upward flow, which rises with eddies near the corners of buildings. Behind buildings, windless zones with low wind speed are formed along with large and small eddies that are generated by unstable airflows.

3. On-site Monitoring

3.1 Research Site and Monitoring Points

The Marine City area in Haeundae-gu, Busan (Fig. 2) was selected as the research site because it is frequently damaged by building wind as it has a high density of high-rise buildings and is located in the coastal area vulnerable to storm and flood damage. In the area, high-rise apartment complexes, higher than 120 m, are densely located and there is also a skyscraper with a maximum height of approximately 301 m.

To observe the building wind in areas close to the high-rise buildings, fixed-type anemometers were installed in the research site. Through preliminary on-site measurements at 25 points during the invasion of the 9th typhoon Maysak and 10th typhoon Haishen in 2020, wind speed data were collected. The points with the highest wind speed were selected among the measurement points, and the anemometers were installed at five points (M-1 to M-5) as shown in Fig. 3. They were installed in structures located at the monitoring points at a height between 4.0 and 8.0 m considering the site conditions. The monitoring points were classified into the points at which the inflow of wind from the open sea is expected (M-1, 4, and 5), the points at which the highest wind speed was measured through the

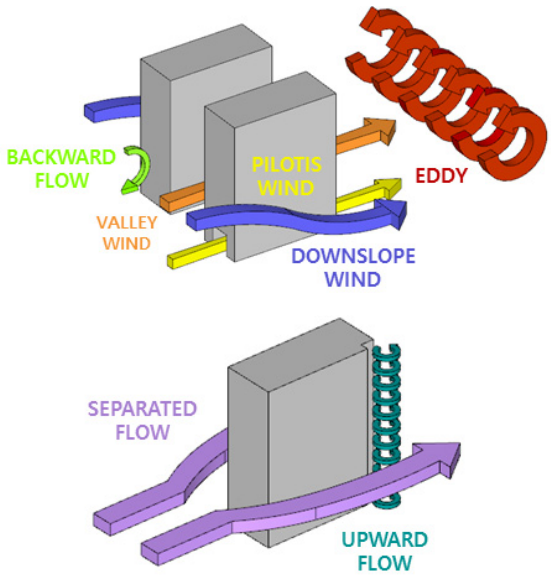

Fig. 1 Type of building wind

Fig. 2 Location and drone photo of research site

-

(a) Installation point (M1~5)

Latitude	Longitude
N 35° 09' 14"	E 129° 08' 49"

(b) View & coordinates of point M-1

Latitude	Longitude
N 35° 09' 18"	E 129° 08' 45"

(c) View & coordinates of point M-2

Latitude	Longitude
N 35° 09' 22"	E 129° 08' 46"

(d) View & coordinates of point M-3

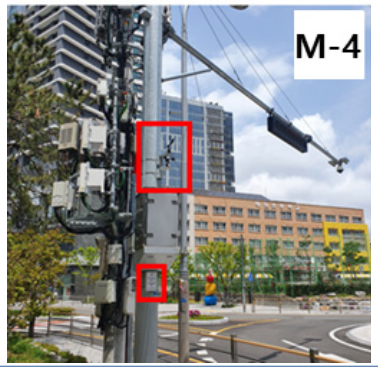

Latitude	Longitude
N 35° 09' 29"	E 129° 08' 35"

(e) View & coordinates of point M-4

Latitude	Longitude
N 35° 09' 17"	E 129° 08' 33"

(f) View & coordinates of point M-5

Fig. 3 Installation point of wind speed & wind direction observation equipment

preliminary on-site survey (M-1, 2, and 5), and the intersection points (M-2, 3, and 5).

3.2 Monitoring Equipment and Method

The equipment for monitoring the building wind was designed in accordance with the "Standard specifications for automatic weather observation equipment" (KMA, 2016). According to the "Standard specification of observation sensors" (article 7) of this standard, the equipment had the performance presented in Table 1. According to the "Standard for signal and data processing" (article 9), four data were acquired per second (345,600 data/day), and the 1-min average wind direction and wind speed were calculated by averaging data for 60 s (240 data).

Table 1 Specification of observation equipment

Windspeed (arco-serial)	Range	0–70 m/s
	Accuracy	± 2 %
	Resolution	0.1 m/s
Wind direction (arco-serial)	Range	0°–360°
	Accuracy	± 1°
	Resolution	1°

Latitude
N 35° 08' 56"
Longitude
E 129° 10' 12"
Observation rate
10 min

Fig. 4 Haeundae beach ocean observatory (Korea hydrographic and oceanographic agency)

The Haeundae beach ocean observatory operated by the Korea Hydrographic and Oceanographic Agency (Fig. 4) is located approximately 2 km east of Marine City (Fig. 2). Considering that the impact range of the building wind is wider than the height of the buildings (Kim and Im, 2012), the location of the ocean observatory is within the building wind impact range of LCT, a skyscraper. The ocean observatory, however, was selected as a comparison group because it is located in the area closest to the research site and in the sea, with relatively little interference. Given that building wind causes local

gusts within a short period of time (Roh, 2008), the 1-min average, which is the shortest time unit provided by the ocean observatory, was compared with the monitoring data of the research site.

3.3 The 12th Typhoon OMAIS

The 12th typhoon OMAIS in 2021 occurred in the sea, approximately 850 km south-southeast of Okinawa, Japan, at 21:00 on August 20th and disappeared at approximately 09:00 on August 24th. The record of the typhoon is presented in Table 2. The typhoon affected Korea from August 23rd, as shown in Fig. 5. Therefore, in this study, the data measured for 48 h from 00:00 on August 23rd to 00:00 on August 25th were analyzed.

Table 2 Record of typhoon OMAIS

Period	2021.08.20. 21:00 ~ 2021.08.24. 09:00
Intensity	Tropical storm
Size	Small storm (Diameter: 330 km)
Minimum air pressure	994 hPa
Maximum wind speed	26 m/s (1 min average)

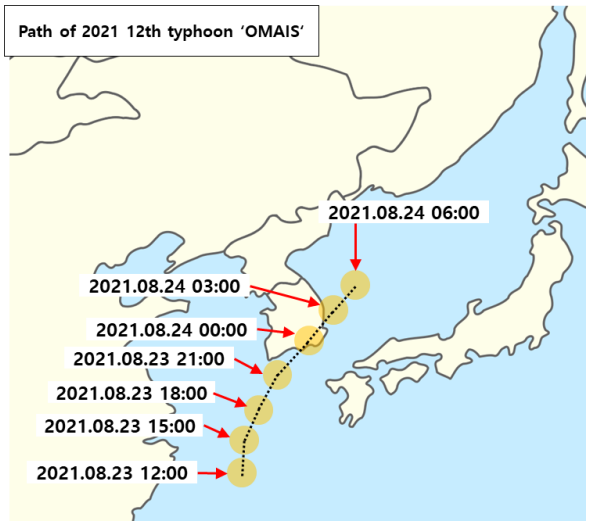

Fig. 5 Path of typhoon OMAIS

The building wind is evaluated using methods such as the strong wind occurrence probability (probabilistic evaluation method), wind speed increase rate (relative evaluation method), and allowed wind speed (absolute evaluation method). Given that the application of the probabilistic evaluation that predicts the strong wind occurrence frequency was judged to be difficult in this study considering the short-term (2 days) data and small number of samples, the relative and absolute evaluation methods were used for building wind evaluation. As for the relative evaluation method, the reference wind speed was that at the weather station (ocean observatory). The wind speed ratio (R) at each point compared to the reference wind speed was derived to calculate the wind speed increase rate by the building wind effect. as expressed in Eq. (1). In the case of the absolute evaluation method, the Beaufort wind scale proposed by Lawson and Penwarden (1975) was applied, as presented in Table 3.

$$windspeedratio(R) = \frac{windspeed_{M_i}}{windspeed_{oceanobservatory}(m/s)} \quad (1)$$

Table 3 Beaufort wind scale

Beaufort number	Description	Wind speed (m/s)
0	Calm	0–0.2
1	Light air	0.3–1.5
2	Light breeze	1.6–3.3
3	Gentle breeze	3.4–5.4
4	Moderate breeze	5.5–7.9
5	Fresh breeze	8.0–10.7
6	Strong breeze	10.8–13.8
7	Near gale	13.9–17.1
8	Gale	17.2–20.7
9	Severe gale	20.8–24.4
10	Storm	24.5–28.4
11	Violent storm	28.5–32.6
12	Hurricane	32.7–

4. Monitoring Results

4.1 One-minute Average Wind Speed of the Ocean Observatory

For the time period between 00:00 on August 23rd and 00:00 on August 25th, which was the impact range of typhoon OMAIS, the Marine City on-site monitoring data were compared with the 1-min average wind speed data of the ocean observatory.

Fig. 6 shows the 1-min average wind speed data (●) and the 1-h average wind direction to identify the atmospheric wind direction (➤), which were provided by the Haeundae beach ocean observatory. At the ocean observatory, a maximum wind speed of 18.5 m/s (southwest) was recorded as the first peak at 01:07 on August 24th after the invasion of the typhoon. At 06:00 on August 24th, a maximum wind speed of 15.5 m/s (southwest, west-southwest) was recorded as the second peak as the wind speed increased again even after the typhoon changed into an extratropical cyclone. The wind direction did not show a certain tendency when the observatory was in the indirect impact range of the typhoon. After 14:00 on August 24th when it was in the direct impact range of the typhoon, however, the wind direction was observed in the order of northeast → southeast → southwest, showing an obvious clockwise direction as in an area located on the right side of a typhoon's path.

4.2 Marine City Wind Speed and Wind Speed Ratio (Relative Evaluation)

Fig. 6 shows the 1-min average wind speed (■) and 1-h average wind direction (➪) measured at five points (M-1 to M-5) in Marine

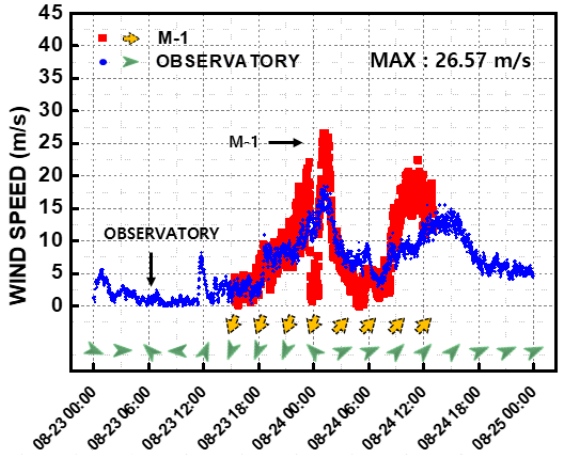

(a) Wind speed comparison (M-1 ■ vs Ocean Observatory ●)

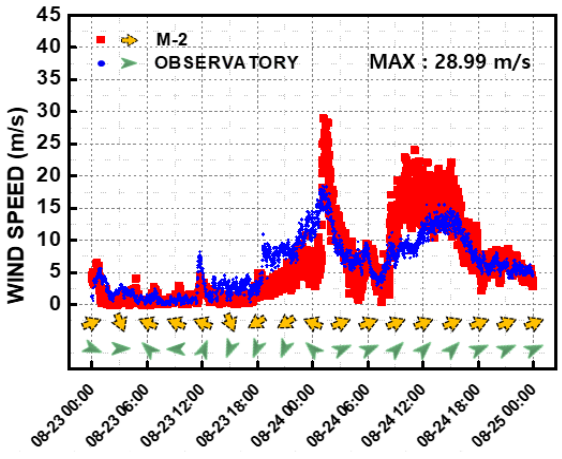

(b) Wind speed comparison (M-2 ■ vs Ocean Observatory ●)

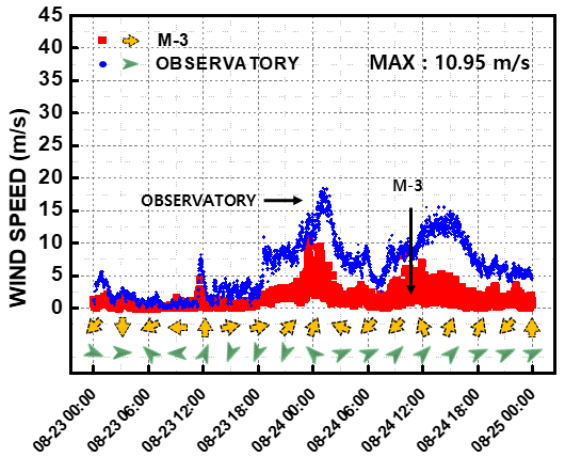

(c) Wind speed comparison (M-3 ■ vs Ocean Observatory ●)

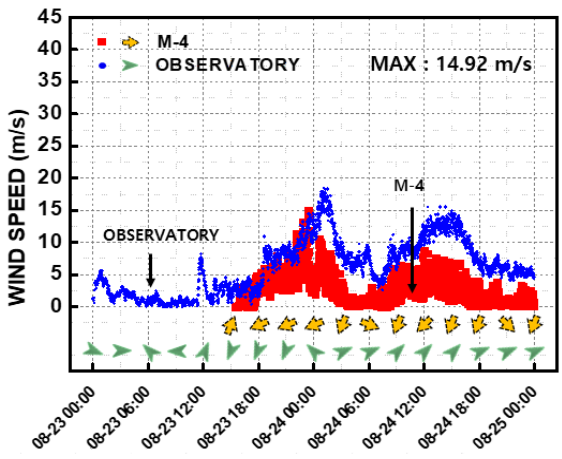

(d) Wind speed comparison (M-4 ■ vs Ocean Observatory ●)

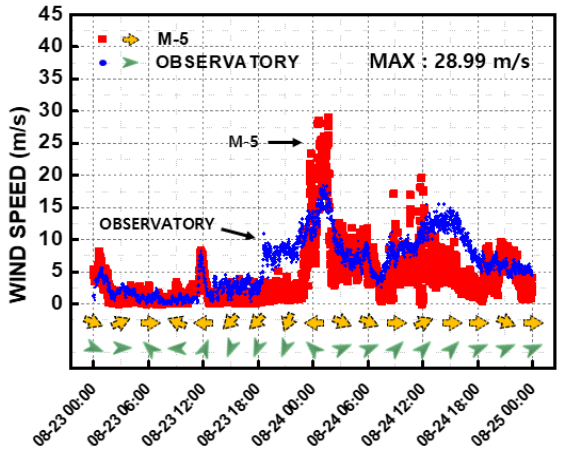

(e) Wind speed comparison (M-5 ■ vs Ocean Observatory ●)

Fig. 6 Comparison of wind speed at each point (Marine City vs Ocean Observatory)

City. Fig. 7 shows the wind speed ratio at each point (▲, ■) by applying Eq. (1). As for the calculation of the wind speed ratio, time points at which the wind speed was not measured were excluded. Some wind speed ratios were excessive (5 to 25), and this appears to be because the wind speed measured at the ocean observatory was relatively low. Therefore, in this study, the wind speed ratio was calculated for cases where the wind speed at the ocean observatory was 2 m/s or higher to derive the wind speed ratio at significant wind speed.

4.2.1 Point M-1

Point M-1 was located on the eastern part of the Marine City coastal road. Given that it was directly in contact with the coast, the easterly

sea wind could be measured without interference. As it was located on the side of a high-rise building, high wind speed caused by the separated flow and downslope wind was expected.

Fig. 6(a) shows the 1-min average wind speed at point M-1. The maximum wind speed (at 01:16 on August 24th) was measured to be 26.57 m/s (southwest) and the wind speed at the ocean observatory at

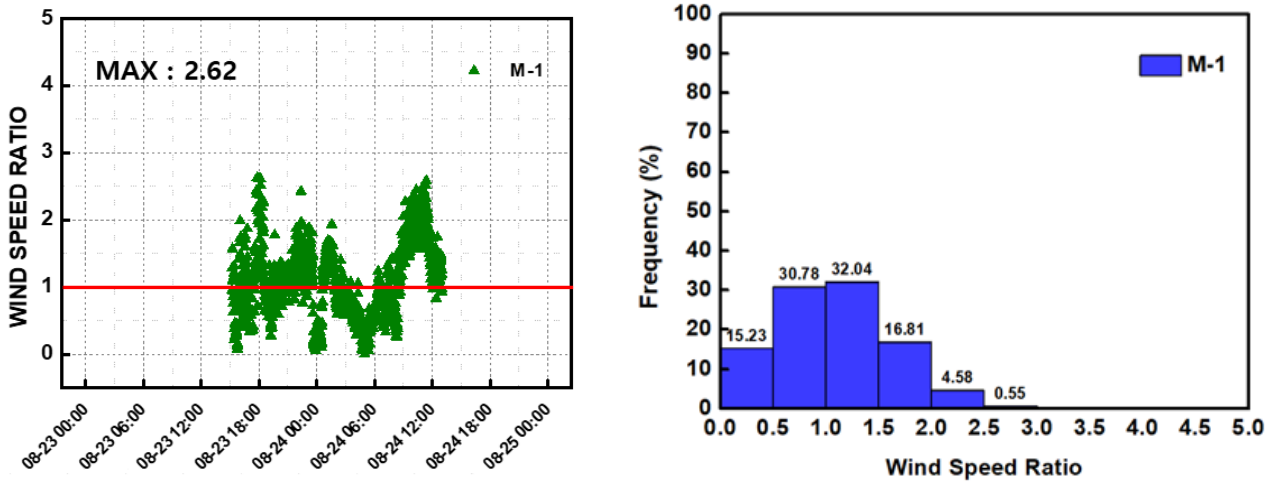

(a) Wind speed ratio ($Windspeed_{M-1}/Windspeed_{OceanObservatory}$ ▲, ■)

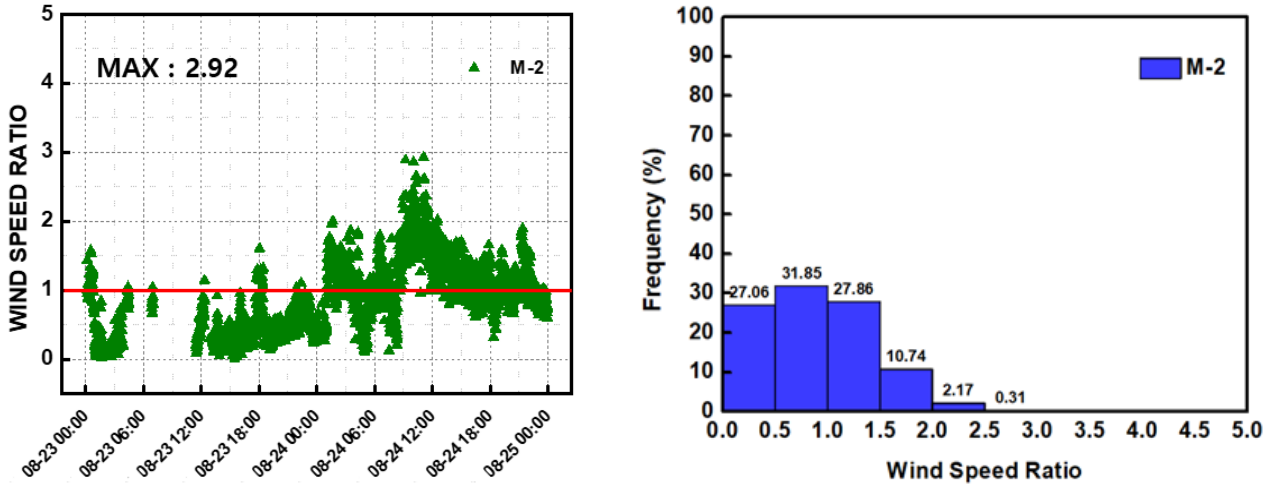

(b) Wind speed ratio ($Windspeed_{M-2}/Windspeed_{OceanObservatory}$ ▲, ■)

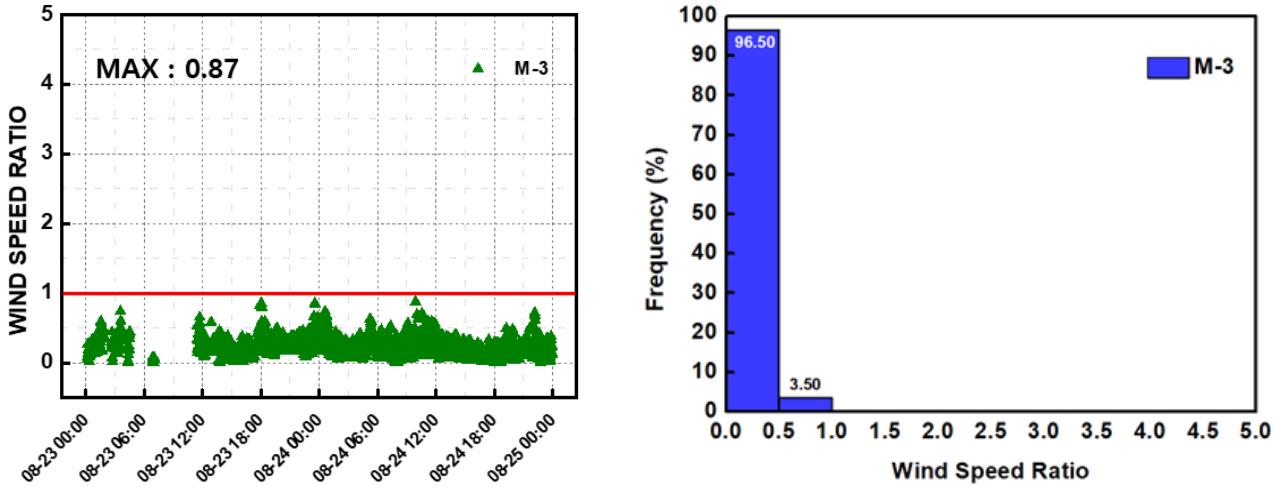

(c) Wind speed ratio ($Windspeed_{M-3}/Windspeed_{OceanObservatory}$ ▲, ■)

Fig. 7 Frequency distribution of wind speed ratio at each point (Marine City/Ocean Observatory) (Continuation)

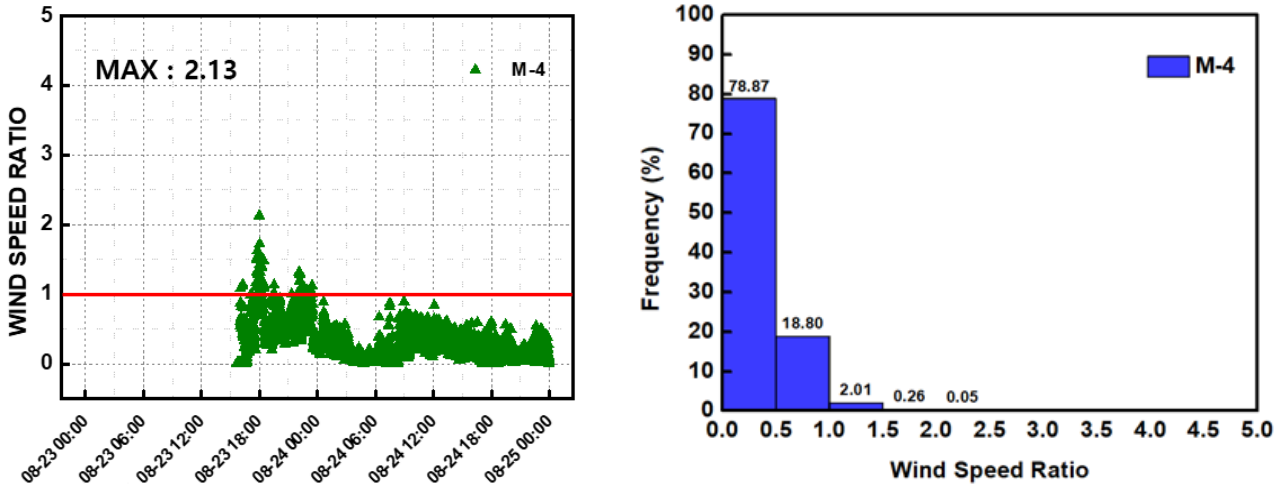

(d) Wind speed ratio ($Windspeed_{M-4}/Windspeed_{OceanObservatory}$ ▲, ■)

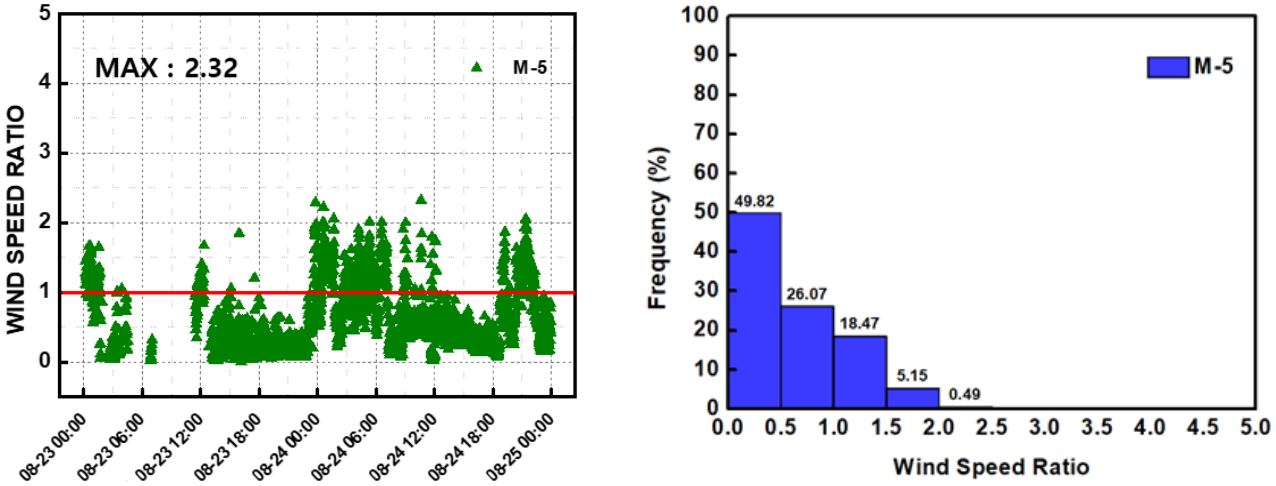

(e) Wind speed ratio ($Windspeed_{M-5}/Windspeed_{OceanObservatory}$ ▲, ■)

Fig. 7 Frequency distribution of wind speed ratio at each point (Marine City/Ocean Observatory)

the same time was 16.9 m/s (southwest), indicating that the wind speed at point M-1 was 1.57 times higher.

The wind speed ratio at point M-1 ranged from 0 to 2.62 as shown in Fig. 7(a). The maximum wind speed ratio (at 17:49 on August 23rd) was found to be 2.62 when the wind speed at point M-1 was 5.51 m/s (north-northeast) and that at the ocean observatory was 2.1 m/s (northeast). Wind speed ratios less than 1.0 accounted for 46% of the wind speeds, whereas those equal to or higher than 1.0 represented 54% of them, indicating that 54% of the wind speeds were higher than the reference wind speed due to the building wind effect.

Point M-1 was located on the side of a building (Fig. 8). Therefore, the wind direction was parallel to the direction of the outer wall of the building. The north-northeast wind direction was mostly observed when the atmospheric wind direction was north, and the southwest wind direction when it was south. The wind speed ratio tended to be high when the atmospheric wind direction was parallel to the outer wall direction as in the time periods between 18:00 and 22:00 on August 23rd and between 09:00 and 12:00 on August 24th.

Fig. 8 Main wind direction (M-1)

4.2.2 Point M-2

At point M-2, a 10-s average wind speed of approximately 30 m/s (an instantaneous wind speed of 46 m/s) was measured through on-site

observation during the invasion of 9th typhoon Maysak in 2020. Given that point M-2 was located at an intersection between high-rise buildings, high wind speed caused by valley wind was predicted.

Fig. 6(b) shows the 1-min average wind speed at point M-2. The maximum wind speed (at 01:10 on August 24th) was measured to be 28.99 m/s (southwest) and the wind speed at the ocean observatory at the same time was 17 m/s (southwest), showing that the wind speed at point M-2 was 1.70 times higher.

The wind speed ratio at point M-2 ranged from 0 to 2.92 as shown in Fig. 7(b). The maximum wind speed ratio (at 11:06 on August 24th) was found to be 2.92 when the wind speed at point M-2 was 24 m/s (southwest) and that at the ocean observatory was 8.2 m/s (southwest). Wind speed ratios less than 1.0 accounted for 59% of the wind speeds, whereas those equal to or higher than 1.0 represented 41% of them, meaning that 41% of the wind speeds were higher than the reference wind speed due to the building wind effect. At point M-2, the wind speed ratio tended to be high under the southwest wind condition (after 09:00 on August 24th). This appears to be because the wind speed was further increased by the downslope wind as high-rise buildings were densely located on the west side of point M-2.

4.2.3 Point M-3

At point M-3, large social damage occurred, including damage to many windows in shopping malls, during the invasion of 9th typhoon Maysak in 2020. In addition, as point M-3 was located at an intersection close to high-rise buildings, as was the case with point M-2, high wind speed caused by valley wind was predicted.

Fig. 6(c) shows the 1-min average wind speed at point M-3. The maximum wind speed (at 23:33 on August 23rd) was measured to be 10.95 m/s (south-southwest) and the wind speed at the ocean observatory at the same time was 12.8 m/s (southeast), showing that the wind speed at point M-3 was lower.

The wind speed ratio at point M-3 ranged from 0 to 0.87, as shown in Fig. 7(c). The maximum wind speed ratio (at 09:55 on August 24th) was found to be 0.87 when the wind speed at point M-3 was 8.64 m/s (east-southeast) and that at the ocean observatory was 9.2 m/s (southwest). Wind speed ratios less than 1.0 represented 100% of the wind speeds, indicating that all wind speeds were lower than the reference wind speed. Although point M-3 was located at an intersection close to point M-2 with a distance of approximately 230 m, the increase in wind speed caused by building wind did not occur and the wind speed rather sharply decreased. This appears to be due to the energy dissipation effect of the trees (Fig. 9) in the apartment complexes adjacent to point M-3.

Given that point M-3 was located at an intersection, as was the case with point M-2, the wind was observed in 360° directions. While point M-2 was highly correlated to the wind direction at the ocean observatory, the wind direction at point M-3 was less correlated. This appears to be due to the generation of a complex airflow pattern caused by the turbulence created in the energy dissipation process by the trees.

Fig. 9 Wind break forest around M-3

4.2.4 Point M-4

As point M-4 was located in the western part of the Marine City area, it was expected that the westerly sea wind could be measured. However, due to the influence of the trees (Fig. 10) planted in the Pusan Yachting Center, as was also the case with point M-3, relatively low wind speed was observed.

Fig. 6(d) shows the 1-min average wind speed at point M-4. The maximum wind speed (at 23:27 on August 23rd) was measured to be 14.92 m/s (northeast) and the wind speed at the ocean observatory at the same time was 13.3 m/s (east-southeast), indicating that the wind speed at point M-4 was 1.12 times higher.

The wind speed ratio at point M-4 ranged from 0 to 2.13 as shown in Fig. 7(d). The maximum wind speed ratio (at 18:00 on August 23rd) was found to be 2.13 when the wind speed at point M-4 was 4.26 m/s (east) and that at the ocean observatory was 2.0 m/s (northeast). Wind speed ratios of 1.0 or higher accounted for only 2.3% of the wind speeds, whereas wind speed ratios less than 1.0 represented 97.7% of them, and 79% of the cases showed a wind speed ratio less than 0.5. It appears that the low wind speed at point M-4 was also caused by the energy dissipation effect of the trees.

Fig. 10 Wind break forest around M-4

4.2.5 Point M-5

Point M-5 was located in the southern part of the Marine City coastal road. As it was directly in contact with the coast, the southerly sea wind could be measured. Due to the location of point M-5 at the corner of a high-rise building, high wind speed caused by the separated wind was expected.

Fig. 6(e) shows the 1-min average wind speed at point M-5. The maximum wind speed was measured to be 28.99 m/s (west-southwest) at 01:40 on August 24th. In this instance, the wind speed at the ocean observatory was 14.1 m/s (southwest), showing that the wind speed at point M-5 was 2.05 times higher.

The wind speed ratio ranged from 0 to 2.32 as shown in Fig. 7(e). The maximum wind speed ratio (at 10:38 on August 24th) was found to be 2.32 when the wind speed at point M-5 was 16.96 m/s (west) and that at the ocean observatory was 7.3 m/s (southwest). Wind speed ratios less than 1.0 accounted for 76% of the wind speeds, whereas those equal to or higher than 1.0 represented 24% of them, indicating that 24% of the wind speeds were higher than the reference wind speed due to the building wind effect.

Given that point M-5 was located on the side of a building (Fig. 11), east and west wind directions parallel to the building's outer wall direction were mostly observed. The wind speed ratio was higher when the atmospheric wind directions were east and west than when they were south and north.

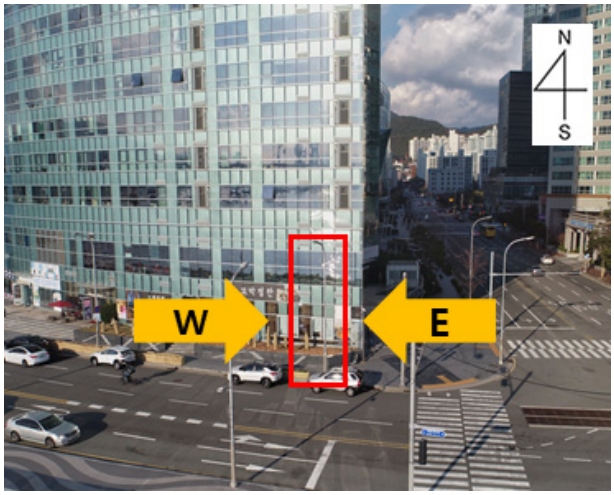

Fig. 11 Main wind direction (M-5)

4.3 Beaufort Number at Marine City Points (Absolute Evaluation)

In Section 4.2, the wind speed increase rate was analyzed through a relative evaluation. As the damage created by wind is caused by high wind speed, it is necessary to evaluate the absolute value of the increase in wind speed generated by the building wind effect. Therefore, the Beaufort wind scale (Table 3) was applied to the wind speed data measured at the ocean observatory and five points in Marine City (M-1 to M-5), and the frequency of the Beaufort number is shown in Fig. 12. Missing data and Beaufort number 0 (calm) were excluded for the convenience of data analysis.

For the wind speed data measured at the ocean observatory, the Beaufort number ranged from 0 to 9. The proportions of Beaufort numbers from 0 to 8 were 1.88%, 15.50%, 14.74%, 13.59%, 21.29%, 16.93%, 11.88%, 3.62%, and 0.56%, respectively, indicating that the numbers were relatively evenly distributed from 1 to 6. The mode was found to be 4 (moderate breeze) and the maximum value was 8 (gale). The results at each point are shown in Figs. 12(a) to 12(e).

Fig. 12(a) shows the Beaufort numbers of wind speeds measured at point M-1(■). The numbers ranged from 0 to 10, and their proportions were 5.42%, 16.42%, 18.72%, 11.76%, 12.45%, 8.94%, 13.83%, 8.10%, 2.52%, and 1.53%, respectively. The mode was found to be 3 (gentle breeze) and the maximum value was 10 (storm). Compared to the wind speed data at the ocean observatory, Beaufort numbers 1, 4, 5, and 6 showed a decrease in frequency, whereas Beaufort numbers 2, 3, 7, and 8 presented an increase in frequency. Wind speeds corresponding to Beaufort numbers 9 and 10 (20.8 to 28.4 m/s), which were not observed at the ocean observatory, were observed here.

Fig. 12(b) shows the Beaufort numbers of the wind speeds measured at point M-2(■). The numbers ranged from 0 to 11, and their proportions were 25.31%, 12.62%, 14.85%, 15.86%, 5.67%, 5.49%, 7.37%, 5.60%, 1.08%, 0.56%, and 0.03%, respectively. The mode was found to be 1 (light air) and the maximum value was 11 (violent storm). Compared to the wind speed data at the ocean observatory, Beaufort numbers 2, 4, 5, and 6 showed a decrease in frequency, whereas numbers 1, 3, 7, and 8 presented an increase in frequency. Wind speeds corresponding to Beaufort numbers 9, 10, and 11 (20.8 to 32.6 m/s), which were not observed at the ocean observatory, were observed here.

Fig. 12(c) shows the Beaufort numbers of wind speeds measured at point M-3(■). The numbers ranged from 0 to 6, and their proportions were 51.30%, 26.93%, 4.66%, 1.54%, 0.46%, and 0.04%, respectively. The mode was found to be 1 (light air) and the maximum value was 6 (strong breeze). Compared to the wind speed data at the ocean observatory, Beaufort numbers from 3 to 6 showed a decrease in frequency, whereas numbers 1 and 2 had a significant increase in frequency.

Fig. 12(d) shows the Beaufort numbers of wind speeds measured at point M-4(■). The numbers ranged from 0 to 7, and their proportions were 29.67%, 25.62%, 24.53%, 8.04%, 2.80%, 0.52%, and 0.05%, respectively. The mode was found to be 1 (light air) and the maximum value was 7 (near gale). Compared to the wind speed data at the ocean observatory, Beaufort numbers from 4 to 7 showed a decrease in frequency, whereas numbers from 1 to 3 presented a significant increase in frequency.

Fig. 12(e) shows the Beaufort numbers of wind speeds measured at point M-5(■). The numbers ranged from 0 to 11, and their proportions were 27.50%, 21.41%, 17.72%, 14.76%, 6.54%, 1.39%, 0.66%, 1.15%, 1.39%, 0.70%, and 0.07%, respectively. The mode was found to be 1 (light air) and the maximum value was 11 (violent storm). Beaufort numbers from 4 to 7 showed a decrease in frequency, whereas numbers 1, 2, 3, and 8 had an increase in frequency. Wind speeds corresponding to Beaufort numbers 9, 10, and 11 (20.8 to 32.6 m/s), which were not

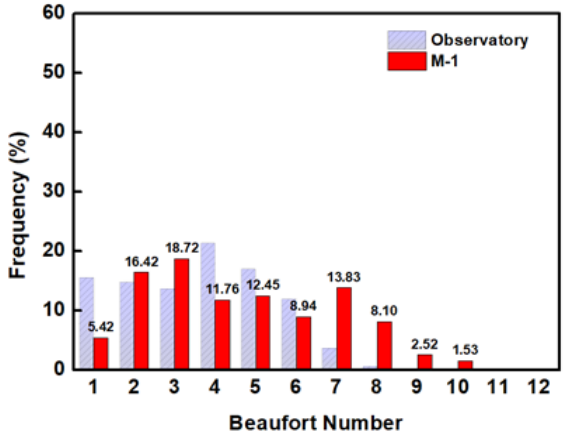

(a) Beaufort number (M-1 ■ vs Ocean Observatory ■)

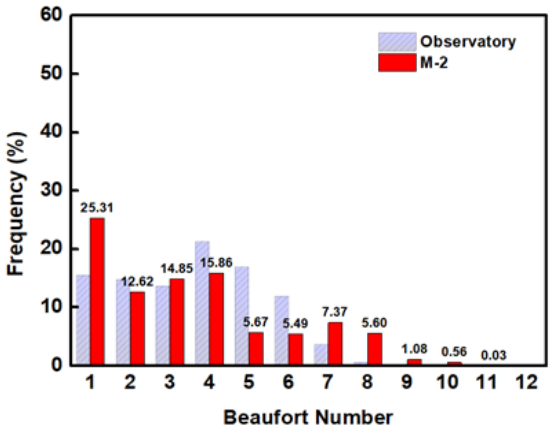

(b) Beaufort number (M-2 ■ vs Ocean Observatory ■)

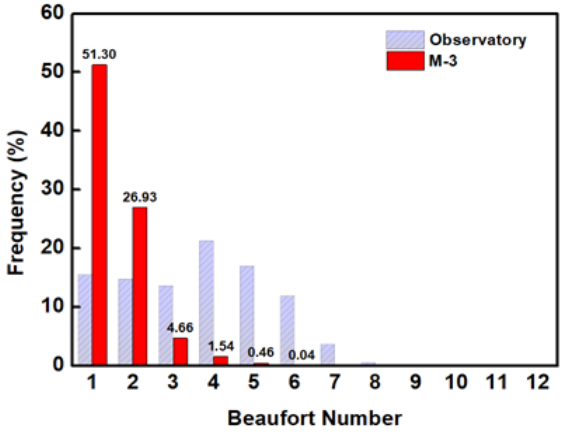

(c) Beaufort number (M-3 ■ vs Ocean Observatory ■)

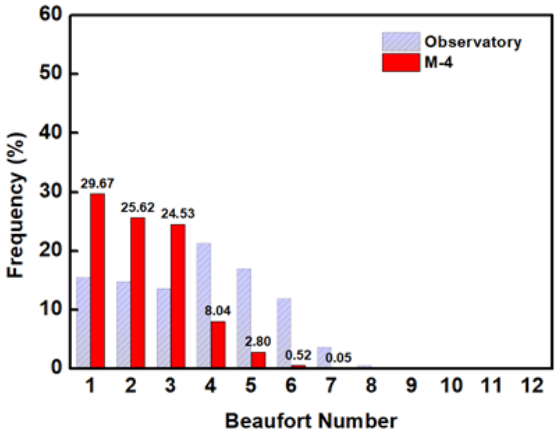

(d) Beaufort number (M-4 ■ vs Ocean Observatory ■)

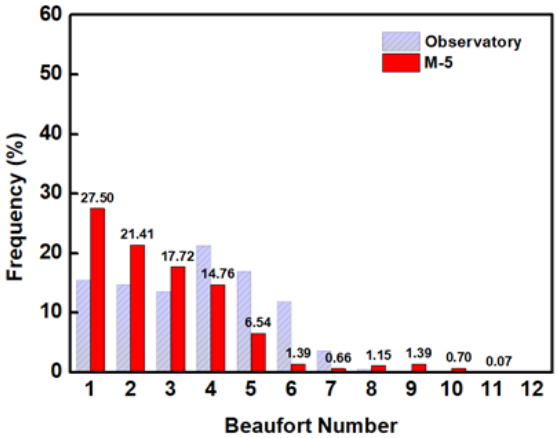

(e) Beaufort number (M-5 ■ vs Ocean Observatory ■)

Fig. 12 Frequency of Beaufort numbers at each point (Marine City vs Ocean Observatory)

observed at the ocean observatory, were observed at this point.

At points M-1, M-2, and M-5, where the wind speed increased, Beaufort numbers from 4 to 6 (5.5 to 13.8 m/s) tended to show a decrease in frequency, whereas numbers from 1 to 3 (0.2 to 5.4 m/s) and 7 to 11 (13.9 to 32.6 m/s) presented an increase in frequency. In other words, the wind speed corresponding to the middle classes was decreased by the blockage of buildings or increased by the building wind effect depending on the conditions. It is considered necessary to conduct further research on factors that affect building wind through long-term monitoring. Meanwhile, at points M-3 and M-4, where the wind speed decreased due to the wind-proof effect of trees, Beaufort numbers of 4 and above (over 7.9 m/s) tended to show a significant decrease in frequency, whereas Beaufort numbers from 1 to 3 (0.2 to 5.4 m/s) had a significant increase in frequency.

5. Conclusion

To evaluate the building wind effect on the approach of typhoon, we investigated the characteristics of wind profile over skyscraper towers surround the other buildings in Haeundae region, Busan, South Korea. In this study, five anemometers were installed in Haeundae Marine City where high-rise buildings are densely located and on-site monitoring of typhoon OMAIS was performed to examine the building wind phenomenon. For result analysis, a relative evaluation through the calculation of the wind speed ratio (wind speed increase rate) and an absolute evaluation based on the Beaufort wind scale were performed. The following conclusions could be drawn.

(1) Among points M-1, M-2, and M-5 at which the wind speed was significantly increased, point M-2 had the highest wind speed, showing a maximum wind speed of 28.99 m/s and a maximum wind speed ratio of 2.92. Different building wind patterns were observed depending on the location characteristics of each point. At points M-1 and M-5, which were located on the side of a high-rise building, the main wind direction was found to be parallel to the building direction and the wind speed ratio was high when the atmospheric wind direction was parallel to the building outer wall direction. The wind direction at point M-2, which was located at an intersection, was highly correlated with that at the ocean observatory located in the sea, and the wind speed ratio was high when the atmospheric wind direction was west. This appears to be because high-rise buildings were located on the west side of point M-2. At points M-3 and M-4, the wind speed ratio was found to be less than 1 and the wind speed rather decreased even though they were located in areas where high-rise buildings were densely located. This appears to be due to the influence of the trees planted near the observation equipment. A previous study (Kim et al., 2013) analyzed the wind-proof effect of planting windbreak forest through a wind tunnel test, and it confirmed that the windbreak forest has the effect of decreasing the wind speed by at least 47%. In this study, the wind-proof effect of trees could also be observed through actual monitoring data.

(2) When the absolute values of the wind speed were analyzed through the Beaufort wind scale, it was found that Beaufort numbers from 7 to 11, which belong to the dangerous wind speed range, showed an increase in frequency at points M-1, M-2, and M-5, where the wind speed was significantly increased. Beaufort numbers from 1 to 3, which correspond to low wind speeds, also showed an increase in frequency. This indicates that the wind speed was decreased by the blockage effect of buildings or increased by the building wind effect depending on the conditions. Thus, further research is required on various variables that cause building wind. At points M-3 and M-4, where the wind speed decreased due to the wind-proof effect of trees, the degree of decrease in wind speed could be quantitatively identified because Beaufort numbers of 4 and above showed a significant decrease in frequency, whereas those from 1 to 3 presented a significant increase in frequency.

Fig. 13 Risk analysis at each point

(3) Based on the above results, the areas with risk due to building wind are shown in Fig. 13. As the number of measurement points is small compared to the range of the research site, it is difficult to identify the risk level for all sections in the site. It seems necessary to perform high-density monitoring by installing more monitoring points or to utilize computational fluid dynamics (CFD) to identify the risk level for the entire range of the research site. It is also considered necessary to conduct further research with high reliability through cross-analysis between monitoring and CFD.

(4) In addition, 1-min average data were used for a comparison with the wind speed data of the ocean observatory, but it is considered necessary to analyze the 3-s average (instantaneous wind speed) or 1-s average wind speed data due to the characteristics of the building wind, which may cause gusts and damage within a short period of time. As an example, at point M-2 where the highest wind speed was observed, the maximum wind speed was calculated to be 48.24 m/s when the 3-s average wind speed was used and 53.20 m/s when the 1-s average wind speed was used. These were 1.66 and 1.83 times higher than 28.99 m/s, which was the maximum average wind speed for 1 min. Given that the outer walls, windows, and glass of buildings can be damaged even by momentary strong winds, it is necessary through further research to analyze the risk level of the building wind using an average wind speed with a short period.

Conflict of Interest

No potential conflict of interest relevant to this article was reported.

Funding

This research was supported by a grant (20011068) of Regional Customized Disaster-Safety R&D Program funded by Ministry of Interior and Safety (MOIS, Korea).

References

Choi, J.S., Kim, E.J., & Yoon, S.H. (2019). A Study on the Comparison of Wind Pressure Coefficient and Natural Ventilation Performance According to the Layout of Apartment Complex. Journal of Korean Institute of Architectural Sustainable Environment and Building Systems, 13(5), 315-324. https://doi.org/10.22696/jkiaebs.20190027

City of London Corporation (2019). Wind Microclimate Guidelines for Developments in the City of London, 1-15. Retrieved from https://in2.ie/wp-content/uploads/2019/11/city-of-london-wind-microclimate-guidelines.pdf

Kim, H.L. (2018). Building and Wind Dynamics. Seoul, Korea: Ilgwang

Kim, H.J., Kim. H.S., Jung, S.H., & Lee, S.H. (2013). Analysis on Effects of Protection Against Wind According to Tree Species and Planting Methods of the Wind Break Forest Based on the Wind Tunnel Experiment. Preceedings of 2013 Forest Science Joint Conference of Korean Institute of Forest Recreation and Welfare, 791-794.

Kim, J.D., & Im, J.T. (2012). Wind-Resistant Design of Tall Building using CFD. Computational Structural Engineering, 25(2), 21-24

Lawson, T.V., & Penwarden, A.D. (1975). The Effectss of Wind on People in the Vicinity of Buildinbg. Proceedings of 4th International Conference on Wind Effects on Buildings and Structures, Cambridge University Press, Heathrow, 605-622.

Lee, J.H., Cheon, D.J., Kim, Y.C., & Yoon, S.W. (2021). Investigation of Peak Pressure Coefficient of Central Open Elliptical Dome Roof by Wind Tunnel Test. Journal of Architectural Institute of Korea, 37(9), 189-197. https://doi.org/10.5659/JAIK.2021.37.9.189

Oh, S.H., Kwon, S.C., Kim, J.C. & Lee, K.W. (2020). Review of Hazardous Areas Through the Field Observation of Building Wind at Pedestrian Height - Concentrated on the 2020 9th Typhoon -. Journal of the Regional Association of Architectural Institute of Korea, 22(6), 151-157.

Roh, J.W. (2008). Example Study on Building Wind of Apartment Complex by Computational Fluid Dynamics - About Two apartment Complex in Cheon-An Region -. Korea Institute of Ecological Architecture and Environment, 8(4), 37-42.

Korea Meteorological Administration. (2016). Standard Specifications for Automatic Weather Observation Equipment. Korea Meteorological Administration.

You, J.Y., Nam, B.H., Park, M.W., & You, K.P. (2021). Comparison for Assessment of Wind Environment in High-rise Buildings Using Wind Tunnel Test and Computational Fluid Dynamics. Journal of Architectural Institute of Korea, 37(5), 163-171. https://doi.org/10.5659/JAIK.2021.37.5.163

Author ORCIDs

Author name	ORCID
Kim, Jongyeong	0000-0001-6642-8622
Kang, Byeonggug	0000-0003-4057-4386
Kwon, Yongju	0000-0001-7935-8416
Lee, Seungbi	0000-0003-4723-9628
Kwon, Soonchul	0000-0003-3764-331X

KSOE

Journal of Ocean Engineering and Technology 35(6), 426-433, December, 2021
https://doi.org/10.26748/KSOE.2021.072

pISSN 1225-0767
eISSN 2287-6715

Original Research Article

Evaluating the Mechanical Properties of Fiber Yarns for Developing Synthetic Fiber Chains

Kyeongsoo Kim[1], Taewan Kim[2], Namhun Kim[1], Dokyoun Kim[3], Yongjun Kang[3] and Seonjin Kim[2]

[1]*Senior Researcher, Special Ships Advanced Technology Center, Research Institute of Medium & Small Shipbuilding, Busan, Korea*
[2]*Professor, Department of Mechanical Engineering, Pukyong National University, Busan, Korea*
[3]*Director, Technical Research Center, DSR. Corp., Busan, Korea*

KEY WORDS: Fiber chain, Synthetic fiber, Stiffness, Time to rupture, Durability

ABSTRACT: *In this study, three types of synthetic fiber materials were evaluated, namely, DM20, SK78, and T147, to replace steel chains in shipbuilding and offshore fields with fiber chains as there is increasing demand for chains with lighter weights and improved usabilities. The strength and quasi-static stiffness were analyzed to select suitable yarns for the fiber chains. The durability of the yarn was evaluated by performing a 3-T (time to rupture) test as a specific tension level. The results of the experiment revealed excellent dynamic stiffness in DM20 and highest values of the windward and leeward stiffness in T147. 3-T linear design characteristic curves for a specific tension level were derived for the three types of fiber materials. The findings of this study can provide insights for improving strength and durability in fiber chain design.*

1. Introduction

Link chains used in general industrial applications are formed by linking several steel rings, and these are used to connect a crane or winch for transporting heavy objects or lashing heavy objects to a designated location. Among the types of link chains, a load chain is representative, and for the field application of load chains, the wire diameter of the chain has to be increased according to the required load of application. However, in steel chains, as the wire diameter increases with increase in the working load, the weight of the chain increases in proportion; this compromises the workability and limits the application scope. Therefore, for using these chains in field applications, the weight of steel chains has to be reduced and the operation has to be made easier. These chains are subjected to high tension conditions during operation, such as gradual increase in the tensile force, peak load from external forces, and prolonged application of cyclic loading; therefore, these and various other load conditions should be considered in the research and development of fiber chains.

Steel is mostly used in industrial applications, but synthetic fiber has been used for a long time in mooring systems for ships and offshore structures. Among synthetic fiber chains used for lifting large loads, synthetic fiber ropes were first proposed for use as mooring lines in the 1960s, and since then, extensive studies have been conducted for practical use of synthetic fiber ropes (Banfield and Casey, 1998). Del Vecchio (1992) were the first to carry out systematic research on the mechanical behavior of polyester ropes. They examined the dynamic stiffness, creep, and fatigue behavior of polyester ropes; these are essential characteristics for application of polyester ropes in deepwater moorings. Petruska et al. (2010) installed the first offshore polyester mooring system in the Campos Basin, Brazil. Over time, polyester ropes have become the preferred option of mooring line installation up to a depth of 1500 m. However, with increasing number of natural resources being discovered at increasing water depths, it remains to be explored whether polyester ropes can be utilized at these depths and whether they can provide sufficient stiffness to maintain adequate platform offsets (Davies et al., 2002). As the offshore oil and gas surveys moved to the deep seas, mooring with polyester ropes faced two challenges. The first problem is the size and weight of polyester ropes that are often considerably thick and long, which may exceed the allowable capacity of anchor handling boats and cause problems in installation (Chi et al., 2009; Det Norske Veritas, 2018). The second problem is that polyester ropes can have large elongations, which may lead to horizontal offsets exceeding the riser limit at depths of >2000 m (Fernandes et al., 1999).

Received 5 October 2021, revised 11 November 2021, accepted 15 November 2021
Corresponding author Seonjin Kim: +82-51-629-6163, sjkim@pknu.ac.kr

To address the limitations of the polyester material, ultra-high-molecular-weight polyethylene (UHMWPE), also known as high-modulus polyethylene (HMPE), was developed, and it has been widely applied as the most suitable material for deep-sea mooring lines. HMPE ropes are lighter than polyester ropes under equivalent minimum breaking load conditions and have smaller diameters and higher stiffnesses. Thus, HMPE ropes have technical as well as operational advantages over traditional polyester ropes for applications in deep-sea mooring (Peter et al., 2011; Davies et al., 2015). HMPE mooring systems with high stiffness are more riser friendly in terms of offset than polyester mooring lines, and HMPE ropes typically break at 2%–2.5% elongation after use when polyester ropes break at 12%-15% elongation. While the positions of offshore structures are held static, the waves apply a cyclic load on the mooring lines, which changes the fiber elongation, and thus, the mooring line is subjected to an extension-retraction fatigue load. In one study, an HMPE rope showed a longer fatigue life than a polyester rope with the same structure, and its axial compression fatigue properties were not inferior to those of an aramid fiber sample (Garrity and Fronzaglia, 2008, Leite and Boesten, 2011). A hybrid rope prepared as a combination of HMPE and polyester has been proposed for mooring systems located in storm and hurricane risk areas where rope stiffness and elasticity are required at the same time. Theoretical and numerical studies of polyester mooring lines for coupled dynamic analysis with deep-sea floating platforms have been conducted (Bunsell et al., 2009, S. Leite et al., 2011, Tahar and Kim, 2008).

The mechanical behavior of synthetic fiber ropes directly impacts mooring responses (Weller et al., 2014). Berryman et al. (2002) examined the residual strength of HMPE ropes for use in mooring lines of mobile offshore drilling units (MODUs) for 110 days; the results showed that the HMPE rope was still in good condition compared to the initial test specimen state. Williams et al. (2002) performed small-scale static tensile testing using polyester elements and sub-rope components to examine damaged ropes. Ward et al. (2006) conducted the length to diameter ratio effect tests on polyester ropes used for mooring to determine the effect of damage on their residual strengths and developed guidelines for mitigating damage in polyester rope mooring lines. Da Costa Mattos and Chimisso (2011) modeled creep tests of HMPE fibers used in ultra-deep-sea mooring ropes and compared the expected lifetime and elongation (%) of the test specimens at various load levels and temperatures. Cedric et al. (2020) analyzed the extension load sensitivity characteristics of HMPE ropes according to the initial load change, and Gen el. al. (2021) conducted an experimental study on the dynamic stiffness of full-size HMPE ropes under long-term cyclic loading conditions.

Several studies have proposed polyester and HMPE as suitable materials for preparing synthetic fiber ropes for mooring and examined their applications. However, with fiber chains, strength and durability similar to mooring ropes are required to transport heavy objects; however, their usage and required characteristics vary than those of mooring ropes. Therefore, to select a suitable material for crane ropes, in this study, we aim to analyze the characteristics of HMPE and liquid crystal polymer (LCP) materials in terms of quasi-static stiffness and durability under various load conditions.

2. Materials and Methods

2.1 Materials and Experimental Setup

In this study, three types of fiber materials were tested for fiber chain development. Considering the yarn types with strength, durability, and wear resistance that can satisfy the specifications of fiber chain development, HMPE DM20, HMPE SK78, and LCP T147 were selected as test materials. The materials used in this study were supplied by DSR Corp. and the types of fiber materials used in this study and their mechanical properties are presented in Table 1.

Table 1 Types of fiber sample and their mechanical properties

Type	Modulus (g/den)	Tenacity (g/den)	Elongation (% at break)
DM20 (HMPE)	1042	35	3.6
SK78 (HMPE)	1267	40	3.5
T147 (LCP)	600	25.9	3.8

A Shimadzu model AGS-X universal tensile testing machine was used to apply varying load conditions to the fiber chain yarns, and the experimental system used to measure the mechanical properties is shown in Fig. 1.

Fig. 1 Photograph of the physical property measurement

2.2 Quasi-static Stiffness Test

In field applications, fiber chains are subjected to repeated extension and retraction. During these extension-retraction loading cycles, the changes in the stiffness characteristics of the fiber chains are essential to ensure the durability of the fiber chains, and thus, analysis of the stiffness characteristics with respect to the type of yarn is necessary.

In typical applications, a lifting device such as fiber chains uses 50% or less of the mean breaking load (MBL). Therefore, it is necessary to set the cycle load conditions considering the general operating conditions of fiber chains; the conditions of quasi-static stiffness tests

Table 2 Load cycle steps and load change conditions

Cycle Step	Load cycle	Condition	Remark
1	Extension load	50% of YBL	
2	Retraction load	10% of YBL	
3	Repetition	10–30% of YBL	15 times
4	Extension load	45% of YBL	24 h
5	Retraction load	20% of YBL	
6	Retraction load	5% of YBL	24 h
7	Extension load	20% of YBL	

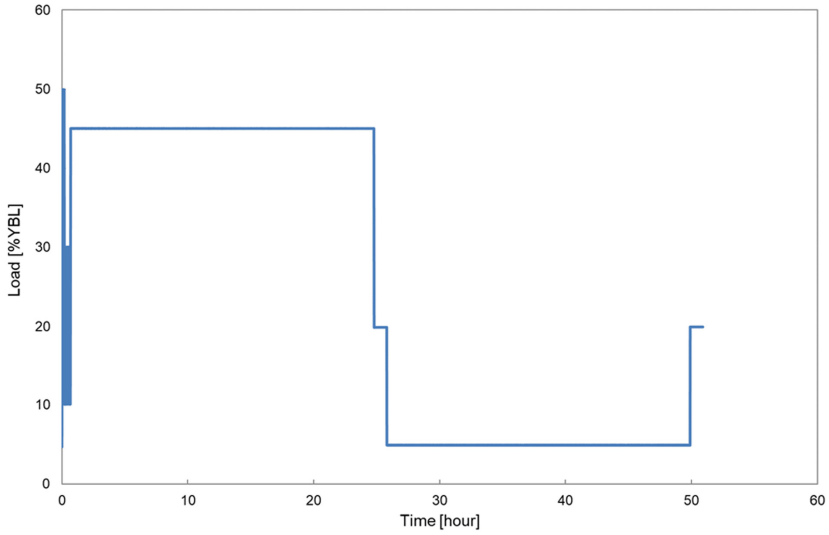

Fig. 2 Load change graph with time for quasi-static stiffness testing

reflecting the operating conditions are outlined in Table 2 and illustrated in Fig. 2.

The load cycles consist of cycle steps and load amplitudes, and in sequence of application, extension load was applied at 50% of MBL, retraction load at 10% of MBL; then, these cycles were repeated 15 times at 10–30% load range, and subsequently, extension load at 45% MBL, retraction load at 20% MBL, retraction load at 5% of MBL, and extension load at 20% MBL were applied (American Bureau of Shipping, 2020).

For evaluation of the yarn stiffness, quasi-static stiffnesses for windward and leeward conditions are measured in accordance with the test procedure. Windward stiffness is defined as the elongation (%) change (including creep) between 20% and 45% yarn breaking load (YBL) over 24 h, and leeward stiffness is defined as the change in elongation (%) (including creep recovery) between 20% and 5% YBL over 24 h. Yarn stiffness is calculated using Eq. (1):

$$Stiffness = \frac{\triangle F/YBL}{\triangle L/L_i} \quad (1)$$

where $\triangle F$ represents the change in YBL considered in high- and low-load creep recovery, $\triangle L$ is the extensional displacement that occurs according to $\triangle F$, and L_i represents the initial length at which the load cycle test starts.

2.3 3-T Endurance Test

When fiber chains are subjected to extension loads close to the design loads, the elongation (%) increases and the fiber chain is eventually ruptured. In this regard, it is important to present the appropriate allowable tension, that is, the design load that the fiber chain can endure before rupture when the extension load is applied. Therefore, analysis of design loads is required for different fiber materials at the yarn level before they are fabricated into fiber chains. 3-T (tension vs. stretch test) endurance tests measure the time taken to rupture under stretched conditions of average breaking load (ABL) for design load analysis of different types of yarn.

3-T endurance tests were conducted in accordance with DNV rules (Det Norske Veritas, 2018) by applying extension loads with respect to the standard with reference to the mean breaking load (MBL); the time

Table 3 3-T endurance test condition

Step	Load	Condition
1	1% ABL	17 min
2	1–50% ABL	10 cycles
3	70% ABL	
4	-	Allow specimen to cool
5	Load to designate tension	
6	-	Measure the time to rupture

taken until the yarn was ruptured was measured. Table 3 outlines the conditions of the 3-T endurance tests.

3. Results and Discussion

3.1 Quasi-static Stiffness According to Yarn Type

Quasi-static stiffness tests were conducted using different types of yarn. Quasi-static stiffness is represented by the change in the strain in response to a change in the load. Strain change varies according to the extension and retraction, and the slope of the curve depends on the type of yarn. YBL was calculated based on the mean values of three measurements of the breaking load measurements of each yarn, and the breaking tensile strength results are listed in Table 4. The average loading rate for static tensile strength test is 10% MBL/min (American Bureau of Shipping, 2020).

The measurement results for quasi-static stiffness of DM20 fiber (measured at 20℃ conditions) are illustrated in Fig. 3. Before measuring the strain change over 24 h, a load of 50% YBL, a retraction load of 10% YBL, and repeated loading of 10−30% YBL were applied. For DM20 fiber, when 45% of MBL was applied for 24 h, strain was increased by approximately 0.8%. Since the load was applied for 24 h, the characteristics of change in the creep behavior of the yarn are included in the analysis. In addition, when a retraction load of 5% MBL was applied for 24 h, strain recovery of 0.31% was obtained, and the characteristics of the change in the creep recovery behavior of the yarn were analyzed. Quasi-static windward stiffness is the slope of the load-strain curve, and it can be obtained when the load of the test conditions is applied; the windward stiffness of DM20 fiber was 18.1. Quasi-static leeward stiffness is the slope of the load-strain curve, and it is obtained when the retraction load of the test condition is applied; the leeward stiffness of DM20 fiber was 15.36. Dynamic stiffness is the slope of the load-strain curve, and it is obtained when the extension load-retraction load of the test condition is repeatedly applied; the dynamic stiffness of DM20 fiber was 51.82.

The results of measurements of quasi-static stiffness of SK78 fiber are shown in Fig. 4. From the test results of SK78, when 45% MBL was applied for 24 h, the strain increased by approximately 1.26%, and when a retraction load of 5% MBL was applied for 24 h, a strain recovery of 0.57% was obtained. The quasi-static windward stiffness under extension load conditions and the leeward stiffness under retraction load conditions for SK78 fiber were 11.11 and 8.77, respectively, and the dynamic stiffness under the cyclic application of extension-retraction load was 38.46.

The measurement results for quasi-static stiffness of T147 fiber (measured at room temperature conditions) are shown in Fig. 5. For T147, when 45% MBL was applied for 24 h, the strain increased by approximately 0.1%, and when a retraction load of 5% was applied for 24 h, strain recovery of 0.163% was obtained. The quasi-static windward stiffness under the extension load condition and the leeward stiffness under the retraction load condition for T147 fiber were 29 and 33.5, respectively, and the dynamic stiffness under the cyclic application of extension-retraction load was 24.87.

Table 4 Yarn breaking test results

Type	Mean breaking load (N)	Tensile strength (N/tex)
DM20	485.2	2.757
SK78	496.3	2.256
T147	386.6	2.315

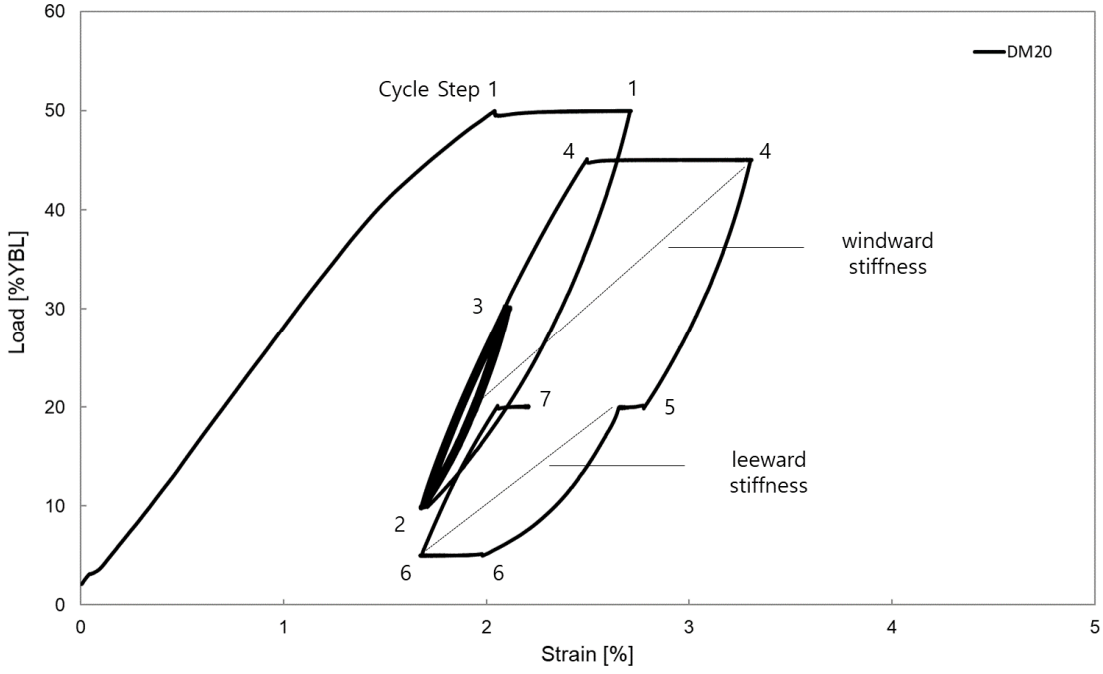

Fig. 3 Load-strain measured on DM20 fiber, based on yarn breaking load

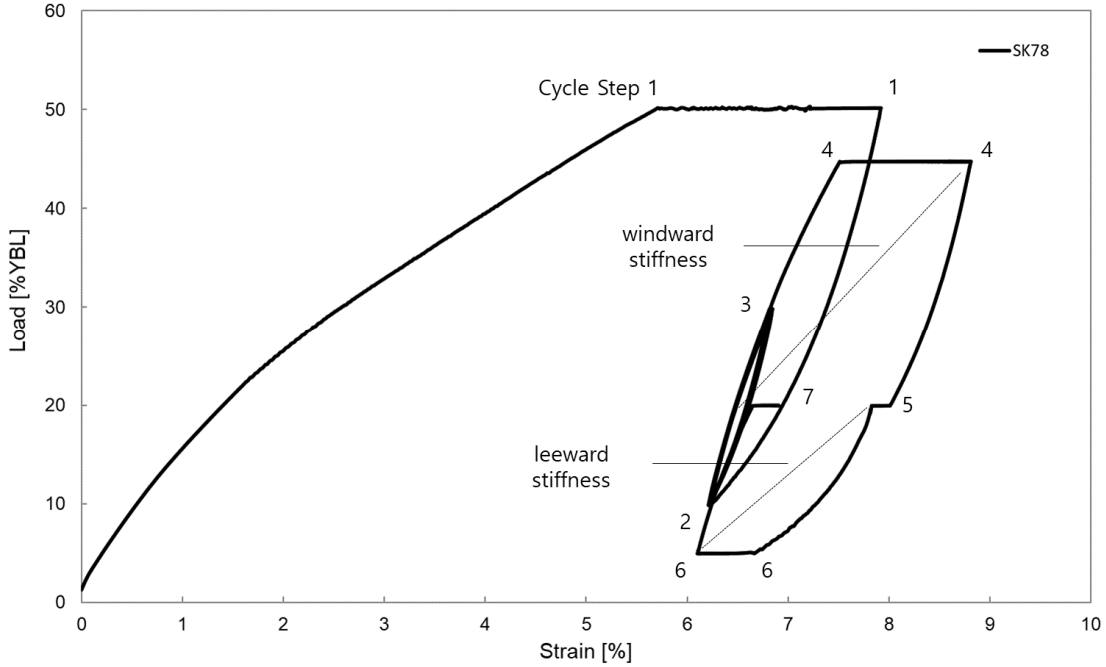

Fig. 4 Load-strain measured on SK78 fiber, based on yarn breaking load

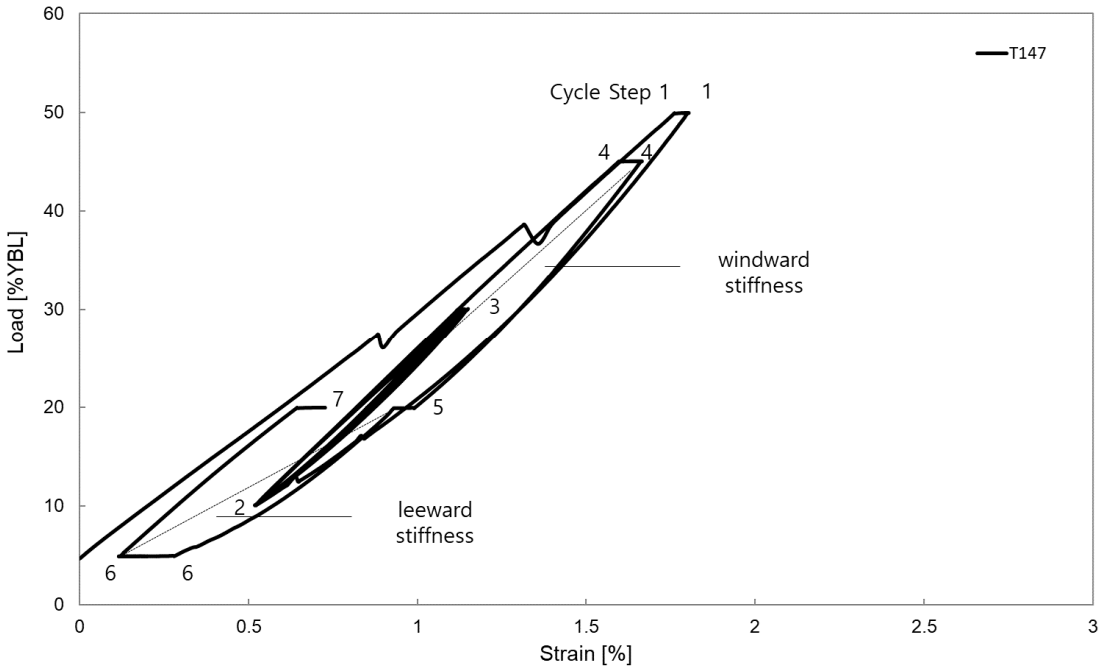

Fig. 5 Load-strain measured on T147 fiber, based on yarn breaking load

During field operations, fiber chains are subjected to high loads for prolonged durations. We applied 45% MBL for 24 h or a retraction load of 5% for 24 h to simulate the type of environment during field operations; there is a difference in the behavior of strain change due to the difference in the viscoelastic behavior of the fibers. When extension load was applied for 24 h, SK78 fiber showed the greatest strain increase among the three materials, showing a difference of approximately 12.6 times that of T147 fiber. The strain against the prolonged application of the extension load can be seen as representing the resistance characteristics of the fiber material under the conditions of continuous loading. The fiber ruptured when the maximum strain was exceeded; therefore, the fiber chain should exhibit less increase in the strain under continuous loading and excellent fatigue life.

Table 5 shows the increase in the strain with respect to the material under the conditions of continuous loading for 24 h. When retraction load was applied for 24 h, SK78 fiber, which showed a large increase in the strain against the extension load, exhibited the greatest strain recovery, and T147 fiber showed the smallest strain recovery. The strain against the prolonged application of the retraction load shows the characteristics of the recovery of the fiber material when the load is

Table 5 Strain increase and recovery test results for 24 hours

	DM20	SK78	T147
Strain increase at 45% YBL	0.8	1.26	0.1
Strain recovery at 5% YBL	0.31	0.57	0.163

Table 6 Equivalent stiffness and dynamic stiffness test results

Stiffness	DM20	SK78	T147
Windward stifness (24 h at 45% YBL)	18.1 × YBL	11.11 × YBL	29 × YBL
Leeward stifness (24 h at 5% YBL)	15.36 × YBL	8.77 × YBL	33.5 × YBL
Dynamic stiffness (10–30% YBL)	51.82 × YBL	38.46 × YBL	24.87 × YBL

removed from the fiber chain. When a fiber chain is subjected to repeated load cycles such as extension-retraction-stop, the increase in the strain is accumulated, eventually leading to the breaking of the fiber, and therefore, it is essential to examine the characteristics of the fiber in terms of extension-recovery under the conditions of prolonged loading.

The calculated windward and leeward stiffnesses are presented in Table 6. The calculated stiffness value corresponds to the slope in the load-strain graph, and the slope can be considered as the ratio of load change to strain change. A large slope indicates that the strain change was small even when the load change was large, and a small slope indicates that the strain change was large when the load change was large. Thus, T147 fiber showed the largest values of windward and leeward stiffnesses, and it is considered that T147 exhibited the smallest strain change under continuous load. For dynamic stiffness, DM20 fiber showed the highest value (51.82). Under the repeated application of extension load-retraction load, the stiffness of DM20 fiber is excellent, and it is considered that DM20 had the longest lifetime under the described operating conditions.

3.2 3-T Results of 3-T Endurance Test

The 3-T endurance test measures the duration for which a test specimen retains a specific tension level, although the tension level is lower than the minimum breaking tensile strength. Since the time measured in this test can be set as a design curve for durability, the results and analysis of 3-T endurance test are essential.

3-T tests were conducted for each of the three types of yarn; the mean of log(time-to-rupture (TTR)) with respect to the tension level is presented in Table 7. At the minimum load level, DM20 fiber showed the highest mean TTR, and at the maximum tension level, T147 fiber had the highest mean TTR. The standard deviation of TTR by yarn type was 0.134 for DM20 and 0.208 and 0.102 for SK78 and T147,

Table 7 Means of log(s) time for tension level

Type	Tension (N/tex)	Mean
DM20	2.671	3.74
	2.757	2.78
	2.842	1.55
SK78	2.185	3.50
	2.256	2.71
	2.326	1.01
T147	2.242	3.62
	2.315	3.30
	2.387	2.91

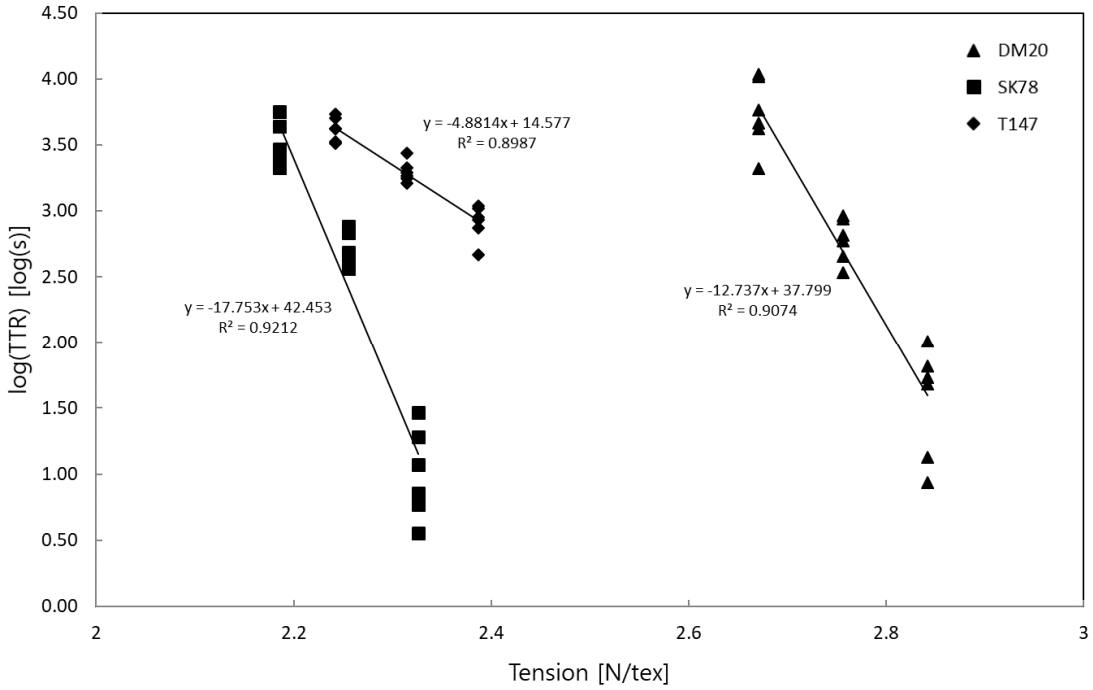

Fig. 6 Time to rupture test results with linear trend line added

respectively, and the deviation of TTR showed an increasing trend with increase in the tension level.

Fig. 6 shows the results of the slope of the linear curve obtained in the test. As the tension decreased, TTR increased exponentially; therefore, TTR was expressed on a log scale. It was measured at three different tension levels for each type of yarn, and a linear trend line was obtained for the measurement results. A linear regression model was applied to easily predict the relationship of TTR to the tension level within the design range, and a linear trend line was derived using the least squares method. The linear trend line indicates the slope characteristic of TTR with respect to tension. The slopes of DM20, SK78, and T147 fibers were −12.73,−17.75, and −4.88, respectively. Using the linear trend line values obtained from the test, the 3-T design characteristic curve that represents the design load characteristics with respect to time can be obtained. DM20 fiber exhibited a higher strength for the same lifetime, but examining the slope of the linear trend line, SK78 fiber showed the least decrease in the strength with respect to the increase in TTR.

In addition, the slope of the linear trend line indicates the tension with respect to the TTR, and TTR varies depending on the type of yarn material and the design load, which can provide insights for selecting the design strength of the yarn when fabricating the fiber chain. When the design strength of the yarn was decreased, the fatigue life increased with respect to the slope of the 3-T design characteristic curve, and therefore, the increase in the fatigue life can be predicted according to the slope calculated based on the test results.

4. Conclusion

In this study, to substitute the material used in steel chains with a synthetic fiber, the quasi-static stiffness characteristics of HMPE DM20, HMPE SK78, and LCP T147 fiber were analyzed, and 3-T endurance tests were performed. The results of this study are outlined as follows.

In the quasi-static stiffness test, the change in the strain of the fiber material against the application of the load is represented in terms of the value of the elastic properties of the fiber material under the conditions of prolonged application of extension load, retraction load, or continuous cyclic loads. With the fiber material, when non-cyclic loading was applied, such as extension-retraction loading, the increase in the strain accumulated, and when the maximum strain was exceeded, the fiber ruptured physically. Therefore, to obtain fiber chains with the desired characteristics, small increases in the strain are required under repeated extension-retraction loading and prolonged extension loading, and a large increase in the strain is required under the application of retraction loading. That is, when the quasi-static stiffness is large, the strain change with respect to the load is small; this characteristic is advantageous in terms of the durability of the fiber chain. In addition, the values of quasi-static windward, leeward, and dynamic stiffnesses of DM20, SK78, and T147 were calculated. T147 fiber showed the highest values for quasi-static windward and leeward stiffnesses, and DM20 fiber was excellent for dynamic stiffness.

For the three types of fiber materials, a 3-T design characteristic curve representing the tension-TTR relationship was derived. The decrease in the tension level and TTR varied depending on the type of the yarn material, and this characteristic can be applied as an important factor in selecting the design strength of the yarn when designing the fiber chain.

The 3-T design characteristic curve can be expressed as the ratio of tension to TTR, and the slope of the test result has important implications. DM20 showed high strength for the same lifetime, but from the slope of the 3-T design characteristic curve, SK78 fiber was calculated to show the lowest decrease in strength with respect to the increase in TTR. The increase in TTR with the decrease in the strength of the yarn can be predicted according to the slope calculated from the test results, which is an important factor in selecting the design strength of the yarn when fabricating the fiber chain.

It is expected that the results of the analysis of the quasi-static stiffness and 3-T design characteristic curve of different types of yarn can be utilized as important data for strength and durability characteristics in fiber chain design.

Conflict of Interest

No potential conflict of interest relevant to this article was reported.

Funding

This research was supported by the Ministry of Trade, Industry & Energy (MOTIE) of Korea (S2641260).

References

Banfield, S., & Casey, N. (1998). Evaluation of Fiber Rope Properties for Offshore Mooring. Ocean Engineering, 25(10), 861−79. https://doi.org/10.1016/S0029-8018(97)10017-8

Del Vecchio, C.J.M. (1992). Light Weight Materials for Deep Water Moorings (Ph.D. Thesis). University of Reading, UK.

Petruska, D.J., Kelly, P., Stone, B., Ahjem, V., Zimmerman, E.H., Garrity, R., & Veselis,Y. (2010). Fiber Moorings, Recent Experiences and Research: Updating API RP 2SM on Synthetic Fiber Rope for Offshore Moorings. Offshore Technology Conference, Houston, USA. https://doi.org/10.4043/20836-MS

Davies, P., Francois, M., Grosjean, F., Baron, P., Salomon, K., & Trassoudaine, D. (2002) Synthetic Mooring Lines for Depths to 3000 Meters. Offshore Technology Conference, Houston, USA. https://doi.org/10.4043/14246-MS

Chi, C.H., Lundhild, E.M., Veselis, T., & Huntley, M. (2009) Enabling Ultra-Depwater Mooring with Aramid Fiber Rope Technology. Offshore Technology Conference, Houston, USA. https://doi.org/10.4043/20074-MS

Det Norske Veritas. (2018) Offshore Fibre Ropes (Offshore Standard DNV-OS-E303).

Fernandes, A.C., Del Vecchio, C.J.M., Castro, G.A.V. (1999). Mechanical Properties of Polyester Mooring Cables. International Journal of Offshore and Polar Engineering, 9(3), 208−213.

Peter, D., Yvan, R., Loic, D., & Patrice, W. (2011). Mechanical Behaviour of HMPE and Aramid Fibre Ropes for Deep Sea Handling Operations. Ocean Engineering, 38(17−18), 22208−2214. https://doi.org/10.1016/j.oceaneng.2011.10.010

Davies, P., Francois, M., Lacotte, N., Vu, T.D., & Durville, D. (2015) An Empirical Model to Predict the Lifetime of Braided HMPE Handling Ropes Under Cyclic Bend Over Sheave (CBOS) Loading. Ocean Engineering, 97, 74−81. https://doi.org/10.1016/j.oceaneng.2015.01.003

Garrity, R., & Fronzaglia, W. (2008) The Use of HMPE Mooring Lines in Deepwater MODU Mooring Systems. In OCEANS 2008, IEEE, 1-4. https://doi.org/10.1109/OCEANS.2008.5151912.

Leite, S., & Boesten, J. (2011) HMPE Mooring Lines for Deepwater MODUs. Offshore Technology Conference, Brazil. https://doi.org/10.4043/22486-MS

Bunsell, A.R. (2009). Handbook of Tensile Properties of Textile and Technical Fibres, Woodhead Publishing.

Tahar, A., & Kim, M.H. (2008). Coupled-Dynamic Analysis of Floating Structures with Polyester Mooring Lines. Ocean Engineering, 35(17−18), 1676-1685. https://doi.org/10.1016/j.oceaneng.2008.09.004

Weller, S.D., Davies, P., Vickers, A.W., & Johanning, L. (2014) Synthetic Rope Responses in the Context of Load History: Operational Performance. Ocean Engineering. 83, 111−124. https://doi.org/10.1016/j.oceaneng.2014.03.010

Berryman, C.T., Dupin, R.M., & Gerrits, N.S. (2002) Laboratory Study of Used HMPE MODU Mooring Lines. Offshore Technology Conference, Houston, USA. https://doi.org/10.4043/14245-MS

Williams, J.G., Miyase, A., Li, D.H., & Wang, S.S. (2002) Small-Scale Testing of Damaged Synthetic Fiber Mooring Ropes. Offshore Technology Conference, Houston, USA. https://doi.org/10.4043/14308-MS

Ward, E.G., Ayres, R.R., Banfield, S.J., O'Hear, N., & Laurendine, T. (2006) The Residual Strength of Damaged Polyester Ropes. Offshore Technology Conference, Houston, USA. https://doi.org/10.4043/18150-MS

Da Costa Mattos, H.S., & Chimisso, F.E.G. (2011) Modelling Creep Tests in HMPE Fibres Used in Ultra-Deep-Sea Mooring Ropes. International Journal Of Solids And Structures. 48(1), 144−152. https://doi.org/10.1016/j.ijsolstr.2010.09.015

Cédric, B., Peter, D., Guilhem, B., Yann, M., & Julien, B. (2020) Influence of Bedding-in on the Tensile Performance of HMPE Fiber Ropes. Ocean Engineering, 203, 107144. https://doi.org/10.1016/j.oceaneng.2020.107144

Gen, L., Wenhua, L., Shanyin, L., Hangyu, L., Yangyuan, G., & Yuqing, S. (2021) Dynamic Stiffness of Braided HMPE Ropes Under Long-Term Cyclic Loads: A Full-Scale Experimental Investigation. Ocean Engineering. 230, 109076. https://doi.org/10.1016/j.oceaneng.2021.109076

American Bureau of Shipping. (2020) Guidance Notes on The Application of Fiber for Offshore Mooring.

Author ORCIDs

Author name	ORCID
Kim, Kyeongsoo	0000-0003-3429-8063
Kim, Taewan	0000-0001-7464-3752
Kim, Namhun	0000-0003-1884-938X
Kim, Dokyoun	0000-0002-8946-9483
Kang, Yongjun	0000-0001-8964-7916
Kim, Seonjin	0000-0001-7755-2581

KSOE

Journal of Ocean Engineering and Technology 35(6), 434-445, December, 2021
https://doi.org/10.26748/KSOE.2021.069

pISSN 1225-0767
eISSN 2287-6715

Original Research Article

UUV Platform Optimal Design for Overcoming Strong Current

Min-Gyu Kim[1], Hyungjoo Kang[2], Mun-Jik Lee[2], Gun Rae Cho[3], Ji-Hong Li[4] and Cheol Kim[5]

[1]*Researcher, Intelligent Robotics R&D Division, Korea Institute of Robotics & Technology Convergence, Pohang, Korea*
[2]*Senior Researcher, Intelligent Robotics R&D Division, Korea Institute of Robotics & Technology Convergence, Pohang, Korea*
[3]*Principal Researcher, Intelligent Robotics R&D Division, Korea Institute of Robotics & Technology Convergence, Pohang, Korea*
[4]*Chief Researcher, Intelligent Robotics R&D Division, Korea Institute of Robotics & Technology Convergence, Pohang, Korea*
[5]*Professor, Department of Mechanical Engineering, Kyungpook National University, Daegu, Korea*

KEY WORDS: Unmanned underwater vehicle (UUV), Remotely operated vehicle (ROV), Autonomous unmanned vehicle (AUV), Overcome strong current, Thrust vector control (TVC)

ABSTRACT: *This paper proposes an optimal design method for an unmanned underwater vehicle (UUV) platform to overcome strong current. First, to minimize the hydrodynamic drag components in water, the vehicle is designed to have a streamlined disc shape, which help maintaining horizontal motion (zero roll and pitch angles posture) while overcoming external current. To this end, four vertical thrusters are symmetrically mounted outside of the platform to stabilize the vehicle's horizontal motion. In the horizontal plane, four horizontal thrusters are symmetrically mounted outside of the disc, and each of them has the same forward and reverse thrust performances. With these four thrusters, a specific thrust vector control (TVC) method is proposed, and for external current in any direction, four horizontal thrusters are controlled to generate a vectored thrust force to encounter the current while minimizing the vehicle's rotation and maintaining its heading. However, for the numerical simulations, the vehicle's hydrodynamic coefficients related to the horizontal plane are derived based on both theoretical and empirically derived formulas. In addition to the simulation, experimental studies in both the water tank and circulating water channel are performed to verify the vehicle's various final performances, including its ability to overcome strong current.*

1. Introduction

Recently, there has been increasing interest in unmanned underwater vehicles (UUVs) that can be used in marine accidents and extreme environments. This is because of the challenges involving the reliance on divers, including the risk of secondary accidents and short exploration times. However, UUVs can perform explorations for long periods of time without secondary accidents, such as human causalities. However, to enable the frequent use of UUVs, it is necessary to overcome the challenges associated with strong currents.

Existing UUVs can be broadly divided into two categories: remotely operated vehicles (ROVs) and autonomous unmanned vehicles (AUVs). Most ROVs have a box-shaped exterior, as shown in Fig. 1(a), which enables the exploration of specific areas in detail as well as the performance of underwater tasks using manipulators. Such forms are excellent in terms of control stability, but they have the disadvantage of being vulnerable to current owing to their high drag coefficient underwater. AUVs are mostly used for the rapid exploration of large areas. Therefore, they have the structural characteristic of a torpedo-shaped exterior, as shown in Fig. 1(b), and their three-dimensional (3D) movement in water is controlled using thrusters and rudders attached at the rear. Owing to the structural properties of such propulsion systems, they are quickly able to provide speed and stability in the forward direction, but their maneuverability is markedly poor, and they have difficulty operating normally in environments with irregular currents.

Early research was performed by the Korea Research Institute of Ships & Ocean Engineering on multi-legged biomimetic submarine robots called CR200 and CR6000 (Jun et al., 2013; Yoo et al., 2014). These research efforts involved the use of a new concept to overcome currents by landing on the sea floor and walking in current environments, which was based on structures that use six legs to perform swimming rather than the conventional propellor method. However, it was found that there remained a challenge of moving on the sea floor in environments with currents of 1.03 m/s or more owing to the large external structure of the robot itself. Pyo and Yu (2016)

Received 3 September 2021, revised 5 November 2021, accepted 11 November 2021
Corresponding author Min-Gyu Kim: +82-54-279-0475, zxdwa0817@kiro.re.kr

(a) ROV platforms developed globally

(b) Various AUV platforms developed by the US Navy

Fig. 1 Examples of conventional UUV platforms

performed a study on a two-body AUV called MI (Mission: Impossible). In strong current environments, the AUV attaches to the sea floor, where the bottom part acts as an anchor and the top part uses a detachable structure to explore the current environment. For detailed explorations, there is still a difficulty with respect to having the top part overcome the current and approach the target object, but it is still considered to be an effective attempt. Unfortunately, only a conceptual design was produced, and there has been no further design, manufacturing, or research.

This paper discusses research on effective methods that are employed to overcome strong current through an optimized design of a UUV's streamlined external structure and propulsion system. Technical research on these research items was performed with the support of the Ministry of Maritime Affairs and Fisheries' Future Marine Industrial Technology Development Program, Korea (Li et al., 2019a).

The UUV platform that was developed in the second year of this study is shown in Fig. 2(a). It was confirmed to have a maximum forward speed of 2.16 m/s underwater, and it can move forward even in a circulating water channel of 1.29 m/s (Li et al., 2019a). However, the three vertical propellers are attached close to the platform's center

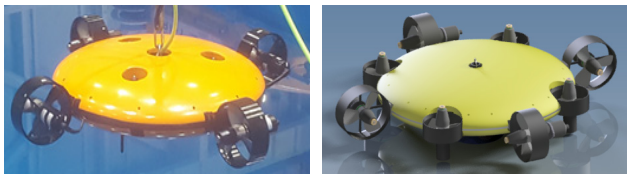

(a) Prototype-II (b) Prototype-III

Fig. 2 Developed UUV platforms

point, and it was difficult to ensure control stability on the platform's horizontal plane in strong current environments. This problem makes it difficult to operate in an environment with irregular currents, which is the main purpose of the platform. To overcome this problem in the UUV Prototype-III, the capacity of the vertical propellers was expanded, and the number of propellers was increased from three to four, and they were installed on the outer parts of the platform, as shown in Fig. 2(b). Because of these structural features, the platform's drag coefficient underwater increased, and the maximum forward speed reached 1.85 m/s; however, experiments in a circulating water channel confirmed that it was possible for the platform to move while maintaining its depth and attitude in an environment with a maximum current of 0.77 m/s because stability in the horizontal plane was assured.. This paper mainly discusses research on Prototype-III of the UUV for overcoming strong current, which was researched and developed in the third year of this study.

2. System Overview

2.1 General Specifications

As shown in Fig. 2(b), the robot platform has a structure in which the pressure vessel, buoyant material, and propellors are attached to a single circular frame. The sensors for the navigation system include an acoustic Doppler current profiler (ADCP) in the lower part of the platform and an attitude heading reference system (AHRS) inside the pressure vessel. The propulsion system for swimming includes four vertical thrusters and four horizontal thrusters arranged symmetrically on the circular frame. A streamlined shape was chosen for the platform's exterior to ensure forward speed through low drag, and it was designed as a circular shape in order to increase the platform's capacity to respond to changing current. The integrated platform's general specifications are shown in Table 1.

Table 1 General specifications of Prototype-III

Items	Specification
Depth rating	100 m
Dimension	1250 m (L) × 240 m (H)
Weight	61.5 kg
Thrust system	Horizontal: 4 × 1 kW (Max. Thrust, 254 N) Vertical: 4 × 0.5 kW (Max. Thrust, 129 N)
Motion sensors	ADCP, AHRS, Depth sensor

2.2 Mechanical System

The platform was designed for a working depth of 100 m. Considering the platform's specific gravity and corrosion resistance, the frame and pressure vessel were designed with AL6061-T6; further, the design was optimized by performing thickness calculations (Moon et al., 2009) and structural analysis based on target values that consider the usage environment. Urethane foam was used as the buoyant material, and its mechanical stiffness was improved by coating the exterior thinly with glass fiber reinforced plastic (GFRP).

2.3 Surface Control Unit

The robot's operating system consists of a shipboard control system (Fig. 3) and a cable winch system (Fig. 4). The shipboard control system consists of a 330 VDC power supply unit, which is required for the thrusters, and a remote control system that is installed on a mobile console. All of the algorithms required for control of the robot are run from the remote control system, and the calculated control commands are sent to the platform in real time via the tether cable's optical communications channel. Monitoring, control, and management of the platform are performed using the graphical user interface (GUI) screen of the shipboard control system.

(a) Control console

(b) Power supply console

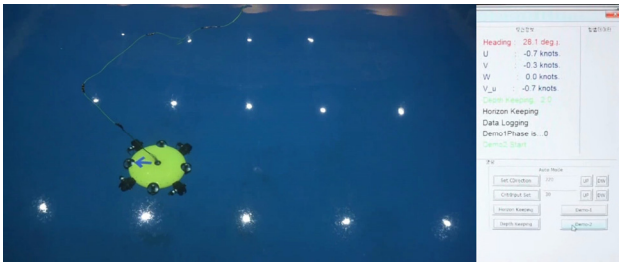

(c) GUI display

Fig. 3 Surface control unit

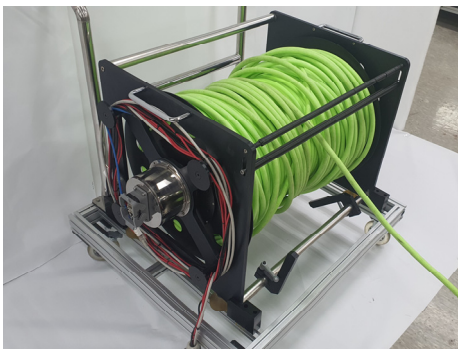

Fig. 4 Tether cable winch system

The tether cable consists of an eight-line power wire and four communications channels. In addition to the slip rings, the wench system includes a communications converter for converting from optical communications to ethernet communications, as well as a video signal converter for converting from optical communications to video signals.

3. Vehicle Design and Its Hydrodynamic Modeling

3.1 Devices Arrangement and Mechanical Design

In the design of a platform for overcoming strong current, the aspect that is considered first is the minimization of the drag experienced by the robot underwater. To achieve this, it is necessary to consider the overall form and optimize the arrangement of equipment such as the thrusters and the ADCPs. Then, a miniaturized light-weight design should be developed for the frame and pressure vessel in the robot design stage.

First, in order to minimize the drag on the exterior, the Mring equation was used to calculate the basic exterior dimensions. After the initial values were calculated with this formula, essential equipment such as the thrusters and pressure vessel were arranged, and optimization was performed with a design-analysis-redesign approach. Considering the reduction in the platform's overall size, the increase in usability, and the convenience of making modifications, the thrusters were externalized. To minimize its impact, an optimal design was created by performing the structural analysis of the ducts and the duct-frame connectors, and the additional drag was minimized through fluid analysis.

To resolve the problem of the unstable attitude control on the horizontal plane that occurred in Prototype-II, the number of vertical thrusters was increased from three to four, and their distance from the centrifuge was increased. Taking this into account, the three separate pressure vessels in Prototype-II were integrated into a single pressure vessel and located at the center of the platform in Prototype-III (Fig. 5).

Generally, when ultrasonic sensors such as Doppler velocity logs (DVLs) and ADCPs are used in UUVs, they are located on the bottom-most part of the platform to minimize the effect of sonic interference. Further, it is advantageous to locate them at the center bottom of the ADCP in order to improve static stability through a low

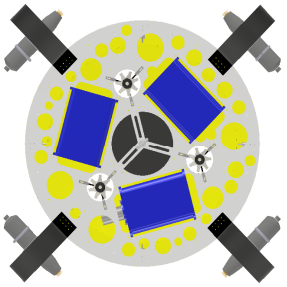

(a) Prototype-II

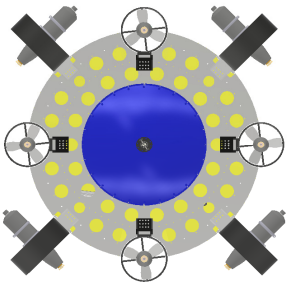

(b) Prototype-III.

Fig. 5 Pressure hull arrangements

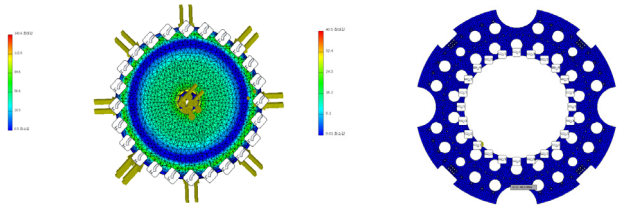

(a) Pressure hull (b) Frame

Fig. 6 Structural analysis

Table 2 Structural analysis result

Cases	Expected maximum stress	Safety factor
Frame	40.5 MPa	5.8
Pressure hull	140.6 MPa	1.67

※ Expected yield strength of AL6061-T6 is 235 MPa

center of gravity. However, in this case, owing to the properties of the disc-shaped platform, they overlap with the location of the pressure vessel and unavoidably increase the height of the platform, which can lead to an increase in the platform's fluid resistance.

This problem was resolved by inserting the ADCP inside the pressure vessel, locating the ADCP sensor on the bottom of the pressure vessel, and placing the ADCP electronics in the center of the pressure vessel interior.

The thickness of the pressure vessel was calculated based on a thickness formula (Moon et al., 2009). However, to ensure reliability, additional verification was performed on the top cover by performing a structural analysis because the top cover is a part that directly receives a load. As shown in Fig. 6(a), the structural analysis results confirm that the top has a safety factor of around 1.67 compared to the yield strength of the material, as listed in Table 2. This is a higher figure than the factor of 1.2 to 1.5 that is generally stipulated in ship classification regulations, indicating that it has excellent stability. The pressure vessel that was manufactured according to this design was pressure-tested at the Korea Research Institute of Ships & Ocean Engineering by applying a pressure of 1 MPa for 30 min in a pressure chamber. As a result, it received accreditation from the Korea Laboratory Accreditation Scheme (KOLAS), confirming that there was no deformation or leakage.

The four vertical thrusters were arranged symmetrically in relation to the designed pressure vessel. To reduce the drag that occurs owing to the vertical thrusters, the neutral duct exterior was miniaturized in keeping with 100-m specifications, and the thrusters were located at the ends of the platform interior, considering interference with the pressure vessel. By doing so, control stability on the horizontal plane was increased.

For the horizontal thrusters, this study selected a model in which the forward thrust matches the reverse thrust, and the thrusters were arranged symmetrically on the circular frame. This ensures that if the maximum thrust of one thruster is $F_{\max}$, the maximum thrust on the horizontal plane is $2\sqrt{2}F_{\max}$, and the minimum thrust is $2F_{\max}$. This was done with consideration to overcoming changes in the direction of the current by keeping a fixed thrust in all directions. The thruster vector control (TVC) algorithm that uses the four horizontal thrusters is discussed in detail in section 4.

In addition, the buoyant material was placed on the top of the frame, and the exterior systems and pressure sensors were attached to the bottom. This was done to improve the platform's attitude recovery capacity by increasing the relative height of the center of buoyancy and the center of gravity.

In order to confirm the structural stability of the frame at the points at which equipment such as the pressure vessel and thrusters was attached, a similar structural analysis was performed. The analysis targeted the launch and recovery environment, which applies the greatest dynamic load among the various environments in which the UUV is used. The boundary conditions for the frame parts that are connected to the lifting eye during the analysis were set, and the analysis was performed. As shown in Table 2, the results confirmed that the design has a safety factor of 5.8, which is somewhat higher than the safety factor of four, and takes into account the dynamic load generally caused by waves or wind during launch and recovery.

3.2 Vehicle Modeling

As mentioned previously, this study designed the system using four vertical thrusters to maintain stability in the platform's horizontal plane, i.e., to keep the platform's roll and pitch angles at 0 degrees at all times. In other words, the four vertical thrusters were designed as dedicated controllers in order to maintain the robot's horizontal plane. Based on this premise, this study estimated the hydrodynamic coefficients of the robot platform by limiting them to the horizontal plane, and they were then used in the simulations.

3.2.1 Vehicle's horizontal kinematics and dynamics

In general, the kinematics and dynamics of a UUV can be expressed as follows (Fossen, 2002; Li et al., 2019b).

$$\begin{aligned} \dot{\eta} &= C_b^n \nu, \\ M_{RB}\dot{\nu} + C_{RB}\nu &= \sum F_{ext} \end{aligned} \tag{1}$$

Here, $\eta = [x, y, \psi]^T$ is the vector of the robot's horizontal plane position and attitude in the navigation coordinate system, $\nu = [u, v, r]^T$ is the vector of linear and rotational speed in the horizontal plane in the robot body coordinate system, and C_b^n is the coordinate transformation matrix from the robot body coordinate system to the navigation coordinate system, and is defined below.

$$C_b^n = \begin{bmatrix} \cos\psi & -\sin\psi & 0 \\ \sin\psi & \cos\psi & 0 \\ 0 & 0 & 1 \end{bmatrix} \tag{2}$$

In this study, the robot platform has a top/bottom, left/right symmetrical structure. Adjustments were made to place the platform's

Table 3 Platform mass and moment of force

Parameters	Value	Unit
m	+6.15e+001	kg
I_{ZZ}	+8.04e+000	kg·m^2

center of gravity at $(x_0, y_0) = (0,0)$ by performing repeated ballast operations on the assembled platform underwater. Based on the results, the platform's rigid body inertial matrix M_{RB} and Coriolis and centrifugal force matrix C_{RB} in Eq. (1) can be expressed as below.

$$M_{RB} = \begin{bmatrix} m & 0 & 0 \\ 0 & m & 0 \\ 0 & 0 & I_{ZZ} \end{bmatrix}, \qquad C_{RB} = \begin{bmatrix} 0 & 0 & -mv \\ 0 & 0 & mu \\ 0 & 0 & 0 \end{bmatrix} \tag{3}$$

Here, m is the rigid body mass, and I_{ZZ} is the rotation moment about the center axis on the horizontal plane, as shown in Table 3.

Fig. A1 and Table A1 in the appendix show the dimensions of the UUV frame used to calculate I_{ZZ} which is the rotational moment in the horizontal plane.

Hence, $\sum F_{ext}$ in Eq. (1) can be expressed as follows.

$$\sum F_{ext} = F_{drag} + F_{added\ mass} + F_{control} \tag{4}$$

Here, F_{drag} is the hydrodynamic damping; $F_{added\ mass}$ is the added mass; and $F_{control}$ is the control input.

3.2.2 Hydrodynamic damping F_{drag}

The robot platform discussed in this study has a structure that is symmetrical in the X, Y, and Z axes in three-dimensions. Therefore, the moment component caused by linear motion and the force component caused by rotational motion are both ignored in this study. In addition, the UUV platform model was simplified, as was done in Prestero (2001), and the following two additional assumptions were made to avoid overly complicated mathematical calculations.

- The acceleration coupling component is ignored.
- Higher-dimensional hydrodynamic damping components above two dimensions are ignored.

As a result, the F_{drag} component can be simplified as follows.

$$F_{drag} = [X_{u|u|}u|u|,\ \ Y_{v|v|}v|v|,\ \ N_{r|r|}r|r|]^T \tag{5}$$

The corresponding hydrodynamic coefficients were calculated using the following empirical formulas (Newman, 1977; Prestero, 2001).

$$\begin{aligned} X_{uvertuvert} &= Y_{vvertvvert} \\ &= -\frac{1}{2}\rho c_d \pi ab - 4 \times \frac{1}{2}\rho s'_{HT} c_{dHT} - 4 \times \rho s_{VT} c_{dVT} \end{aligned} \tag{6}$$

$$N_{rvertrvert} = -2 \times \frac{1}{2}\rho c_d \int_0^a D(r) r^{3dr} - 4 \times x_{HT}^3 \times \frac{1}{2}\rho s_{VT} c_{dVT} \tag{7}$$

Here, ρ is the liquid density, and c_d, c_{dHT}, and c_{dVT} are drag coefficients that correspond to the platform's ellipsoid, horizontal thrusters, and vertical thrusters. and are the major axis and minor axis in the ellipsoid's horizontal plane. s_{HT}, s_{VT}, and s'_{HT} are the cross section areas that correspond to each thruster (Figs. A1–A3). Table A2 in the appendix shows the cross sections for each thruster.

The calculated damping coefficients are shown in Table 4.

Table 4 Hydrodynamic damping coefficients

Parameters	Value	Unit
$X_{u\|u\|}$	-1.06e+002	kg/m
$Y_{v\|v\|}$	-1.06e+002	kg/m
$N_{r\|r\|}$	-4.99e+000	kg·m^2/rad^2

3.2.3. Added mass $F_{added\ mass}$

To calculate the additional mass coefficient, this study only considered the diagonal components in the additional mass matrix via the platform's symmetrical structure. The corresponding coefficients were estimated as follows using an empirical graph presented in the literature (Newman, 1977).

The added mass coefficients are shown in Table 5.

Table 5 Added mass coefficients

Parameters	Value	Unit
$X_{\dot{u}}$	-8.2e+000	kg
$Y_{\dot{v}}$	-8.2e+000	kg
$N_{\dot{r}}$	-2.7e+002	kg·m^2/rad

In addition, the added mass $F_{added\ mass}$ is as follows

$$F_{added\ mass} = [X_{\dot{u}}\dot{u},\ \ Y_{\dot{v}}\dot{v},\ \ N_{\dot{r}}\dot{r}]^T \tag{8}$$

Based on the results, the model of motion and dynamics on the robot's horizontal plane can be set up as follows.

$$\begin{bmatrix} \dot{x} \\ \dot{y} \\ \dot{\psi} \end{bmatrix} = \begin{bmatrix} \cos\psi & -\sin\psi & 0 \\ \sin\psi & \cos\psi & 0 \\ 0 & 0 & 1 \end{bmatrix} \begin{bmatrix} u \\ v \\ r \end{bmatrix} \tag{9}$$

$$\begin{aligned} \begin{bmatrix} \dot{u} \\ \dot{v} \\ \dot{r} \end{bmatrix} &= \begin{bmatrix} \dfrac{mvr}{m - X_{\dot{u}}} + \dfrac{X_{u|u|}}{m - X_{\dot{u}}} u|u| \\ -\dfrac{mur}{m - Y_{\dot{v}}} + \dfrac{Y_{v|v|}}{m - Y_{\dot{v}}} v|v| \\ \dfrac{N_{r|r|} r|r|}{I_{zz} - N_{\dot{r}}} \end{bmatrix} + \begin{bmatrix} \dfrac{1}{m - X_{\dot{u}}} & 0 & 0 \\ 0 & \dfrac{1}{m - Y_{\dot{v}}} & 0 \\ 0 & 0 & \dfrac{1}{I_{zz} - N_{\dot{r}}} \end{bmatrix} \begin{bmatrix} F_u \\ F_v \\ F_r \end{bmatrix} \\ &= \begin{bmatrix} f_u \\ f_v \\ f_r \end{bmatrix} + \begin{bmatrix} b_u & 0 & 0 \\ 0 & b_v & 0 \\ 0 & 0 & b_r \end{bmatrix} \begin{bmatrix} F_u \\ F_v \\ F_r \end{bmatrix} \end{aligned} \tag{10}$$

Here, $F_{control} = [F_u, F_v, F_r]^T$ are the control inputs.

4. TVC Algorithm

When the robot performs a given task underwater, the ADCP attached to the bottom of the robot platform can measure the flow speed U_{cur} and direction ψ_{cur} of the current in real time as it flows in any direction. The main objective of the control algorithm in this study is to use the four horizontal thrusters to overcome this current while maintaining the robot's given horizontal plane motion $(x_{ref}(t),\ y_{ref}(t),\ \psi_{ref}(t))$ (Fig. 7).

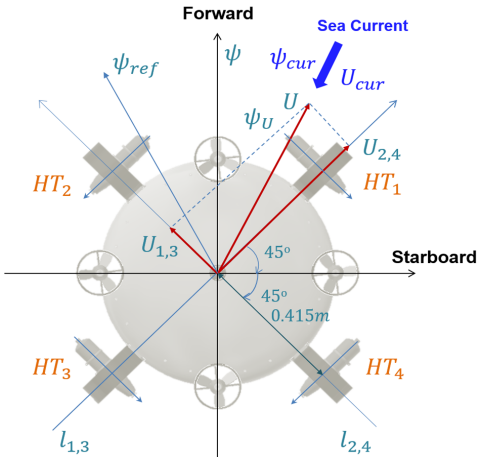

Fig. 7 Horizontal thruster arrangement in the body-fixed frame

4.1 Model-based Controller Design

Assuming that the robot's model, i.e., the hydrodynamic coefficients, is accurately known, it is possible to design the controller using a general backstepping technique (Krstic et al., 1995; Li, 2016), as shown below.

Step 1. As mentioned before, the control objective here is to maintain the given motion $(x_{ref}(t),\ y_{ref}(t),\ \psi_{ref}(t))$. In addition, in this stage, the following Lyapunov function candidate is considered.

$$V_1 = \frac{1}{2}\left(x_e^2 + y_e^2 + \gamma_\psi \psi_e^2\right) \tag{11}$$

Here, $x_e = x_{ref} - x,\ y_e = y_{ref} - y$, 및 $\psi_e = \psi_{ref} - \psi$; $\gamma_\psi > 0$ is a design variable.

If both sides of Eq. (11) are differentiated and inserted in Eq. (9),

$$\dot{V}_1 = x_e(\dot{x}_{ref} - U_x) + y_e(\dot{y}_{ref} - U_y) + \gamma_\psi \psi_e(\dot{\psi}_{ref} - r) \tag{12}$$

Here, U_x and U_y are defined as follows.

$$\begin{bmatrix} U_x \\ U_y \end{bmatrix} = \begin{bmatrix} \cos\psi & -\sin\psi \\ \sin\psi & \cos\psi \end{bmatrix} \begin{bmatrix} u \\ v \end{bmatrix} = P_b^n \begin{bmatrix} u \\ v \end{bmatrix} \tag{13}$$

If (U_x, U_y, r) in Eq. (12) are seen as virtual control inputs, and $(\alpha_{Ux}, \alpha_{Uy}, \alpha_r)$ is the corresponding stabilizing function (Kristic et al., 1995), Eq. (12) can be expanded as follows.

$$\dot{V}_1 = x_e(\dot{x}_{ref} - \alpha_{Ux}) + y_e(\dot{y}_{ref} - \alpha_{Uy}) + \gamma_\psi \psi_e(\dot{\psi}_{ref} - \alpha_r) + x_e e_{Ux} + y_e e_{Uy} + \gamma_\psi e_r \tag{14}$$

Here, $e_{Ux} = \alpha_{Ux} - U_x, e_{Uy} = \alpha_{Uy} - U_y$, and $e_r = \alpha_r - r$

The following control rules were selected in Step 1 based on Eq. (14).

$$\begin{bmatrix} \alpha_{Ux} \\ \alpha_{Uy} \\ \alpha_r \end{bmatrix} = \begin{bmatrix} \dot{x}_{ref} + k_x x_e \\ \dot{y}_{ref} + k_y y_e \\ \dot{\psi}_{ref} + k_\psi \psi_e \end{bmatrix} \tag{15}$$

Here, $k_x, k_y, k_\psi > 0$ is a design variable.

If Eq. (15) is inserted into Eq. (14),

$$\dot{V}_1 = -k_x x_e^2 - k_y y_e^2 - k_\psi \psi_e^2 + x_e e_{Ux} + y_e e_{Uy} + \psi_e e_r \tag{16}$$

Step 2. In this step, a Lyapunov function candidate is selected, as shown below.

$$V_2 = V_1 + \frac{1}{2}\left(e_u^2 + e_v^2 + \gamma_r e_r^2\right) \tag{17}$$

Here, $e_u = \alpha_u - u, e_v = \alpha_v - v$, and $\begin{bmatrix} \alpha_u \\ \alpha_v \end{bmatrix} = P_b^{n'} \begin{bmatrix} \alpha_{Ux} \\ \alpha_{Uy} \end{bmatrix}$, $\begin{bmatrix} e_u \\ e_v \end{bmatrix} = P_b^{n'} \begin{bmatrix} e_{Ux} \\ e_{Uy} \end{bmatrix}$

If Eq. (17) is differentiated and inserted into Eq. (10) and Eq. (16),

$$\begin{aligned} \dot{V}_2 = & -k_x x_e^2 - k_y y_e^2 - k_\psi \psi_e^2 + x_e(e_u \cos\psi - e_v \sin\psi) \\ & + y_e(e_u \sin\psi + e_v \cos\psi) + \psi_e e_r + e_u(\dot{\alpha}_u - f_u - b_u F_u) \\ & + e_v(\dot{\alpha}_v - f_v - b_v F_v) + \gamma_r e_r(\dot{\alpha}_r - f_r - b_r F_r) \end{aligned} \tag{18}$$

As a result, the final control input $[F_u, F_v, F_r]^T$ can be designed as follows.

$$\begin{bmatrix} F_u \\ F_v \\ F_r \end{bmatrix} = \begin{bmatrix} b_u^{-1}(\dot{\alpha}_u - f_u + k_u e_u + x_e \cos\psi + y_e \sin\psi) \\ b_v^{-1}(\dot{\alpha}_v - f_v + k_v e_v - x_e \sin\psi + y_e \cos\psi) \\ b_r^{-1}[\dot{\alpha}_r - f_r + \gamma_r^{-1}(k_r e_r + \psi_e)] \end{bmatrix} \tag{19}$$

Lemma 1. If the control rules are designed as in Eqs. (15) and (19) based on the model of the UUV's motion and dynamics given in Eqs. (9) and (10), it can be guaranteed that the robot maintains a given motion $(x_{ref}(t),\ y_{ref}(t),\ \psi_{ref}(t))$ in a stable manner.

Proof. The proof is simple. If Eq. (19) is inserted into Eq. (19) and expanded,

$$\begin{aligned} \dot{V}_2 = & -k_x x_e^2 - k_y y_e^2 - k_\psi \psi_e^2 - k_u e_u^2 - k_v e_v^2 - k_r e_r^2 \\ \leq & -\lambda V_2 \end{aligned} \tag{20}$$

Here, $\lambda = \min\left\{k_x, k_y, \gamma_\psi^{-1} k_\psi, k_u, k_v, \gamma_r^{-1} k_r\right\}$.

Hence, V_2 can be known to converge at 0 exponentially.

Remark 1. For the control input calculated in Eq. (19), the thrust corresponding to each thruster is calculated as follows based on the thruster arrangement shown in Fig. 7.

$$[F_{HT1}, F_{HT2}, F_{HT3}, F_{HT4}]^T = B'(BB')^{-1}[F_u, F_v, F_r]^T \tag{21}$$

Here, $B = \begin{bmatrix} \frac{\sqrt{2}}{2} & \frac{\sqrt{2}}{2} & \frac{\sqrt{2}}{2} & \frac{\sqrt{2}}{2} \\ -\frac{\sqrt{2}}{2} & \frac{\sqrt{2}}{2} & -\frac{\sqrt{2}}{2} & \frac{\sqrt{2}}{2} \\ -0.415 & 0.415 & 0.415 & -0.415 \end{bmatrix}$.

Finally, the control input for each thruster is calculated using the chart of thruster control input[1] vs. thrust provided by the thruster manufacturer based on the thrust of each thruster calculated in Eq. (21).

Remark 2. The controller design presented in this section is based on the premise that the model of the UUV's motion and dynamics is accurate. However, in the case of an actual system that has strong nonlinear dynamic properties, such as a UUV, it is quite difficult to accurately derive hydrodynamic coefficients in advance. To handle the uncertainty in systems that include such a modeling error, a robust and adaptive controller design is needed (Li, 2016 and references therein).

4.2 Experimental Study-Based TVC Method

Generally, UUVs have strong nonlinear dynamic properties owing to the environments in which they operate and their own kinematic properties. Furthermore, it is difficult to accurately simulate robot models in actual applications. Therefore, when applying the control techniques that were proposed in the previous section, precise motion control cannot be guaranteed.

To overcome these problems, this study performed field experiments to derive the formula for the relationship between the thruster control input and the robot's forward speed. Based on this formula, this study attempted to find a simple control method for handling current flowing in any direction.

In this study, the forward and backward thrust models for each horizontal thruster are the same, and the four thrusters are all arranged with left/right and front/back symmetry, as shown in Fig. 7. Furthermore, this study adopted an approach that groups HT_1 and HT_3 into one set and HT_2 and HT_4 into a separate set, and it applies the same control input to the two thrusters of each set. In this case, the thrust vector of the thruster set located in the $l_{1,3}$ line is always placed at $l_{2,4}$; conversely, the thrust vector of the thruster set in the line is always located at $l_{1,3}$.

Based on this concept, the formula for the relationship between the speed and control input $C_{input} = vel2vol(U)$[2] was found by applying different control inputs to the HT_1, HT_3 set (it is possible to apply the same relational formula to the HT_2, HT_4 set) in a water tank environment and measuring the robot's corresponding speed (Li et al. 2019a). Based on this empirical relational formula, the following control rule is proposed.

Lemma 2. For a given arbitrary current (U_{cur}, ψ_{cur}), the current can be overcome if the following control rules are designed.

$$C_{input13} = vel2vol(U_{1,3}), \quad C_{input24} = vel2vol(U_{2,4}) \tag{22}$$

Here,

$$U_{1,3} = -U_{cur}\sin\left(\psi_{cur} - \psi - \frac{\pi}{4}\right), \quad U_{2,4} = U_{cur}\cos\left(\psi_{cur} - \psi - \frac{\pi}{4}\right).$$

Proof. Below is the speed vector U, which is composed of $U_{1,3}$ and $U_{2,4}$, which were calculated by Eq. (22) based on Fig. 7.

$$\begin{aligned} U &= U_{1,3}\csc\left(\psi + \frac{\pi}{4} - \psi_U\right) = U_{2,4}\sec\left(\psi + \frac{\pi}{4} - \psi_U\right) \\ &= -U_{cur}\sin\left(\psi_{cur} - \psi - \frac{\pi}{4}\right)\csc\left(\psi + \frac{\pi}{4} - \psi_{cur} + \pi\right) \\ &= -U_{cur} \end{aligned} \tag{23}$$

As a result, when the control input for a given current is designed, as shown in Eq. (22), the UUV is able to maintain the existing attitude.

In order to control the attitude on the robot's horizontal plane while overcoming a given current, the following simple proportional derivative (PD) technique was used.

$$\begin{aligned} C_{input1} &= vel2vol(U_{1,3}) + \delta C \\ C_{input3} &= vel2vol(U_{1,3}) - \delta C \\ C_{input2} &= vel2vol(U_{2,4}) - \delta C \\ C_{input4} &= vel2vol(U_{2,4}) + \delta C \end{aligned} \tag{24}$$

Here, $\delta C = K_P(\psi_{ref} - \psi) + K_D(\dot{\psi}_{ref} - r)$, and K_P and K_D are design variables.

Remark 3. The core of the TVC algorithm proposed in this section involves finding the formula for the relationship between the control input and the speed $C_{input} = vel2vol(U)$. In this study, the robot platform has both front/back and left/right symmetry, and it is possible to use the simple algorithm above when employing a method that divides the four horizontal thrusters into two sets, and applies the same control input to the two thrusters of each set. However, in the case of normal UUVs, it is very difficult to find formulas for the relationships between the control inputs for various situations and the corresponding speeds, and the use of the above control method will certainly be limited.

4.3 Simulation Study

A simulation was performed in Matlab using the robot's dynamic properties, which are expressed in Eq. (10), as well as the coefficients in Tables 3-5.

4.3.1 Maximum forward speed test

First, a 4.5-V control input (in the water tank experiments, a

1) Charts illustrating the relationship between thruster control input and thrust are often not provided by the thruster manufacturer. In such cases, the chart must be created by the researcher in order to perform precise control.

2) In this study, the thruster control input was a voltage value between (−5 V, +5 V).

maximum control input of ±4.5 V was proposed to protect the thrusters) was applied to all four thrusters to estimate the maximum forward speed.

As seen in Fig. 8, the maximum forward speed is around 2.36 m/s. This is the result of using the simplified model, and it ignores the effects of using the tether cable, etc. as in the water tank experiments. In the actual water tank experiments, a maximum forward speed of 1.85 m/s was obtained.

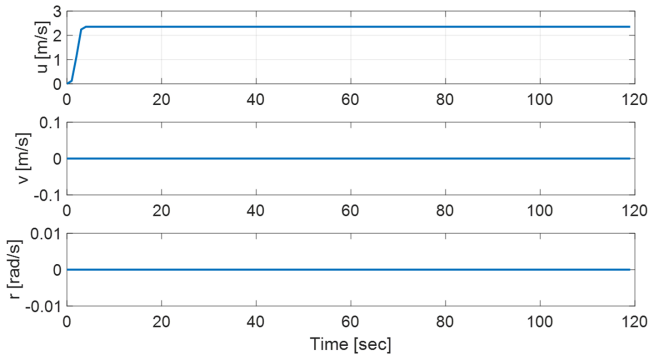

Fig. 8 Maximum forward speed simulation result

4.3.2 Path tracking with rotating motion

Owing to the structural properties of the robot platform, it is of interest to examine whether the platform can rotate at the same time

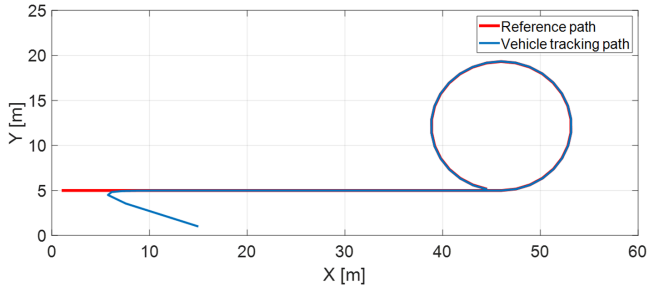

Fig. 9 Vehicle path tracking simulation result

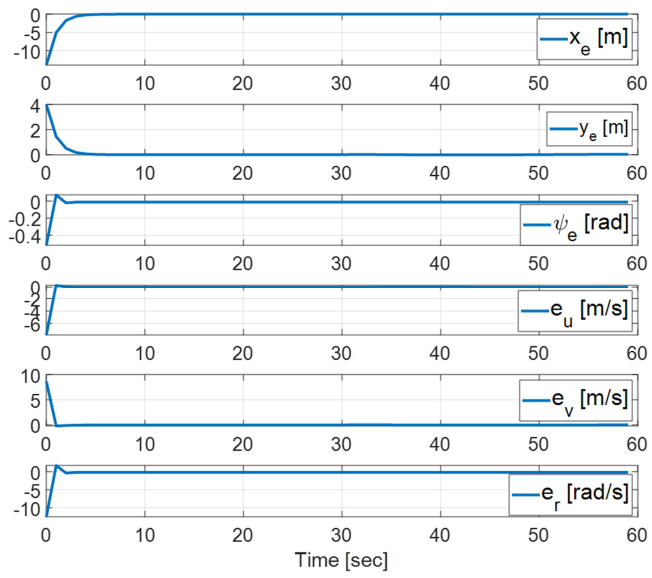

Fig. 10 Path tracking error convergence

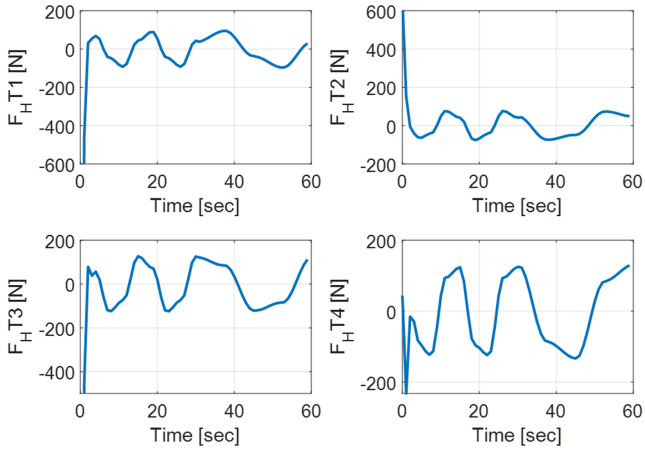

Fig. 11 Path tracking control inputs (thrust forces)

that the robot's center point traces a given path. To this end, the following simulation was performed. $[\dot{x}_{ref}, \dot{y}_{ref}, \dot{\psi}_{ref}] = [1.5\cos\theta(t), 1.5\sin\theta(t), 2\pi/15]$, and here $x_{ref}(0) = 1$ m, $y_{ref}(0) = 5$ m, $\psi_{ref}(0) = 0$, if $t < 0$, $\theta(t) = 0$; else $\theta(t) = 12°/s$. The robot's initial conditions are $x(0) = 15$ m, $y(0) = 1$ m, $\psi(0) = 30°$, $u(0) = v(0) = r(0) = 0$. For the control algorithm in the simulation, the technique introduced in section 4.1 was used, and the specific design variables are as follows.

k_x, $k_y = 1$, $k_u = k_v = 15$, $k_r = 25$, $\gamma_\psi = 1$, $\gamma_r = 5$.

The simulation results are shown in Figs. 9–11. Fig. 9 shows the given path and the path tracking for this path, and Fig. 10 shows the path tracking error. It can be seen that all results converged on 0 exponentially. Fig. 11 shows the calculated final control input.

5. Water Tank Experimental Studies

To verify the performance of the developed robot platform, i.e., its stability in the horizontal plane and its forward speed and performance

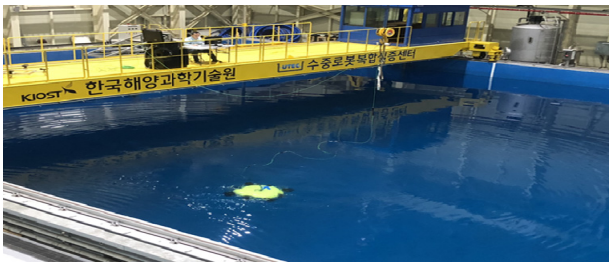

(a) Basin test

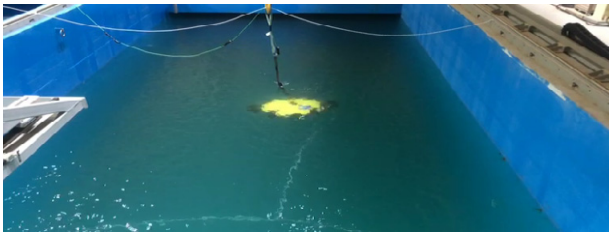

(b) Circulating water channel test

Fig. 12 Water tank test setup

in the horizontal plane, and to verify the ultimate performance of the proposed control algorithm, various experiments were performed at the Korea Institute of Ocean Science and Technology's Underwater Robot Test Center (Kim et al., 2017). The water tank tests verified the robot's performance at overcoming current using the TVC algorithm, which was mainly introduced in section 4.2. The water tank tests were broadly divided between an engineering basin and a circulating water channel, as shown in Fig. 12.

5.1 Basin Tests

5.1.1 Depth and roll, pitch motion control

First, in order to verify the platform's stability and general control performance, its depth, roll, and pitch control performance were examined.

As seen in Figs. 13–14, it was found that the platform is capable of rapid stable control according to the given depth, roll, and pitch control commands. Fig. 14 focuses on the control response speed to step-shaped reference values for the roll and pitch angles, and it appears that the platform's tracking performance is somewhat poor because it does not have an adequate response time. However, in separate independent roll and pitch angle control experiments, it was found that the values converged in a stable manner within approximately 3° after around 10 s had elapsed.

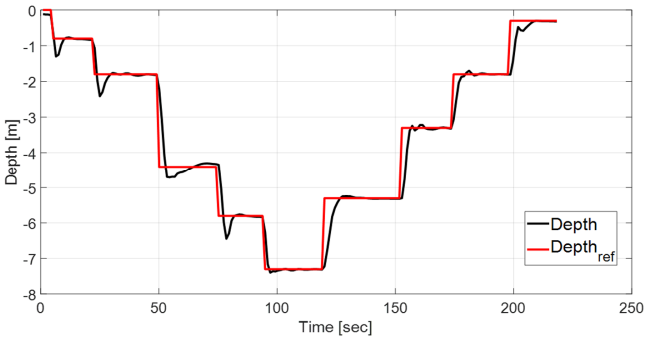

Fig. 13 Depth control performance

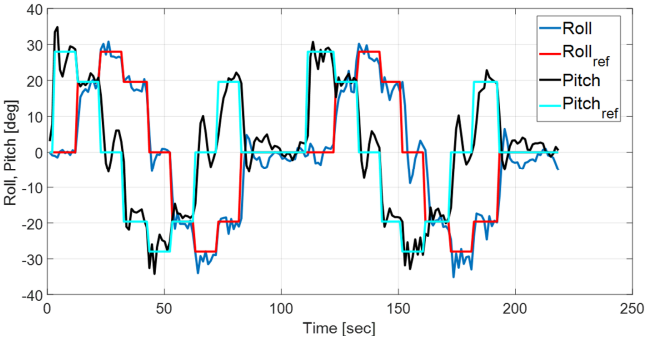

Fig. 14 Roll and pitch motion control performances

5.1.2 Heading keeping while encountering variant current

The following experiment was performed to examine the UUV's attitude angle keeping (heading-keeping) in scenarios where the current direction changed over time. The given attitude angle was $\psi_{ref} = 20°$, and a time-varying current was simulated as follows: $U_{cur} = 0.5$ m/s, if $0 \le t < 15$ or $t \ge 45$, $\dot{\psi}_{cur}(t) = 12°/s$; $else\ \dot{\psi}_{cur}(t) = -12°/s$; else, $\psi_{cur}(0) = 120°$.

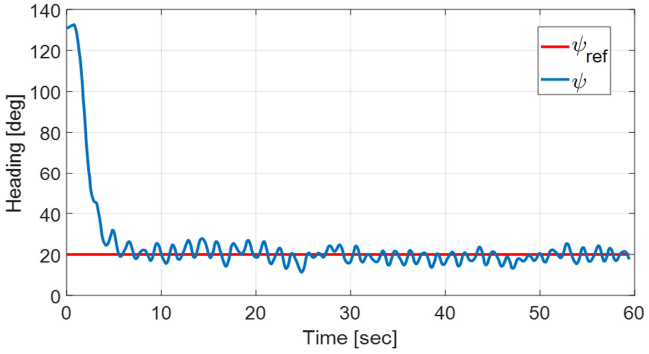

Fig. 15 Heading keeping performance

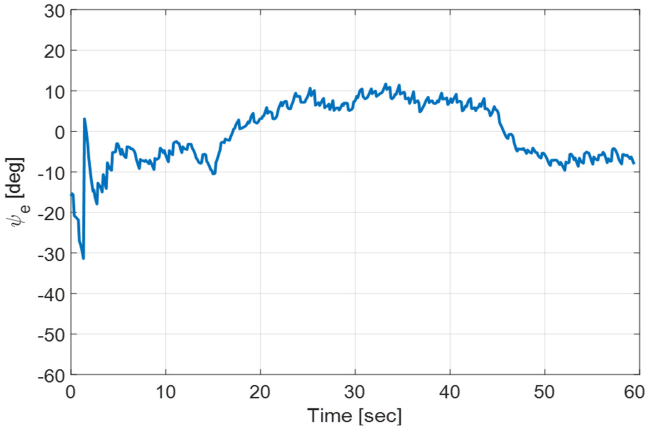

Fig. 16 Current tracking performance

The experiment results are shown in Figs. 15–16. Fig. 15 shows the heading keeping error, and Fig. 16 shows the current direction tracking error $\psi_e = -\psi_{cur} - [\psi + atan2(v,u)]$. Here, $\psi_U = \psi + atan2(v,u)$ is the robot's forward direction (Fig. 7). In Fig. 16, it can be seen that ψ_e has an error of around 10°. This is believed to be due to the accuracy of the $vel2vol(\cdot)$ function mentioned in section 4.2, as well as the attitude angle error of the MEMS-based AHRS and the effect of drift.

5.2 Circulating Water Channel Tests

To verify the stability and control performance of the platform in an actual current environment, various control experiments were performed on the robot in a circulating water channel with a flow speed of around 0.62 m/s (refer to Fig. 12(b)).

First, as in the basin tests, the platform's depth and attitude control performance were examined. As seen in Figs. 17–18, the depth and attitude angles were tracked well overall, but the results had more fluctuations than those of the basin tests. Next, tests were performed on attitude control for a ψ_{ref} that deviated from the current direction in the current environment, as well as the forward motion in the corresponding direction. As shown in Fig. 19, the robot converged to within ±5° of the given value of ψ_{ref}. The current speed and the robot's forward speed relative to the water tank floor that was measured at this time are shown in Fig. 20. It can be seen that the robot

made forward progress as it overcame the current, and this was also confirmed visually.

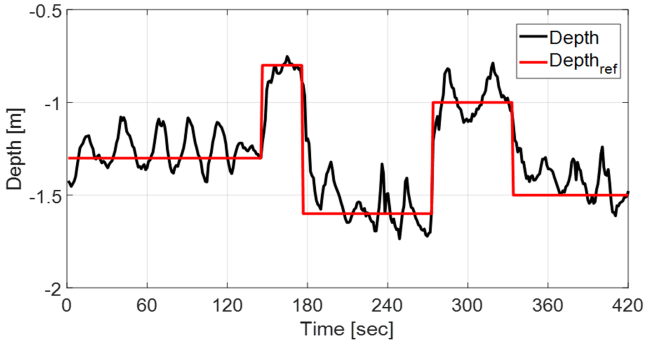

Fig. 17 Depth keeping performance with 0.62 m/s current

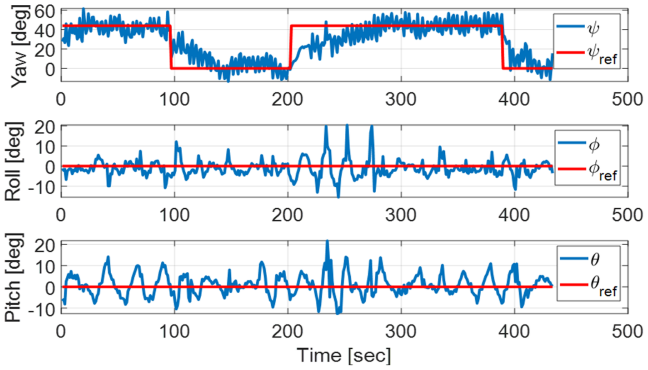

Fig. 18 Attitude control performance with 0.62 m/s current

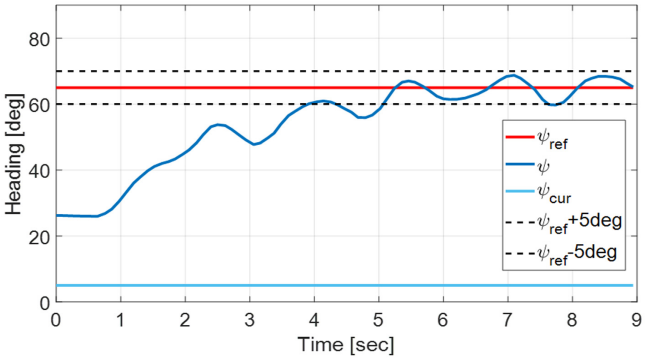

Fig. 19 Heading control performance with 0.62 m/s current

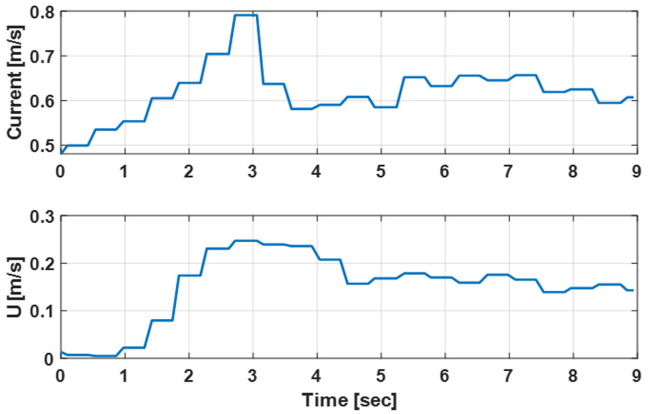

Fig. 20 Vehicle's forward speed

6. Conclusion

This paper discussed the design of an unmanned underwater vehicle (UUV) platform that overcomes strong currents, as well as a corresponding effective control method. To minimize drag underwater, the UUV's exterior was designed with a streamlined circular shape, and the size of the UUV was minimized through the optimal arrangement of the equipment and by designing and analyzing the mechanical systems in advance. A platform profile and empirical equations for the designed platform were used to create a simplified dynamics model and corresponding hydrodynamic coefficients, and these were used in a simulation study. This paper proposed an efficient and simple TVC algorithm by performing field experiments; after finding the formulas for the relationship between the platform's control input and forward speed based on a structure in which the four horizontal thrusters on the disc-shaped robot platform all had front/back and left/right symmetry, the same forward/backward propulsion model was used. The ultimate performance of the developed platform and control algorithm was verified in a water tank and circulating water channel environments.

Because stable control is needed to operate in irregular current environments, the control difficulties that were found in Prototype-II were resolved by varying the performance, number, and location of the vertical thrusters. In doing so, the overall drag was increased and the maximum forward speed was reduced from 2.16 m/s to 1.85 m/s, but control stability in the horizontal plane was significantly improved. Hence, more stable attitude control was possible in the water tank experiments, especially in the circulating water channel experiments.

One limitation of this study was that the thrusters used were all off-the-shelf products, which had limitations concerning their weight and exterior shapes and hence could not maximize the vehicle's speedIt is believed that if a propulsion system that is specialized for disc-shaped platforms is used, it will be possible to create a more effective technology for overcoming strong current.

Funding

This research was supported by the project titled "Development of Underwater Robot Platform and its Control Technology to Overcome up to 3.5 knots of Sea Current," which was funded by the Ministry of Oceans and Fisheries (MOF) and the Korea Institute of Marine Science and Technology promotion (KIMST), Korea (20160148). In addition, it was partially supported by the project No. 17-CM-RB-16 titled "Development of Multi-sensor Fusion based AUV's Terminal Guidance and Docking Technology," which was funded by the Agency for Defense Development (ADD) in South Korea.

Conflict of Interest

No potential conflict of interest relevant to this article was reported.

References

Fossen, T.I. (2002). Marine Control Systems－Guidance, Navigation, and Control of Ships, Rigs and Underwater Vehicles. Trondheim, Norway: Marine Cybernetics.

Kim, J.H., Sitorus, P.E., Won, B.R., Le,T.Q., Ko, J.H., Kim, D.Y., & Jang, I.S. (2017). A Flow-Visualization Study of a Multiple Hydrofoils Duct with Particle Image Velocimetry Equipment in KIOST. Proceedings of the 12th International Symposium on Particle Image Velocimetry, Busan, Korea.

Krstic, M., Kanellakopoulos, I., & Kokotovic, P. (1995). Nonlinear and Adaptive Control Design. New York: John Wiley & Sons, Inc..

Jun, B.H., Shim, H., Kim, B., Park, J.Y., Baek, H., Yoo, S., & Lee, P.M. (2013). Development of Seabed Walking Robot CR200. Proceedings of MTS/IEEE Oceans Bergen 2013, Bergen, Norway.

Li, J.H. (2016). Path Tracking of Underactuated Ships with General form of Dynamics. International Journal of Control, 89(3), 506-517. https://doi.org/10.1080/00207179.2015.1083123

Li, J.H., Kim, M.G., Kang, H.J., Lee, M.J., Jee, S.C., Park, M.J., ... Cho, G.R. (2019a). Development of Underwater Robot Platform and its Control Technology to Overcome up to 3.5 knots of Sea Current (R&D 2016-0148). KIMST.

Li, J.H., Kim, M.G., Kang, H.J., Lee, M.J., & Cho, G.R. (2019b). UUV Simulation Modeling and its Control Method: Simulation and Experimental Studies. Journal of Marine Science and Engineering, 7(4), 89. https://doi.org/10.3390/jmse7040089

Moon, Y.S., Sur, J. Ko, N.Y., Kim, H.S., & Park, Y.G. (2009). Design of Mine Robot Platform. Korea Robotics Society Review, 6(4), 64−71.

Newman, J.N. (1977). Marine Hydrodynamics. Cambridge, MA: The MIT Press

Prestero, T. (2001). Verification of a Six-degree of Freedom Simulation Model for the REMUS Autonomous Underwater Vehicle (Masters Thesis). Department of Ocean Engineering and Mechanical Engineering, MIT.

Pyo, J., & Yu, S.C. (2016). Development of AUV (MI) for Strong Ocean Current and Zero-visibility Condition. Proceedings of 2016 IEEE/OES Autonomous Underwater Vehicles, 54−57. https://doi.org/10.1109/AUV.2016.7778720.

Yoo, S.Y., Jun, B.H., & Shim, H. (2014). Design of Static Gait Algorithm for Hexapod Subsea Walking Robot: Crabster. Transactions of the Korean Society of Mechanical Engineers A, 38(9), 989−997. https://doi.org/10.3795/KSME-A.2014.38.9.989

Author ORCIDs

Author name	ORCID
Kim, Min-Gyu	0000-0001-8517-6352
Kang, Hyungjoo	0000-0001-8838-3285
Lee, Mun-Jik	0000-0001-7806-3237
Cho, Gun Rae	0000-0002-8536-4844
Li, Ji-Hong	0000-0002-5162-2737
Kim, Cheol	0000-0003-1160-5585

Appendix

Mechanical Dimensions of Prototype-III

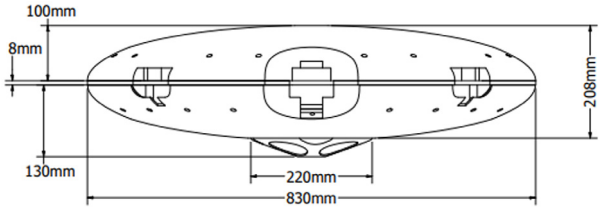

Fig. A1 Platform external dimensions

Table A1 Instruments weights and arrangements

Equipment	Weight (kg)	Position (x,y,z)
ADCP	4.62	(0,0,129.9)
AHRS	0.012	(110,0,0)
Horizontal thruster	3.5	(370,370,0), (-370,370,0),
Horizontal duct	0.72	(370,-370,0), (-370, -370,0)
Vertical thruster	2.4	(415,0,0), (-415,0,0),
Vertical duct	0.49	(0,415,0), (0,-415,0)

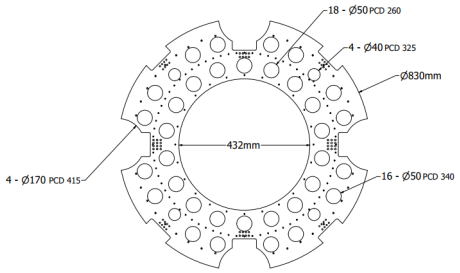

(a) Frame Dimensions

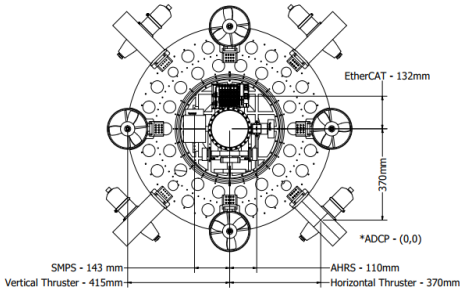

(b) Frame with instruments arrangements

Fig. A2 Frame dimensions and instruments arrangements

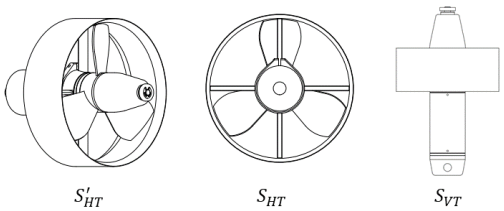

Fig. A3 Thrusters profiles

Table A2 Thrusters profiles area

Parameters	Surface area (mm^2)
S'_{HT}	34797
S_{HT}	19550
S_{VT}	22035

KSOE

Journal of Ocean Engineering and Technology 35(6), 446-456, December, 2021
https://doi.org/10.26748/KSOE.2021.065

pISSN 1225-0767
eISSN 2287-6715

Technical Article

A Study on Current Characteristics Based on Design and Performance Test of Current Generator of KRISO's Deep Ocean Engineering Basin

Jin Ha Kim[1], Jae Sang Jung[2], Seok Won Hong[1], Chun Ju Lee[1], Yong Guk Lee[3], Il Ryong Park[4] and In Haeng Song[5]

[1]*Principal Researcher, Korea Research Institute of Ship & Ocean Engineering (KRISO), Busan, Korea*
[2]*Senior Engineer, Korea Research Institute of Ship & Ocean Engineering (KRISO), Busan, Korea*
[3]*Junior Engineer, Korea Research Institute of Ship & Ocean Engineering (KRISO), Busan, Korea*
[4]*Professor, Department of Naval Architecture and Ocean Engineering, Don-Eui University, Busan, Korea*
[5]*Professor, Unit LINC, Korea Maritime & Ocean University, Busan, Korea*

KEY WORDS: Deep ocean engineering basin, Current generator, Model test, Seakeeping test, Impeller system

ABSTRACT: *To build an environment facility of a large-scale ocean basin, various detailed reviews are required, but it is difficult to find data that introduces the related research or construction processes on the environment facility. The current generator facility for offshore structure safety evaluation tests should be implemented by rotating the water of the basin. However, when the water in the large basin rotates, relatively large flow irregularities may occur and the uniformity may not be adequate. In this paper, design and review were conducted to satisfy the performance goals of the DOEB through computational numerical analysis on the shape of the waterway and the flow straightening devices to form the current in the large tank. Based on this, the head loss, which decreases the flow rate when the large tank water rotates through the water channel, was estimated and used as the pump capacity (impeller) design data. The impeller of the DOEB current generator was designed through computational numerical analysis (CFD) based on the lift surface theory from the axial-type impeller shape for satisfying the head loss of the waterway and maximum current velocity. In order to confirm the performance of the designed impeller system, the flow rate and flow velocity performance were checked through factory test operation. And, after installing DOEB, the current flow rate and velocity performance were reviewed compare with the original design target values.*
Finally, by measuring the current velocity of the test area in DOEB formed through the current generator, the spatial current distribution characteristics in the test area were analyzed. Through the analysis of the current distribution characteristics of the DOEB test area, it was confirmed that the realization of the maximum current velocity and the average flow velocity distribution, the main performance goals in the waterway design process, were satisfied.

1. Introduction

It is essential to secure domestic front-end engineering and design (FEED) technology to ensure international competitiveness in the offshore plant industry, as well as to direct the deep-sea resource development industry and the new offshore plant industry market. To contribute to the technological development of the domestic shipbuilding offshore plant industry, it is imperative to build a large-scale ocean engineering basin to verify the performance of offshore plants and structures. The Korea Research Institute of Ships and Ocean Engineering (KRISO) developed the world's largest deep-sea engineering water tank (100 m (length) × 50 m (breadth) × 15 m (depth)). It is equipped with complex equipment such as a wave maker, wind generator, current generator, depth control device, and towing carriage for the reproduction of the marine environment, including waves, wind, and current. The deep ocean engineering basin (DOEB) is used as a facility for design verification and performance/safety evaluation of existing oil and gas based on offshore structures and novel concepts for offshore plants.

The current generator is a major environment-reproducing facility and is useful for conducting motion and load characteristic tests on offshore structures. Offshore structures are significantly affected by the force of currents. The current force has an important influence on the structural characteristics, mooring lines, and risers. However, it is

Received 30 July 2021, revised 30 September 2021, accepted 7 October 2021
Corresponding author Jae Sang Jung: +82-51-604-7830, jsjung@kriso.re.kr

difficult to accurately predict the current force because the various fluidic interferences are rather strong.

Additionally, the current force has a significant influence on the motion characteristics of the structure and directly generates vortex-induced motions (VIM) in offshore structures (Finnigan et al, 2005; Lu et al, 2007). The current generator for the model test should consider the uniformity of the current, vertical current profile, and mutual interference between the waves and current. In particular, reproducing currents in deep-sea areas is an important issue, but it is quite difficult to consistently simulate currents for model tests. Because the flow is generated through a pump in the model test, relatively large flow irregularity may occur, and the uniformity may not be appropriate (Buchner and Wilde, 2008).

Because of these problems, the current flow uniformity of a large tank can be an important factor in a current load model test. However, it is difficult to find a study on a large tank current generator, which is not common. Therefore, it is necessary to consider how to circulate the tank water in a large tank to create a uniform flow. This study introduces a waterway shape design process to form uniform current flow and current velocity in a large tank and describes the design and installation process of an impeller system to rotate the water. Finally, after installation, the performance of the DOEB current generator was reviewed and compared with the design target factors.

2. Design of Current Generator in DOEB

2.1 Numerical Analysis for Design of Current Channel (Waterway) in DOEB

To implement a current generator that gyrates approximately 100,000 tons of water in the DOEB, the shape and specifications of the current channel and flow straightening devices for current uniformity were designed through numerical analyses. The main components and shape of the current channel of the DOEB across six stages of vertical waterway are shown in Fig. 1, which illustrates the culvert of the square guide pipe connected to a circular current pump pipe, guide vane located at the junction of the 90°-bend inside the culvert, mixing chamber, and current channel entrance. The mixing chamber is one of the important components in the current channel system for uniform current generation.

The water in the basin that is accelerated by the impeller of the current pump flows into the duct and culvert through the guide pipe and then exits into the basin through the mixing chamber, which has perforated walls and screens to generate a uniform current flow. The uniformity of the current flow in the test zone of the DOEB is very important for accurate offshore platform tests. To determine the shape and size of the current channel, the hydrodynamic performance of the current generation system was simulated through a computational fluid dynamics (CFD) approach. In this study, all simulations were carried out using the general-purpose software STAR-CCM+ (Siemens, 2018). The flow in the current channel was assumed to be turbulent and stationary.

The realizable k-ε turbulence model was employed for the turbulence closure of the Reynolds-averaged Navier-Stokes (RANS) equations. The SIMPLE (semi-implicit method for pressure linked equations) algorithm was used for the pressure-velocity coupling with the control of the overall solution. A second-order upwind scheme was used for the convection terms of the RANS equations, while a central difference scheme was applied to the diffusion terms.

To a certain extent, high flow velocities, velocity gradients, and turbulence intensities transferred by the pump decrease as the flow passes through the current channel system. However, relatively large-scale non-uniform flow structures can still be prominent, which makes it difficult to meet the required uniformity of the current flow in the basin. For this reason, the DOEB adopted perforated walls and screen structures that have some degree of solidity to make large-scale non-uniformities in the flow decay sufficiently and to control flow

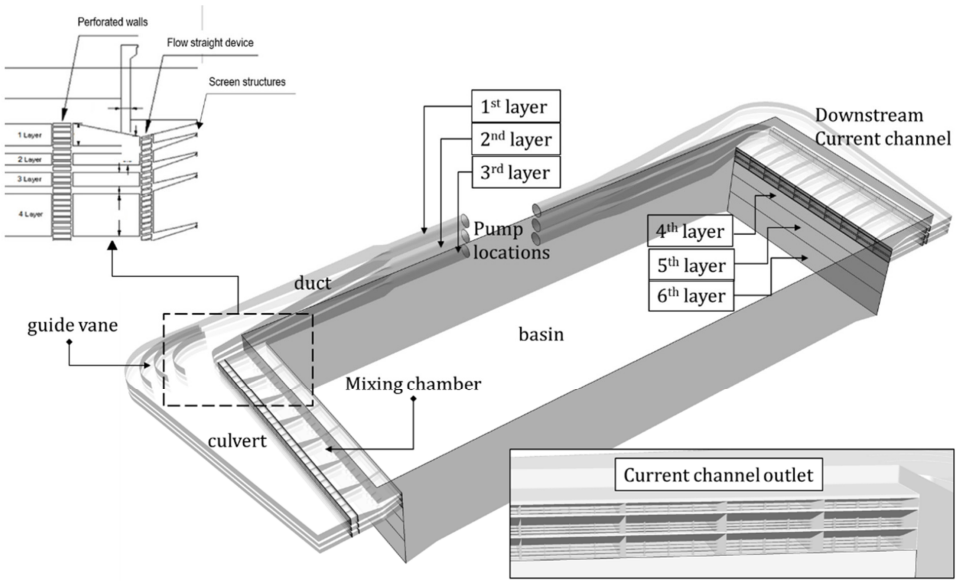

Fig. 1 Main components of the current generation system developed by KRISO

irregularities. The perforated walls are placed at the entrance of the mixing chambers and the exit of the tapered culvert section, while the screen structures are located at the entrance of the basin.

The present study used a screen model based on a wire mesh in the flow simulations to reproduce the solidity of the perforated walls and screen structures. The solidity of the wire mesh screen is easily calculated based on the diameter of wire and the size of mesh section (Lindgren and Johansson, 2002). This solidity effect can be modeled as an inertial resistance force term in the governing equations (Siemens, 2018) as follows:

$$f_p = P_v + P_i|\overline{V}| \tag{1}$$

where P_v is the viscous resistance, P_i is the inertial resistance, and $\overline{V}$ is the mean velocity through a perforated wall with a given degree of solidity. The current study neglected the viscous term and calculated the inertial resistance by using a pressure loss formula as follows:

$$P_i = \rho K_o \tag{2}$$

$$K_o = f(R_{ed})\frac{1-\beta^2}{\beta^2} \tag{3}$$

where ρ is the fluid density, K_o is the loss coefficient, R_{ed} is the Reynolds number based on the diameter of wire screen, and β is the solidity. $f(R_{ed})$ is a function of the pressure drop and has a converged value of 0.5 at $R_{ed} > 100$. More details of the numerical methodology can be found in a previous study (Park et al., 2014).

The computational domain was the DOEB itself. As shown in Fig. 2, the free surface in the DOEB was modeled as a symmetry plane without deformation. The inlet and outlet sections of the upper three current channel layers had the same velocity condition, which corresponds to the average velocity at the impeller plane generated by the pump at each layer. For the remaining lower three channel layers, constant inflow velocities were imposed at each channel exit to the basin. Wall boundary conditions were applied to all other surfaces of the DOEB.

The three less important lower channel layers were not included in the grid in order to reduce the complexity of the three-dimensional

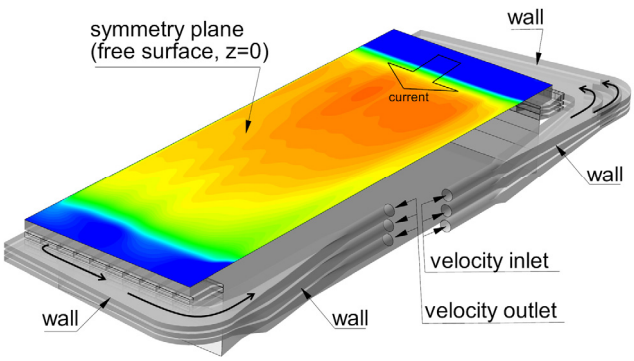

Fig. 2 Computational domain and boundary conditions

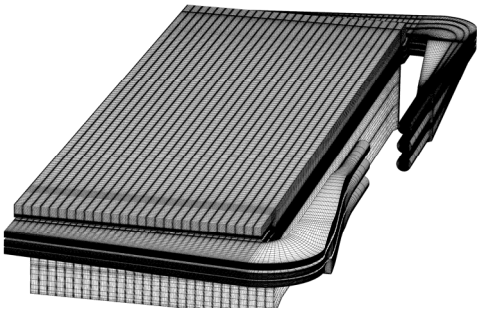

(a) Overall region

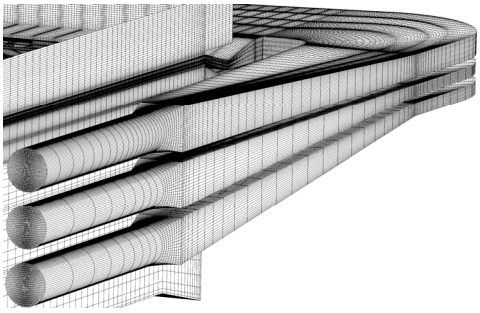

(b) Inlets and ducts

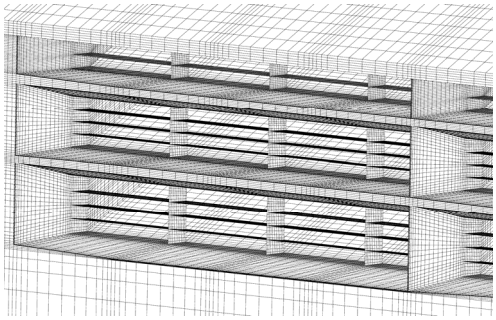

(c) Mixing chambers

Fig. 3 3D grid distribution of the current channel and DOEB

simulations and to avoid a massive increase of grid points. Except for neglecting the thickness of flow-embedded control surfaces, the generated grid considers every part of the current generation system without further geometrical assumptions. As can be seen in Fig. 3, which shows the grid distribution around the main parts, the current study used a multi-block structured grid with 11.0M (million) grid points.

Table 1 Average axial flow velocities at the impeller planes of six current channel layers.

Layer	Mean velocity (m/s)
1	3.60
2	3.47
3	3.22
4	3.22
5	2.50
6	0.59

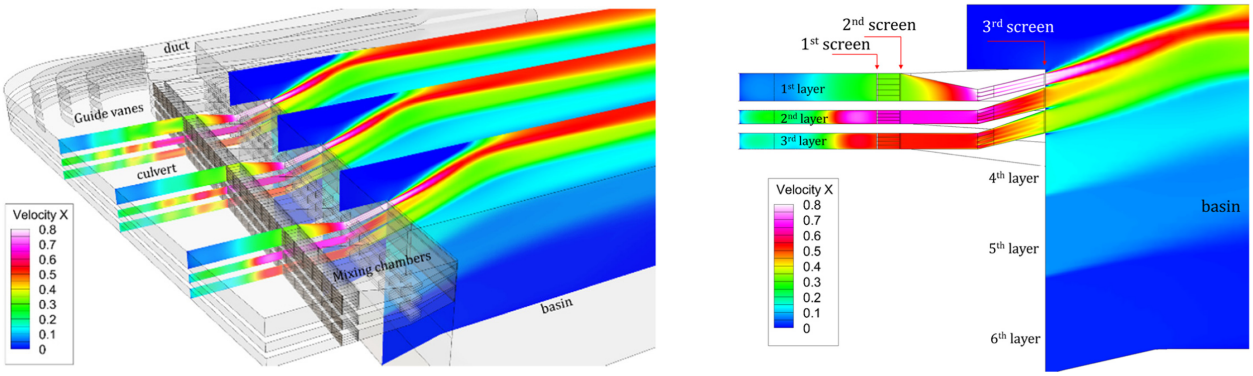

(a) (b)

Fig. 4 Streamwise velocity distributions on the selected vertical sections, x-z planes at y = 8 m, 15 m and 27 m (a), and x-z plane at y = 15 m with the description of the screens and channel layers (b)

In this study, the flow rate of the impellers and the solidity of the screen models should be determined for the generation of uniform current. Table 1 shows the average magnitude of the axial flow velocity at each impeller face of the current channel layers. These values were determined through numerical experiments to reproduce the target current speed of 0.5 m/s on the free surface in the basin.

Fig. 4 shows the streamwise velocity distributions on the selected vertical planes at y=8 m, 15 m, and 27 m in the DOEB. It is seen that the flows entering the culverts after turning 90° through the ducts are significantly complicated. After the flows passed through the screens and mixing chambers, a current with stratified flow velocity distribution in the depth direction was generated in the basin. The solidity values of the three screens from a previous study (Park et al., 2014)are shown in Fig. 4(b). The values required to generate the desired uniform current in the basin were determined to be 0.5, 0.83, and 0.5. A re-circulation flow region developed near the free surface above the 1st channel layer, and its length spanned 5.9 m from the exit of the channels. However, the effects of the re-circulation flow are not expected to be significant since the location of the model test zone is 50 m from the current channel exit.

Fig. 5 shows the streamwise velocity distribution of the generated current on the free surface and its profiles extracted at x = 50 m in the y direction. As shown in Fig. 5(a), re-circulation flow regions were formed in the upstream and downstream parts of the basin. The current speed slowed as the flow went downstream of the basin, but sufficiently constant current distribution was obtained over the measurement zone.

As shown in Fig. 5(b), the predicted streamwise velocity profile on the free surface at x = 50 m satisfies the extreme current speed target of 0.5 m/s. On the other hand, the uniformities of the velocity profiles below the free surface were slightly low. This can be overcome by using higher solidity, but it causes an increase in the head loss of the current pumps. In model tests, it is necessary to investigate the effects of the non-uniformity of the current below the free surface according to the draft of offshore structure models.

Fig. 6 shows a comparison of the vertical current profile. The target current profile in the figure was designed as an extreme case by referring to field data. The predicted profile was extracted in the z direction in the middle of the model test zone at x = 50 m and y = 17.5 m. The water depth influenced by the three upper current channel layers that were directly considered in the grid was about z = -5.8 m. Below this depth, the current profile was generated by a constant velocity inlet condition with an inclined angle imposed at the inflow

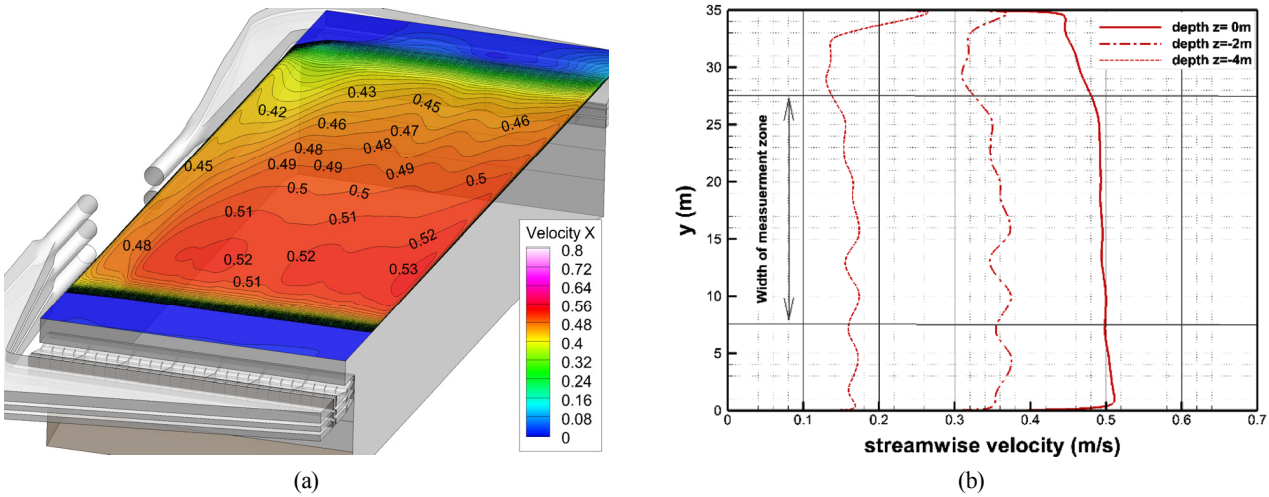

(a) (b)

Fig. 5 Streamwise velocity distribution on the free surface (a), and streamwise velocity profiles at different depths (b)

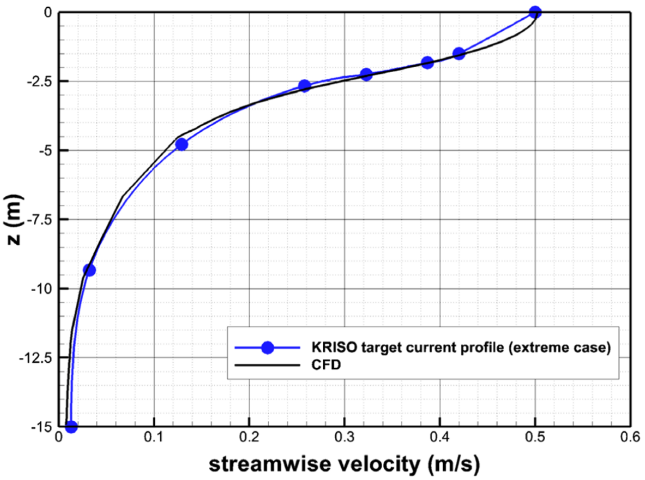

Fig. 6 Comparison of the predicted vertical current profiles and the design profile

Table 2 Head loss of current channel in the current generation system

Layer	Head loss (m)
1	3.60
2	3.47
3	3.22

section of each of the three lower current channel layers. Within the design capacity of the pump, the current generation system reproduced the design extreme current profile well and showed good agreement. Table 2 shows the calculated results of the head loss of the current channel at the design flow rate. The maximum head loss value was used for the pump capacity and impeller design.

2.2 Design of Current Generation System

The current generator is composed of a six-layer water channel

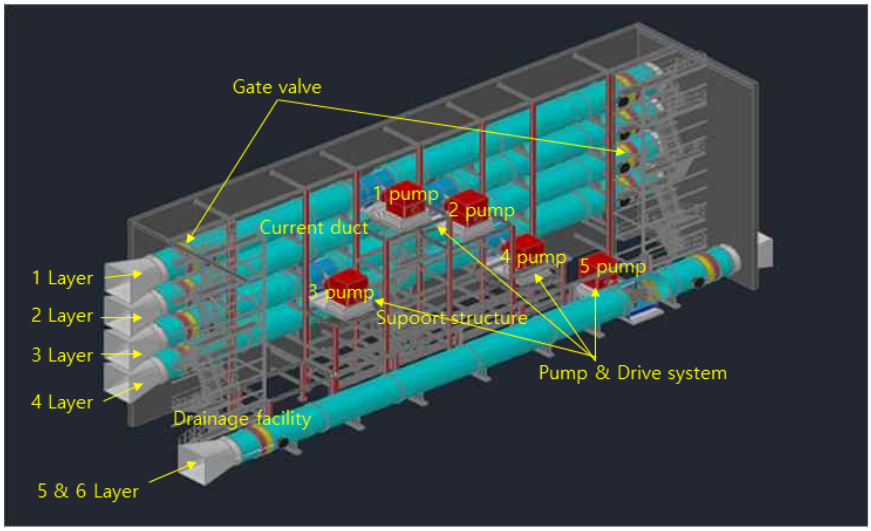

Fig. 7 Concept of current pump facility proposed by KRISO

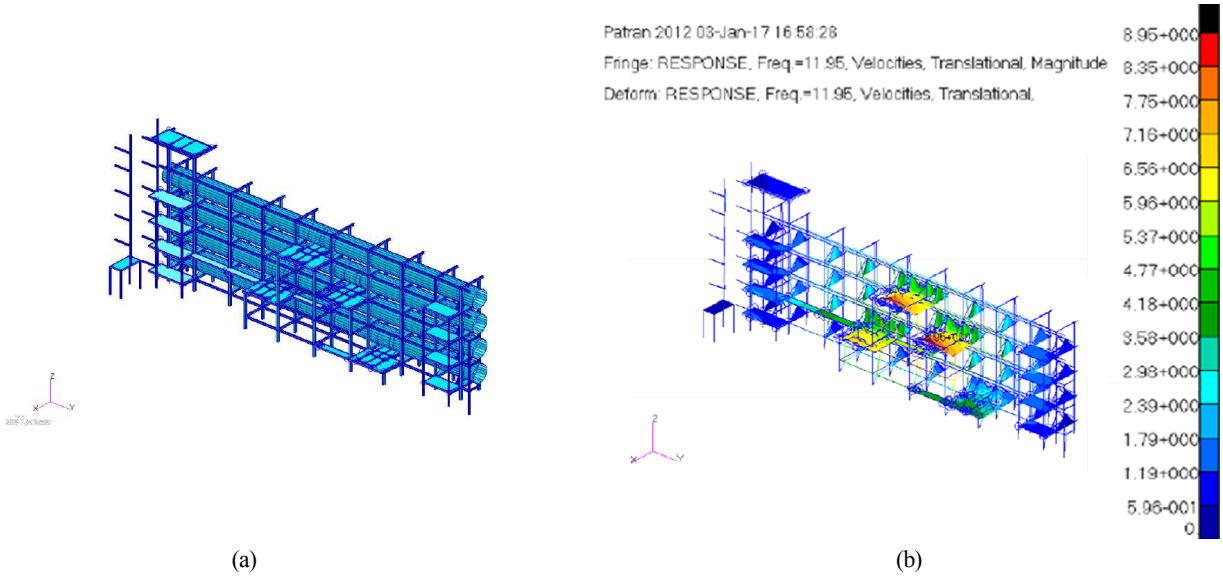

(a) (b)

Fig. 8 Modeling of structural analysis (a), and vibration analysis result for the maximum response frequency in the high frequency (magnitude velocity Freq. = 11.95 Hz) region (b)

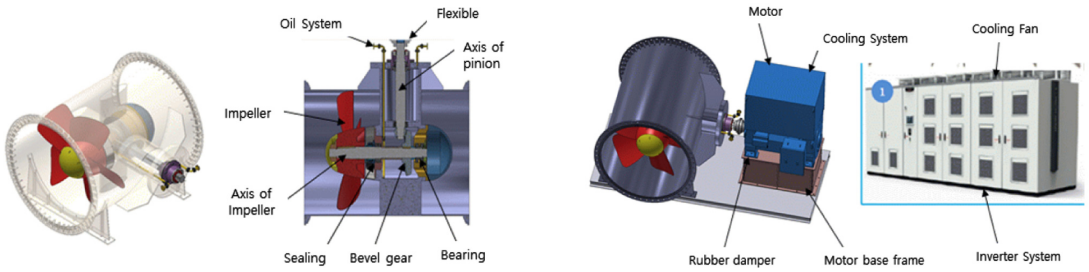

(a) (b)

Fig. 9 Configuration of current pump (a), and Configuration of current drive system (b)

aligned vertically to realize arbitrary current spatial distribution, and five current pump facilities (combining the lower current channel). A conceptual diagram of the current pump facility is shown in Fig. 7, and it is composed of a current duct, facility support structure, pump and drive system, drainage facility, electric unit, and operation control system. The current duct is a steel structure with a circular cross-section of sufficient strength and a support structure to withstand the self-weight and pressure of the basin. It ensures uniform circulation flow transfer, and each duct is connected in the form of a bolted flange. It was placed such that the waterway could be blocked with a gate valve. The current duct arrangement was designed in series with the two rows (five and six layer) forming one layer and the four layers being without inflections to minimize possible head loss.

The supporting structure supports static loads generated by the self-weight of the motors, impellers, and current ducts (when the generator is switched off), dynamic loads generated by driving the motors and impellers, and the duct flow, The supporting structure prevents damage to the duct system due to thermal deformation. For analyzing the strength of the supporting structure, as shown in Fig. 8, static and dynamic strength analyses were performed. In addition, an earthquake analysis was performed on the facility's supporting structure to verify the stability of the design values.

The figure on the left of Fig. 8 shows a model for structural stability analysis of the support structure arranged in the vertical direction from duct 1 to duct 4. Analysis was done modeled through MSC / PATRAN. In this case, 1,081 elements were used, and 70 nodes were used. The boundary condition of the vibration analysis model is the same as in the static analysis, and a constraint condition of 6-DOF motion for translational and rotational motion was applied to the part fastened to the basic anchor bolt.

The primary natural frequency obtained through natural frequency analysis of the supporting structure was 3.7332 Hz, and the main natural frequencies were 8.6308 Hz, 9.1378 Hz, 10.183 Hz, 10.454 Hz, 11.055 Hz, 11.544 Hz. 11.704 Hz, 11.89 Hz, 14.027 Hz, and 14.302 Hz. Among them, the result for 11.95 Hz is shown in Fig. 8 (right). Through vibration response analysis, the maximum displacement in the 1−5 Hz section were 0.053 mm, which was less than 1.0mm, which is the standard for DNV steel structures and satisfies the stability standard. In the case of the 5−15 Hz section, the maximum speed is 8.95 mm/s, which is lower than the 30 mm/s standard for DNV steel structures, which satisfies stability.

The current pump used are an axial pump that accelerates the circulating fluid. As shown in Fig. 9, it comprises an impeller, gear housing, bevel gear, impeller shaft, pinion shaft, flexible coupling, bearing, sealing, and lubricant system, and has a structure that can be completely sealed.

An axial-type impeller was selected based on the particular speed. The impeller was designed to have the best efficiency, good cavitation, and low vibration performance, and an azimuth thruster was selected because it has efficient maintenance. The number of blades was selected as five to absorb the high power density and avoid a resonance with a "+"-type stator system. Design conditions were selected according to the target profile (waterway capacity of 14.9 m^3/s and required head loss of 1.33 m) and to absorb the motor power. Two types of impellers were designed to ensure suitability for different loads due to the head loss across the flow layer. The first impeller type was designed for the second and third layers, and the second impeller type was designed for the first, fourth, and fifth layers.

The performance of the pump was predicted using a lifting-surface theoretical analysis, and the pitch and camber distribution were

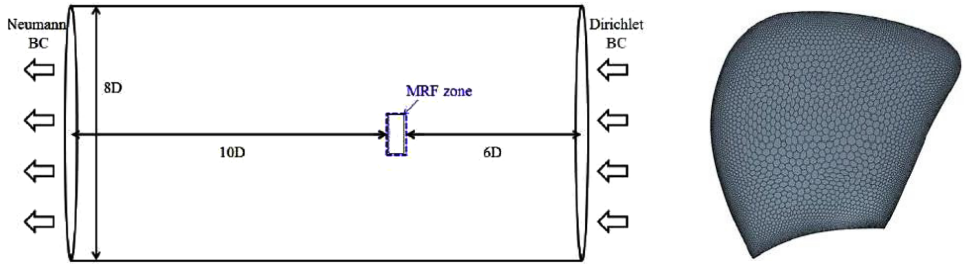

(a) (b)

Fig. 10 Computational region (a), Grid distribution of the impeller (b)

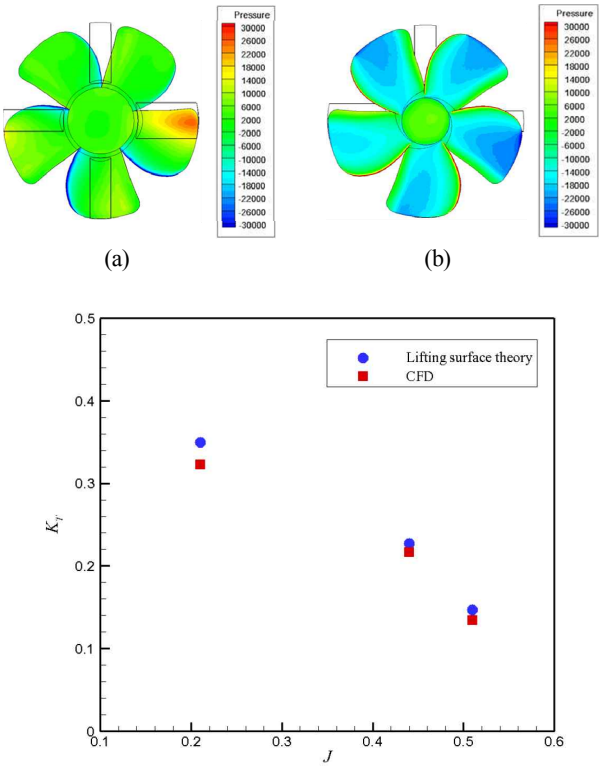

Fig. 11 Pressure distribution of impeller 1 obtained via CFD analysis: pressure side (a), and suction side (b), and result of single impeller performance analysis (c)

Table 3 Predicted performance of the impeller in channels 1 and 2

	Channel 1 (Impeller 2)		Channel 2 (Impeller 1)	
RPM	*Vd* (m/s)	DHO (kW)	*Vd* (m/s)	DHO (kW)
405	2.81	78.8	2.56	113.3
480	3.33	131.3	3.04	188.8
537	3.73	183.8	3.40	264.3
592	4.12	246.8	3.75	355.0

determined. The performance of the impeller in the channel was calculated based on the lift surface theory and CFD. The CFD turbulence model and discrete scheme were the same as those used for the aforementioned current channel analysis.

Fig. 10 shows the computational domain and grid distribution on the impeller surface for the single-impeller performance analysis. A hybrid mesh technique with polyhedral and trimmed meshes was employed due to the complex shape of the impeller. The polyhedral mesh was applied to the MRF rotating region, including the blade, while the trimmed mesh was used for the remaining region. To simulate the turbulent boundary layer, five prism layers were generated on the blade surface, and $y_P^+ \approx 30$ was considered as the position of the first grid point. As a result, the number of grid cells was 1.8 million for the overall region.

Fig. 11(a) and Fig. 11(b) show the pressure distributions on the pressure and suction sides of the blade, which were obtained after the impeller thrust and torque converged. Similar to the pressure distributions of a general thruster, the pressure increases at the leading edge of the blade while gradually decreasing toward the trailing edge. Fig. 11(c) presents the result of the single-impeller performance in terms of the thrust coefficient and advance ratio. The results of the non-viscous-based lift surface theory and the CFD analysis show the same physical trend. Based on this result, it can be confirmed that the CFD analysis results show similar accuracy to the lift plane theory. Table 3 shows the flow rates and the delivered horsepower (DHP) at various impeller revolutions per minute (RPM) for channel 1 with impeller 2 and for channel 2 with impeller 1.

2.3 FAT (Factory Test) of Current Generation System

Before installing the current pump, an FAT of the current pump was performed as shown in Fig. 12, to verify the performance and durability of the current pump. The FAT consisted of a leak test for the major parts, a pressure test for each section, and a performance test for the pump. The pump performance test was divided into 5 stages based on the different motor load values: 1/4, 2/4, 3/4, 4/4, and 11/10 times the initial motor load. The number of rotations for each load and, required shaft horsepower current, voltage, coolant temperature, and performance were analyzed by measuring the temperature and lubricant temperature.

As shown in Fig. 12 (b), the flow rate was measured by an ultrasonic system at three positions, V1 was at the inlet side, V2 was at the outlet side, and V3 was diametrically opposite the impeller. The measured flow rates at V1 are relatively low because V1 is far downstream from the impeller. The flow rate according to the RPM change was analyzed with respect to the FAT result of the pump performance, as shown in Fig. 13. The measured flow rates, except for pump #4 were stable for the various RPMs and are similar to the predicted flow rates.

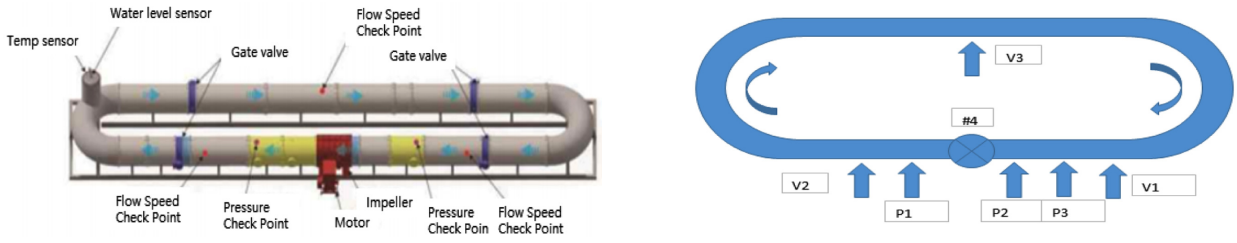

Fig. 12 Configuration of FAT (a), and configuration of sensors (b)

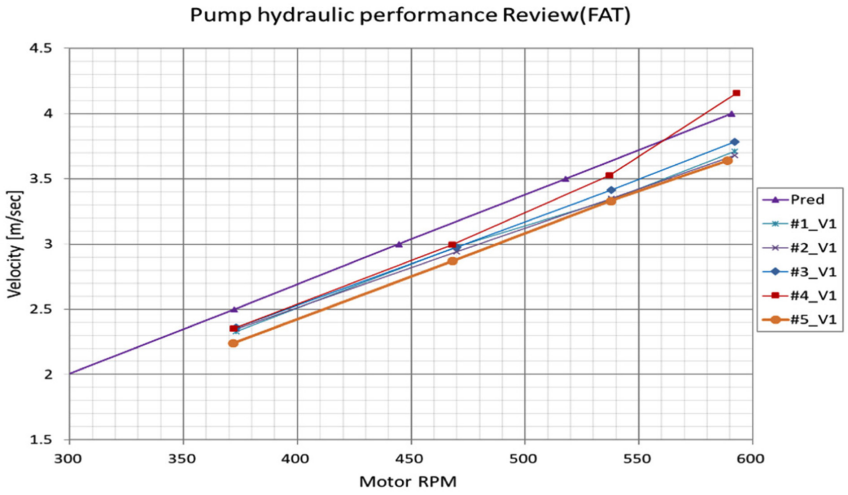

Fig. 13 Flow rate of the pump performance in FAT

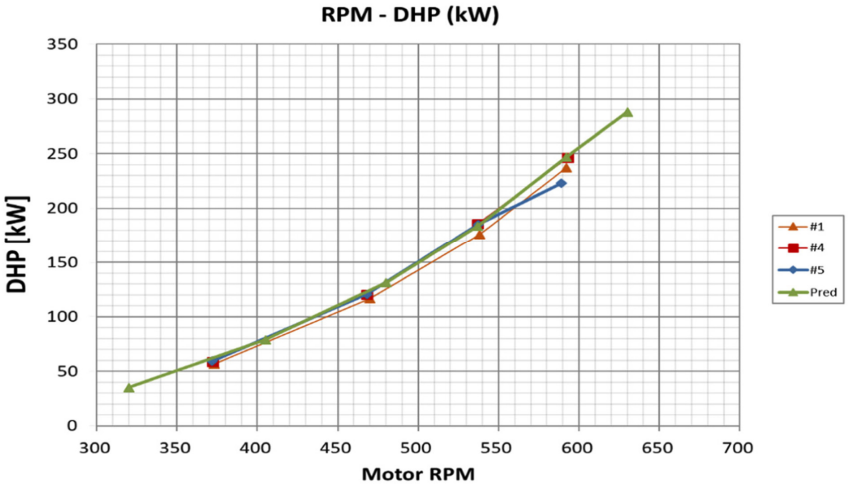

Fig. 14 DHP of pump performance in FAT

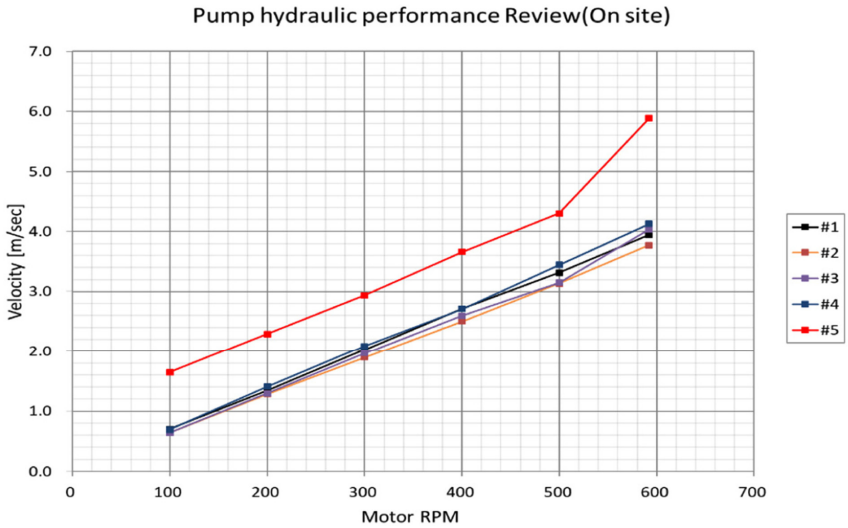

Fig. 15 Review of pump hydraulic performance test results after on-site installation in DOEB

The delivered horsepower (DHP) was obtained based on the motor output voltage and current obtained during the pump performance FAT. The DHP curves of impellers are shown in Fig. 14. These curves are in good agreement with the predicted value, which is at table 3 (impeller 2), dependent on the accuracy of the flow rates in FAT and impeller efficiency.

2.4 Installation and Testing of Current Generation System

The current generation system was installed in the current pump room of the DOEB, and all the inspections and durability tests were performed on the major components. Safety checks were conducted on the shafting alignment, electrical parts, and installation structures, which are the main components of the on-site installation of the current generation system. The shafting alignment is very important for stably driving the current generation system for a long duration. For this purpose, the single and interlock drives (with 5 pumps simultaneously) drives were performed for more than 8 h per day for 2 weeks, and the alignment status was checked by separating the shafting system.

After the completion of the stability check of the current generation system, a single pump performance test of pumps 1−5 was conducted, and the pump performance was reviewed by interlocking five pumps, as shown in Fig. 15, By interlocking five pumps. The performance of the pump was maintained at a maximum flow rate of 4 m/s. This result exceeds the CFD prediction result for the pump output flow rate for forming the target vertical profile as shown in Table 1. And there was no significant difference in the flow rate performance of the pump in the single and interlocking drives. However, an increase in the flow rate of pump #5 was observed during the FAT. This is because pump #5 is responsible for current channels 5 and 6 of the DOEB.

3. Analysis of the Current Characteristics in DOEB

3.1 Characteristics of Flow Rate of the RPM Current in the Current Generation System

According to the impeller drive of the DOEB current generation system, current is generated in the DOEB test area through the waterway. The experimental area of the DOEB is near the middle area of the DOEB, and the test area is set as shown in Fig. 16 to analyze the current velocity from the water depth.

The result of measuring the flow rate in the DOEB by increasing the RPM of the current pump facility is shown in Fig. 17. It can be seen that the flow rate is 0.56 m/s at the maximum RPM of the current

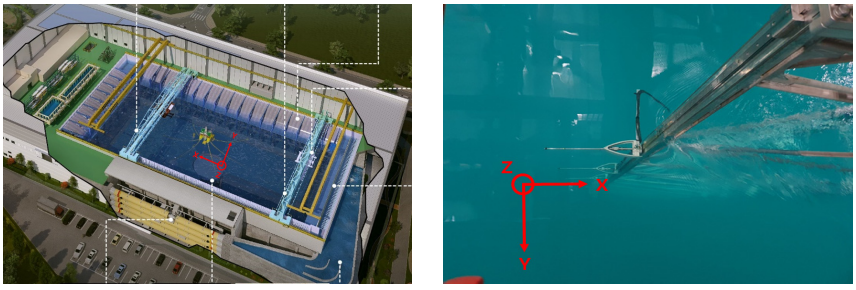

(a) (b)

Fig. 16 Aerial view of DOEB (a) and measurement location in DOEB and photo of current measurement (b)

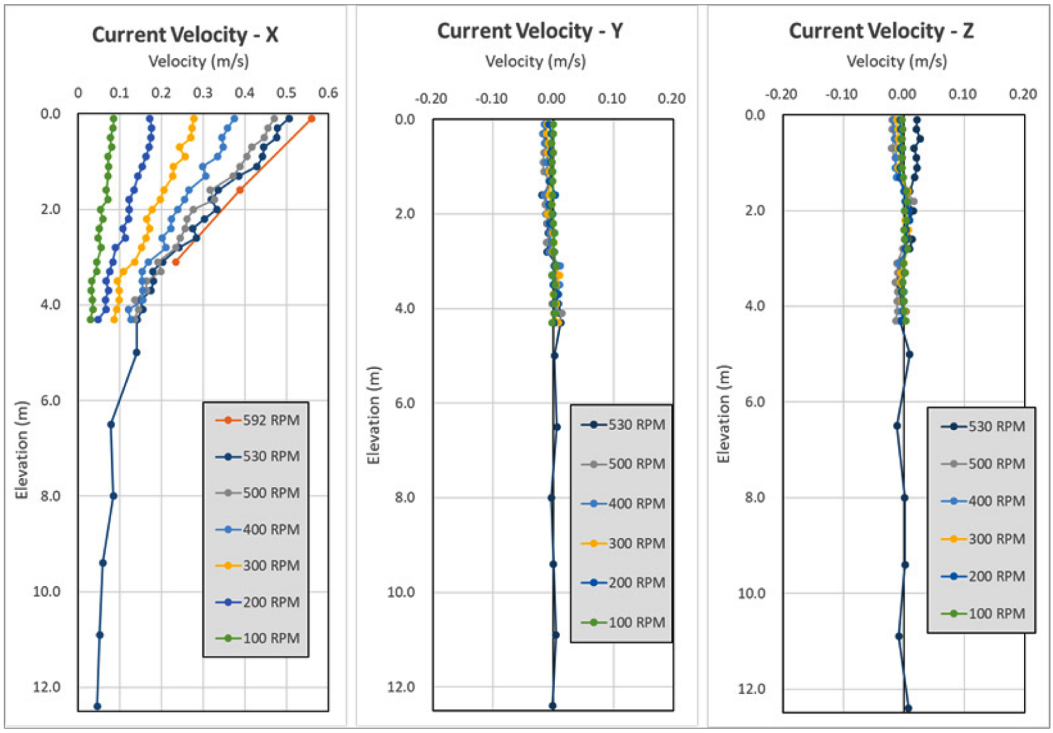

Fig. 17 Current velocity compared with RPM of the current pump facility in DOEB

pump facility, which exceeds the design target flow speed of 0.5 m/s. Based on these flow velocity results, the initial driving RPM can be estimated when the current velocity is reproduced for the following model test.

3.2 Spatial Area Characteristics of Current in DOEB

To investigate the distribution of the current velocity in the DOEB, the towing carriage was used, and the current velocity was measured as shown in Fig. 18. The error range of the average flow velocity distribution in the test area of the model test (10 m (width) × 10 m (length)) was within 5%. This confirms that the DOEB current channel waterway and the several turbulence control devices are working effectively.

As shown in Fig. 19, the turbulence intensity (T) was examined based on the equation obtained by Bas Buchner (Buchner and Wilde, 2008).

$$T = \sigma/V \quad (4)$$

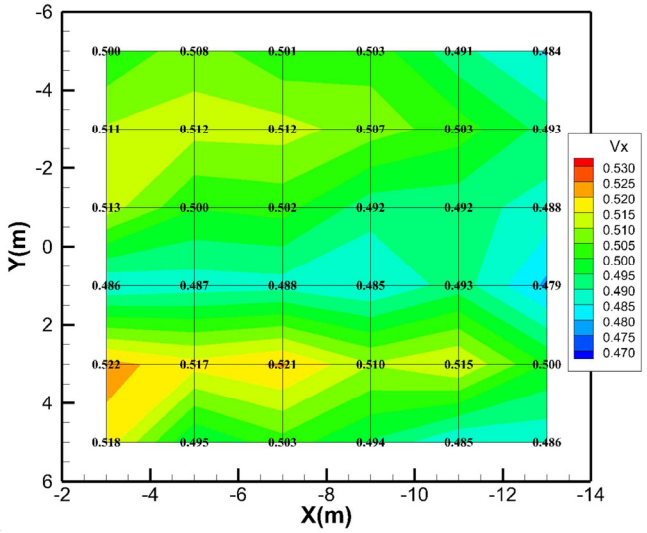

Fig. 18 Spatial distribution of current velocity on the surface of the DOEB

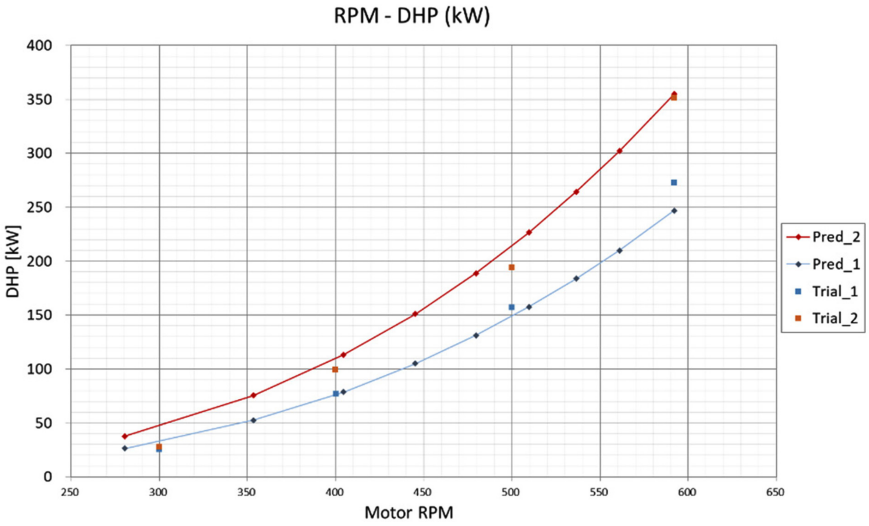

Fig. 19 Turbulence intensity (T) on the surface of DOEB

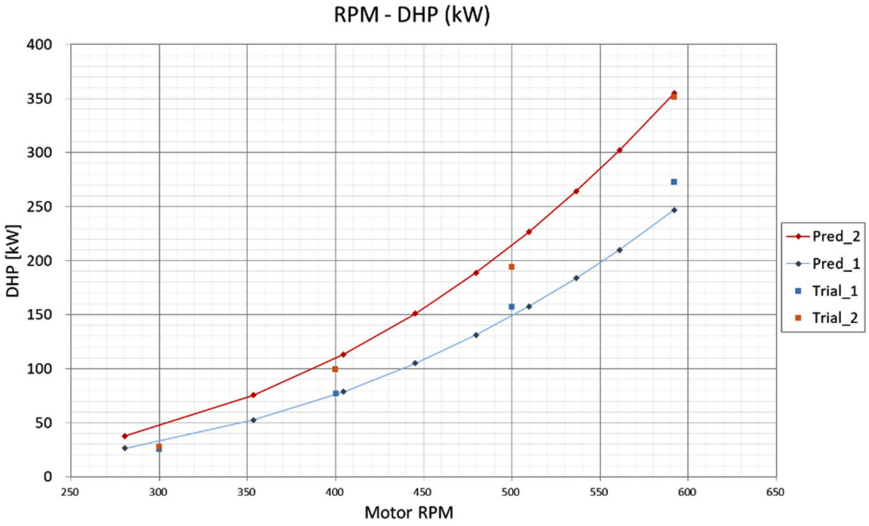

Fig. 20 DHP curves of the pump #1 and #2 during the performance test

where σ is the standard deviation of the velocity fluctuations, and V is the mean velocity.

It can be seen that the turbulence intensity of the current near the test area of the DOEB is 7~8%. A turbulence intensity improvement test was planned through a solidity change test of the turbulence grid (SUS screen) at the outlet. The performances of pump #1 and pump #2 plays a significant role in obtaining the target current velocity in the test section. Fig. 20 shows the DHP curves for pumps #1 and #2 during the performance test, and they are in good agreement with the predicted value.

4. Conclusions

In order to design the current generator in the DOEB of KRISO, a 3D numerical analysis was performed to evaluate the hydrodynamic performance of the current channel of the current generator. Based on the analysis results, the number of screen devices installed in the current channel, location of the installation, and distribution of current according to the solidity were reviewed, and the maximum flow velocity of current in the surface layer was obtained. The head loss of the current channel was also obtained.

The main components of impellers were designed based on the hydrodynamic performance of the current channel and verified through an FAT and pump hydraulic performance test in the DOEB. Finally, by measuring the characteristics of current generation in the DOEB test area, it was confirmed that the design performance target was satisfied. Further research will be conducted on the development of a turbulence control device for improving the current turbulence intensity and the current distribution characteristics in the DOEB data based on the depth.

Acknowledgments

This study was conducted by the “Deep Ocean Engineering Basin-based standard ocean structure performance evaluation technology development (3/3)” project, one of the major projects of KRISO (PES3920).

References

Buchner, B., & de Wilde, J. (2008). Current Modeling Experience in an Offshore Basin." Proceedings of the ASME 2008 27th International Conference on Offshore Mechanics and Arctic Engineering. Volume 4: Ocean Engineering; Offshore Renewable Energy. Estoril, Portugal, 417~424. https://doi.org/10.1115/OMAE2008-57597

Finnigan, T., Irani, M., & Van Dijk, RRT. (2005). Truss Spar VIM in Waves and Currents. Proceedings of the ASME 2005 24th International Conference on Offshore Mechanics and Arctic Engineering. 24th International Conference on Offshore Mechanics and Arctic Engineering: Volume 2. Halkidiki, Greece, 475~482. https://doi.org/10.1115/OMAE2005-67054

Lu, H., Yang, J., Peng, T., & Chen, Gang. (2007). Numerical and Experimental Research on Current Generation in Deep Water Offshore Basin. Journal of Hydrodynamics, 19(5), 551-558. https://doi.org/10.1016/S1001-6058(07)60152-8

Buchner, B., & de Wilde, J. (2008). Current Modeling Experience in an Offshore Basin." Proceedings of the ASME 2008 27th International Conference on Offshore Mechanics and Arctic Engineering. Volume 4: Ocean Engineering; Offshore Renewable Energy. Estoril, Portugal, 417-424. https://doi.org/10.1115/OMAE2008-57597

Park, I.R., Kim, J.H., Hong, S.W., & Sung, H.G. (2014) Numerical Investigation of Current Generation Performance in a Large Ocean Engineering. Proceedings of the Eleventh Pacific-Asia Offshore Mechanics Symposium. Shanghai, China.

Siemense. (2018). STAR-CCM+ 11.04 User Guide. Retrieved from https://support.industrysoftware.automation.siemens.com/general/documentation.shtml

Lindgren, B., & Johansson, A.V. (2002). Design and Evaluation of a Low-Speed Wind-Tunnel with Expanding Corners (Internal Report TRITA-MEK 2002:14). Stockholm, Swedon: Dept. of Mechanics, KTH.

Author ORCIDs

Author name	ORCID
Kim, Jin Ha	0000-0003-3856-9668
Jung, Jae Sang	0000-0001-7090-2382
Hong, Seok Won	0000-0001-5623-2562
Lee, Chun Ju	0000-0002-4600-1928
Lee, Yong Guk	0000-0002-3167-3553
Park, Il Ryong	0000-0002-6194-5716
Song, In Haeng	0000-0002-0371-8769

Instructions for Authors

General information

To submit a manuscript to the Journal of Ocean Engineering and Technology (JOET), it is advised to first carefully read the aims and the scope section of this journal, as it provides information on the editorial policy and the category of papers it accepts. Unlike many regular journals, JOET usually has no lag in acceptance of a manuscript and its publication. Authors that find a match with the aims and the scope of JOET are encouraged to submit as we publish works from all over the world. JOET adheres completely to guidelines and best practices published by professional organizations, including Principles of Transparency and Best Practice in Scholarly Publishing (joint statement by COPE, DOAJ, WAME, and OASPA (http://doaj.org/bestpractice) if otherwise not described below. As such, JOET would like to keep the principles and policies of those professional organizations during editing and the publication process.

Research and publication ethics

Details on publication ethics are found in http://joet.org/authors/ethics.php. For the policies on research and publication ethics not stated in the Instructions, Guidelines on Good Publication (http://publicationethics.org/) can be applied.

Requirement for membership

One of the authors who submits a paper or papers should be member of the Korean Society of Ocean Engineers (KSOE), except a case that editorial board provides special admission of submission.

Publication type

Article types include scholarly monographs (original research articles), technical articles (technical reports and data), and review articles. The paper should have not been submitted to other academic journal. When part or whole of a manuscript was already published to conference papers, research reports, and dissertations, then the corresponding author should note it clearly in the manuscript.

Copyright

After published to JOET, the copyright of manuscripts should belong to KSOE. A transfer of copyright (publishing agreement) form can be found in submission website (http://www.joet.org).

Manuscript submission

Manuscript should be submitted through the on-line submission website (http://www.joet.org). The date that manuscript was received through on-line website is the official date of receipt. Other correspondences can be sent by an email to the Editor in Chief or secretariat. The manuscript must be accompanied by a signed statement that it has been neither published nor currently submitted for publication elsewhere. The manuscript should be written in English or Korean. Ensure that online submission are in a standard word processing format. Corresponding author must write the manuscript using the JOET template provided in Hangul or MS Word format. Ensure that graphics are high-resolution. Be sure all necessary files have been uploaded/ attached.

Authors' checklist

Please refer to “Authors' Checklist” for details.

Article structure

Manuscript must be edited in the following order: (1) Title, (2) Authors' names and affiliations, (3) Keywords, (4) Abstract, (5) Nomenclature (optional), (6) Introduction, (7) Main body (analyses, tests, results, and discussions), (8) Conclusions, (9) Conflict of interest (optional), (10) Funding (optional), (11) Acknowledgements (optional), (12) References, (13) Appendices (optional), (14) Author’s ORCIDs.

Abstract

A concise and factual abstract is required. The abstract should state briefly the background, purpose and methods of the research, the principal results and conclusions. An abstract should be written in around 300 words. References are not cited in abstract whenever possible. Also, non-standard or uncommon abbreviations should be avoided, but if essential they must be defined at their first mention in the abstract itself.

Keywords

Immediately after the abstract, provide a maximum of 5 or 6 keywords.

Unit

Use the international system units(SI). If other units are mentioned, please give their equivalent in SI.

Equations

All mathematical equations should be c1early printed/typed using well accepted explanation. Superscripts and subscripts should be typed clearly above or below the base line. Equation numbers should be given in Arabic numerals enclosed in parentheses on the right-hand margin.

Tables

Tables should be numbered consecutively with Arabic numerals. Each table should be fully titled. All tables should be referred to in the texts.

Figures

Figures should be numbered consecutively with Arabic numerals. Each figure should be fully titled. All figures should be referred to in the texts. All the illustrations should be of high quality meeting with the publishing requirement with legible symbols and legends.

Conflict of interest

It should be disclosed here according to the statement in the Research and publication ethics regardless of existence of conflict of interest. If the authors have nothing to disclose, please state: “No potential

conflict of interest relevant to this article was reported."

Funding

Funding to the research should be provided here. Providing a FundRef ID is recommended including the name of the funding agency, country and if available, the number of the grant provided by the funding agency. If the funding agency does not have a FundRef ID, please ask that agency to contact the FundRef registry (e-mail: fundref.registry@crossref.org). Additional detailed policy of FundRef description is available from http://www.crossref.org/fundref/. Example of a funding description is as follows:

The study is supported by the Inha University research fund (FundRef ID: 10.13039/501100002632), and the Korea Health Personnel Licensing Examination Institute research fund (FundRef ID: 10.13039/501100003647).

Acknowledgments

Any persons that contributed to the study or the manuscript, but not meeting the requirements of an authorship could be placed here. For mentioning any persons or any organizations in this section, there should be a written permission from them.

References in text

References in texts follow the APA style. Authors can also see how references appear in manuscript text through the 'Template'.

Reference list

Reference list follows the APA style. Authors can see how references should be given in reference section through the 'Template'.

Appendices

The appendix is an optional section that can contain details and data supplemental to the main text. If there is more than an appendix, they should be identified as A, B, C, etc. Formulae and equations in appendices should be given separate numbering: Eq. (A1), Eq. (A2), etc.; in a subsequent appendix, Eq. (B1) and so on. Similarly for tables and figures: Table A1; Fig. A1, etc.

ORCID (Open Researcher and Contributor ID)

All authors are recommended to provide an ORCID. To obtain an ORCID, authors should register in the ORCID web site: http://orcid.org. Registration is free to every researcher in the world. Example of ORCID description is as follows:

Joonmo Choung: https://orcid.org/0000-0003-1407-9031

Peer review and publication process

The peer review process can be broadly summarized into three groups: author process, review process, and publishing process for accepted submissions. General scheme is presented in Figure 1.

Check-in process for review

If the manuscript does not fit the aims and scope of the Journal or does not adhere to the Instructions to Authors, it may be rejected immediately after receipt and without a review. Before reviewing, all submitted manuscripts are inspected by Similarity Check powered by iThenticate (https://www.crossref.org/services/similarity-check/), a plagiarism-screening tool. If a too high degree of similarity score is found, the Editorial Board will do a more profound content screening.

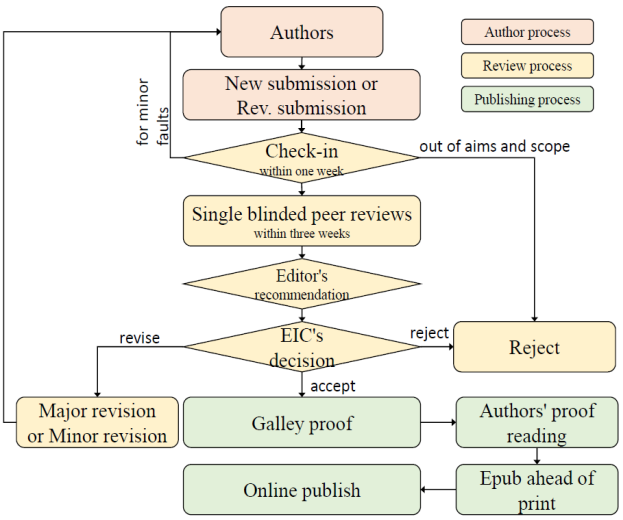

Figure 1 Flow chart of the peer review and publication process of JOET

The criterion for similarity rate for further screening is usually 15%; however, rather than the similarity rate, the Editorial Board focuses on cases where specific sentences or phrases are similar. The settings for Similarity Check screening are as follows: It excludes quotes, bibliography, small matches of 6 words, small sources of 1%, and the Methods section.

Number of reviewers

Reviewers will be selected from the list of reviewers. Manuscripts are then peer reviewed by at least 2 experts in the corresponding field, usually by 2.

Peer review process and the author response to the reviewer comments

JOET adopts single blind review, which means that the authors do not know the identity of the reviews. All papers, including those invited by the Editor, are subject to peer review.

The review period is 4 weeks. Usually the first decision is made within a week after completion of the review. The Editorial Board's decision after the review will be one of followings: Accept, Minor revision, Major revision, or Rejection. The Editorial Board may request the authors to revise the manuscript according to the reviewers' comments. If there are any requests for revision of the manuscript by the reviewers, the authors should do their best to revise the manuscript. If the reviewer's opinion is not acceptable or is believed to misinterpret the data, the author should reasonably indicate that. After revising the manuscript, the author should upload the revised files with a separate response sheet to each item of the reviewer's commentary. The author's revisions should be completed within 3 months after the request. If it is not received by the due date, the Editorial Board will notify the author. To extend the revision period beyond 3 months, the author should negotiate that with the Editorial Board. The manuscript review process can be provided for up two rounds. If the authors wish further review, the Editorial Board may consider it. The Editorial Board will make a final decision on the approval of the submitted manuscript for publication and can request any further corrections, revisions, and deletions of the article text if necessary. Statistical editing is also performed if the data requires professional statistical review by a statistician.

Processing after acceptance

If the manuscript is finally accepted, the galley proof will be sent to the corresponding author after professional manuscript editing and English proofreading. Proofreading should be performed for any misspellings or errors by the authors. Proofreading manuscript for publication is provided to the corresponding author, and the corresponding author must review the proofreading manuscript. Corresponding authors are responsible for the content of the proofreading manuscript and any errors. After final proofreading, the manuscript may appear at the journal homepage as an article in press with a unique DOI number for rapid communication. All published articles will be replaced by the replacement XML file and a final PDF.

Feedback after publication

If the authors or readers find any errors, or contents that should be revised, it can be requested from the Editorial Board. The Editorial Board may consider erratum, corrigendum or a retraction. If there are any revisions to the article, there will be a CrossMark description to announce the final draft. If there is a reader's opinion on the published article with the form of Letter to the editor, it will be forwarded to the authors. The authors can reply to the reader's letter. Letter to the editor and the author's reply may be also published.

How the journal handle complaints and appeals

The policy of JOET is primarily aimed at protecting the authors, reviewers, editors, and the publisher of the journal. If not described below, the process of handling complaints and appeals follows the guidelines of the Committee of Publication Ethics available from: https://publicationethics.org/appeals

- *Who complains or makes an appeal?*

Submitters, authors, reviewers, and readers may register complaints and appeals in a variety of cases as follows: falsification, fabrication, plagiarism, duplicate publication, authorship dispute, conflict of interest, ethical treatment of animals, informed consent, bias or unfair/inappropriate competitive acts, copyright, stolen data, defamation, and legal problem. If any individuals or institutions want to inform the cases, they can send a letter via the contact page on our website: https://www.joet.org/about/contact.php. For the complaints or appeals, concrete data with answers to all factual questions (who, when, where, what, how, why) should be provided.

- *Who is responsible to resolve and handle complaints and appeals?*

The Editorial Board or Editorial Office is responsible for them. A legal consultant or ethics editor may be able to help with the decision making.

- *What may be the consequence of remedy?*

It depends on the type or degree of misconduct. The consequence of resolution will follow the guidelines of the Committee of Publication Ethics (COPE).

Article processing charge

Payment due

Article processing charge (APC) covers the range of publishing services JOET provides. This includes provision of online tools for editors and authors, article production and hosting, and customer services. Upon editorial acceptance of an article for the regular review service and upon submission of an article for the fast review service, the corresponding author will be notified that payment is due.

APC

The APC up to 6 pages is ₩200,000 (or ＄200) and ₩550,000 (or ＄550) for the for the regular and fast review services, respectively. An extra APC of $50 per page is charged for papers longer than 6 pages, No taxes are included in this charge. For the fast review service, an advance fee of ₩250,000 ($250) should be paid on submission.

Payment methods

Credit card payment can be made online using a secure payment form as soon as the manuscript has been editorially accepted. We will we send a receipt by email once payment has been processed. Please note that payment by credit card carries a surcharge of 10% of the total APC.

Invoice payment is due within 7 days of the manuscript receiving editorial acceptance. Receipts are available on request.

Journal of Ocean Engineering and Technology 00(0), 000-000, December, 2100
https://doi.org/10.26748/KSOE.2100.000
pISSN 1225-0767
eISSN 2287-6715

Original Research Article, Technical Article, Review Article, etc

Title of Article

Firstname Lastname[1], Firstname Lastname[2] and Firstname Lastname[3]

[1]*Professor, Department of OO, OO School, OO University, Busan, Korea*
[2]*Graduate Student, Department of OO, OO University, Seoul, Korea*
[3]*Senior Researcher, Department of OO, OO Engineering. Corp., Seoul, Korea*

KEY WORDS: Lumped mass line model, Explicit method, Steel lazy wave riser (provide a maximum of 5 or 6 keywords.)

ABSTRACT: *A concise and factual abstract is required. The abstract should state briefly the background, purpose and methods of the research, the principal results and conclusions. An abstract should be written in around 300 words. References are not cited in abstract whenever possible. Also, non-standard or uncommon abbreviations should be avoided, but if essential they must be defined at their first mention in the abstract itself.*

Nomenclature (Optional)

ITOC	Increment of total operating cost ($/yr)
LHV	Lower heating value (kJ/kg)
Pw	Power (kW)
T	Temperature (K)
V	Volume (m^3)
ρ	Density (kg/m^3)

1. Introduction

The introduction should briefly place the study in a broad context and highlight why it is important. It should define the purpose of the work and its significance. The current state of the research field should be reviewed carefully and key publications cited. Please highlight controversial and diverging hypotheses when necessary. Finally, briefly mention the main aim of the work and highlight the principal conclusions. As far as possible, please keep the introduction comprehensible to scientists outside your particular field of research.

2. General Information for Authors

2.1 Research and Publication Ethics

Authorship should be limited to those who have made a significant contribution to the conception, design, execution, or interpretation of the reported study. All those who have made significant contributions should be listed as co-authors. Where there are others who have participated in certain substantive aspects of the research project, they should be acknowledged or listed as contributors.

The corresponding author should ensure that all appropriate co-authors and no inappropriate co-authors are included on the paper, and that all co-authors have seen and approved the final version of the paper and have agreed to its submission for publication.

Details on publication ethics are found in the journal's website (http://joet.org/authors/ethics.php). For the policies on research and publication

Received 00 February 2100, revised 00 October 2100, accepted 00 October 2100
Corresponding author Firstname Lastname: +82-51-759-0656, e-mail@e-mail.com
It is a recommended paper from the proceedings of 2019 spring symposium of the Korea Marine Robot Technology (KMRTS).

ethics not stated in the Instructions, Guidelines on Good Publication (http://publicationethics.org/) can be applied.

2.2 Requirement for Membership

One of the authors who submits a paper or papers should be member of The Korea Society of Ocean Engineers (KSOE), except a case that editorial board provides special admission of submission.

2.3 Publication Type

Article types include scholarly monographs (original research articles), technical articles (technical reports and data), and review articles. The paper should have not been submitted to other academic journal. When part or whole of a manuscript was already published to conference papers, research reports, and dissertations, then the corresponding author should note it clearly in the manuscript.

Example: It is noted that this paper is revised edition based on proceedings of KAOST 2100 in Jeju.

2.4 Copyright

After published to JOET, the copyright of manuscripts should belong to KSOE. A transfer of copyright (publishing agreement) form can be found in submission website (http://www.joet.org).

2.5 Manuscript Submission

Manuscript should be submitted through the on-line submission website (http://www.joet.org). The date that manuscript was received through on-line website is the official date of receipt. Other correspondences can be sent by an email to the Editor in Chief or secretariat. The manuscript must be accompanied by a signed statement that it has been neither published nor currently submitted for publication elsewhere. The manuscript should be written in English or Korean. Ensure that online submission are in a standard word processing format. Corresponding author must write the manuscript using the JOET template provided in Hangul or MS Word format. Ensure that graphics are high-resolution. Be sure all necessary files have been uploaded/ attached.

2.5.1 Authoer's checklist

Authoer's checklist and Transfer of copyright can be found in submission hompage (http:/www.joet.org).

3. Manuscript

Manuscript must be edited in the following order: (1) Title, (2) Authors' names and affiliations, (3) Keywords, (4) Abstract, (5) Nomenclature (optional), (6) Introduction, (7) Main body (analyses, tests, results, and discussions), (8) Conclusions, (9) Conflict of interest (optional), (10) Funding (optional), (11) Acknowledgements (optional), (12) References, (13) Appendices (optional), (14) Author's ORCIDs.

3.1 Unit

Use the international system units(SI). If other units are mentioned, please give their equivalent in SI.

3.2 Equations

All mathematical equations should be clearly printed/typed using well accepted explanation. Superscripts and subscripts should be typed clearly above or below the base line. Equation numbers should be given in Arabic numerals enclosed in parentheses on the right-hand margin. The parameters used in equation must be defined. They should be cited in the text as, for example, Eq. (1), or Eqs. (1)–(3).

$$G_{GEV}(x;\mu,\sigma,\xi)=\begin{cases}\exp[-(1+\xi(x-\mu)/\sigma)^{-1/\xi}] & \xi\neq 0\\ \exp[-\exp(-(x-\mu)/\sigma)] & \xi=0\end{cases} \tag{1}$$

in which μ, σ, and ξ represent the location ("Shift" in figures), scale, and shape parameters, respectively.

3.3 Tables

Tables should be numbered consecutively with Arabic numerals. Each table should be typed on a separate sheet of paper and be fully titled. All tables should be referred to in the texts.

Table 1 Tables should be placed in the main text near to the first time they are cited

Item	Buoyancy riser
Segment length[1)] (m)	370
Outer diameter (m)	1.137
Inner diameter (m)	0.406
Dry weight (kg/m)	697
Bending rigidity ($N \cdot m^2$)	1.66E8
Axial stiffness (N)	7.098E9
Inner flow density ($kg \cdot m^3$)	881
Seabed stiffness ($N/m/m^2$)	6,000

[1)]Tables may have a footer.

3.4 Figures

Figures should be numbered consecutively with Arabic numerals. Each figure should be fully titled. All the illustrations should be of high quality meeting with the publishing requirement with legible symbols and legends. All figures should be referred to in the texts. They should be referred to in the text as, for example, Fig. 1, or Figs. 1−3.

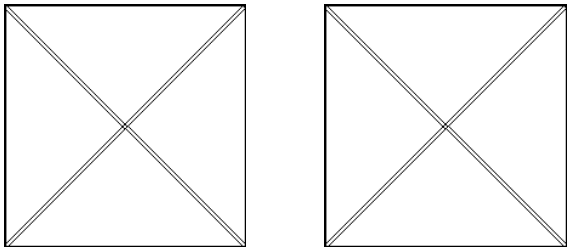

(a) Description of what is contained in the first panel

(b) Description of what is contained in the first panel

Fig. 1 Schemes follow the same formatting. If there are multiple panels, they should be listed as: (a) Description of what is contained in the first panel; (b) Description of what is contained in the second panel. Figures should be placed in the main text near to the first time they are cited

3.5 How to Describe the References in Main Texts

All references should be listed at the end of the manuscripts, arranged in order of Alphabet. References in texts follow the American Psychological Association (APA) style. The exemplary form of listed references is as follows:

Single author: (Kim, 1998) or Kim (1998)

Two authors: (Kim and Lee, 2000) or Kim and Lee (2000)

Three or more authors: (Kim et al., 1997) or Kim et al. (1997)

Two or more papers: (Lee, 1995a; Lee, 1995b; Ryu et al., 1998)

Year unknown: (Kim, n.d.) or Kim (n.d.)

4. Results

This section may be divided by subheadings. It should provide a concise and precise description of the experimental results, their interpretation as well as the experimental conclusions that can be drawn. Tables and figures are recommended to present the results more rapidly and easily. Do not duplicate the content of a table or a figure with in the Results section. Briefly describe the core results related to the conclusion in the text when data are provided in tables or in figures. Supplementary results can be placed in the Appendix.

5. Discussion

Authors should discuss the results and how they can be interpreted in perspective of previous studies and of the working hypotheses. The findings and their implications should be discussed in the broadest context possible. Future research directions may also be highlighted

6. Conclusions

This section can be added to the manuscript.

Conflict of Interest (Optional)

It should be disclosed here according to the statement in the Research and publication ethics regardless of existence of conflict of interest. If the authors have nothing to disclose, please state: “No potential conflict of interest relevant to this article was reported.”

Funding (Optional)

Please add: “This research was funded by Name of Funder, grant number XXX” and “The OOO was funded by XXX”. Check carefully that the details given are accurate and use the standard spelling of funding agency names at https://search.crossref.org/funding

Acknowledgments (Optional)

In this section you can acknowledge any support given which is not covered by the author contribution or funding sections. This may include administrative and technical support, or donations in kind (e.g., materials used for experiments). For mentioning any persons or any organizations in this section, there should be a written permission from them.

References

- Journal name should not be abbreviated.
- A private report with limited access or download availability can not be a reference.
- Include the digital object identifier DOI or URL for all references where available.
- Reference list follows the American Psychological Association (APA) style.

Referring to journal publications:

Author, A.A., Author, B.B., & Author, C.C. (Year). Title of Article. Journal Title, vol(no), pp–pp. https://doi.org/xx.xxxx/xxxxxx

Author, A.A., Author, B.B., Author, C.C. (accepted; in press). Title of Article. Title of Periodical. Retrieved from http://xx.xxx/x.pdf

Lee, T.K., Kim, T.W., Rim, C.W., & Kim, S.C. (2013). A Study on Calculation of Local Ice Pressures for ARAON Based on Data Measured at Arctic Sea. Journal of Ocean Engineering and Technology, 27(5), 88–92. https://doi.org/10.5574/KSOE.2013. 27.5.088

Lee, T.K., Kim, T.W., Rim, C.W., & Kim, S.C. (accepted; in press). A Study on Calculation of Local Ice Pressures for ARAON Based on Data Measured at Arctic Sea. Journal of Ocean Engineering and Technology, Retrieved from http://xxx.xxx/xxx.pdf

Referring to conference proceedings:

Author, A.A., Author, B.B., & Author, C.C. (Year). Title of Article. Proceeding Title, City, Country, pp–pp. https://doi.org/xx.xxxx

Aoki, S., Liu, H., & Sawaragi, T. (1994). Wave Transformation and Wave Forces on Submerged Vertical Membrane. Proceedings of International Symposium Waves - Physical and Numerical Modeling, Vancouver, Canada, 1287–1296.

Tsukamoto, C.L., Lee, W., Yuh, J., Choi, S.K., & Lorentz, J. (1997). Comparison Study on Advanced Thruster Control of Underwater Robots. Proceedings of International Conference on Robotics and Automation, 1845–1850. https://doi.org/110.1109/ROBOT.1997.619056

Referring to books:

Author, A.A. (Year). Title of Book (xx ed.). Location: Publisher.

Strunk, W., & White, E.B. (2000). The Elements of Style (4th ed.). NewYork, USA: Longman.

Schlichting, H. (1968). Boundary Layer Theory (6th ed.). New York, USA: McGraw-Hill.

Referring to theses or dissertations:

Author, A.A. (Year). Title of Doctoral Dissertation or Master’s thesis (Doctoral Dissertation or Master’s thesis). Name of Institution, City, Country.

Giovanni, I. (1998). Modelling and Identification of Underwater Robotic Systems (Ph.D. Thesis). University of Genova, Genova, Italy.

Referring to technical reports, rules, or guidelines:

Author, A.A. (Year). Title of report (Reprot No. xxx), Location: Publisher.

Likhomanov, V. (2010). Full-Scale Ice Trials of the Korean Research Icebreaker ARAON. Daejeon, Korea: Arctic and Antarctic Research Institute (AARI).

ABS. (2011). Guide for Ice Loads Monitoring Systems. Houston, USA: American Bureau of Shipping.

Lloyd's Register. (2011). FDA ICE Fatigue Induced by Ice Loading, ShipRight Design and construction - Fatigue Design Assesment. London, United Kingdom: Lloyd's Register.

Larson, M., & Kraus, N.C. (1989). SBEACH: Numerical Model for Simulating Storm-Induced Beach Change - Report 1 Empirical Foundation and Model Development (Technicla Report CERC-89-9). Coastal Engineering research center Vicksburg Ms.

Referring to patents:

Righsholder, A.A. (Year). Title of Patent. Patent number, Patent office with country.

Dawoo Shipbulding & Maringe Engineering (DSME). (2013). Distance Length Standardization Method for Preventing Interference at the time of Uploading Cell Guide of Container Ship. Unexamined Patent Publication 1020130044635, Korean Interllectual Property Office.

Referring to websites:

Righsholder, A.A. (Year). Title of webpage. Retrieved Month Year from http://xxxx

International Association of Classification Societies (IACS). (2010a). Common Structural Rules for Bulk Carriers. Retrieved July 2010 from http://www.iacs-data.org.uk

US Congressional Hearing. (2009). Strategic Importance of the Arctic in Us Policy. Retrieved June 2019 from https://fas.org/irp/arctic.pdf

Dawoo Shipbulding & Maringe Engineering (DSME). (2013). Distance Length Standardization Method for Preventing Interference at the time of Uploading Cell Guide of Container Ship. Retrieved June 2019 from https://patentimages.storage./pdfs/792.pdf

Referring to software:

Righsholder, A.A. (Year). Title of Software. Downloaded Month Year from http://xxxx

Standard

Organization. (Year). Title of the standard in italics [Translated title − if applicable] (Standard No.). Retrieved from https://...

International Organization for Standardization. (2005). Industrial sewing machines: Safety requirements for sewing machines, units and systems (ISO Standard No. 10821). Retrieved from http://www.standard.no/no/Nettbutikk/produktkatalogen/Produktpresentasjon/?ProductID=113554

Translation

Author, A. A. (Year of publication). Title of work: Capital letter also for subtitle (T. Translator, Trans.). Location: Publisher. (Original work published YEAR). DOI

Ura, T., & Takakawa, S. (2015). All about Submersibles (W.S. Kim, D.S. Kim, Y.H. Choi,.C.H. Park, J.S. Park, P.M. Lee, H.S. Jung, Trans.). Korea: CIR. (Original Work Published in 1994, Japan: Seizan-Shoten Publiching)

in text: (Ura and Takakawa, 1994/2015)

Referring to some exceptional cases:

- when authors are missing, institution can replace authors

National Oceanic and Atmospheric Administration (NOAA). (2015). Deep-ocean Assessment and Reporting of Tsunamis (DART). Retrieved December 2019 from https://nctr.pmel.noaa.gov/Dart/

- when dates or years are missing, it is replaced with "n.d."

National Oceanic and Atmospheric Administration (NOAA). (n.d.). Deep-ocean Assessment and Reporting of Tsunamis (DART).

- when more then seven authors, first 6 authors ... last author.

Yeu, T., Choi, H.T., Lee, Y., Chae, J., Lee, Y., Kim, S.S., ... Lee, T.H. (2019). Development of Robot Platform for Autonomous Underwater Intervention. Journal of Ocean Engineering and Technology, 33(2), 168−177. https://doi.org/10.26748/KSOE. 2019.021

Appendix (Optional)

The appendix is an optional section that can contain details and data supplemental to the main text. For example, explanations of experimental details that would disrupt the flow of the main text, but nonetheless remain crucial to understanding and reproducing the research shown; figures of replicates for experiments of which representative data is shown in the main text can be added here if brief, or as Supplementary data. Mathematical proofs of results not central to the paper can be added as an appendix.

All appendix sections must be cited in the main text. In the appendixes, Figures, Tables, etc. should be labeled starting with 'A', e.g., Fig. A1, Fig. A2, etc.

Examples:

https://doi.org/10.26748/KSOE.2019.022

https://doi.org/10.26748/KSOE.2018.4.32.2.095

Author ORCIDs

All authors are recommended to provide an ORCID. To obtain an ORCID, authors should register in the ORCID web site: http://orcid.org. Registration is free to every researcher in the world. Example of ORCID description is as follows:

Author name	ORCID
So, Hee	0000-0000-000-00X
Park, Hye-Il	0000-0000-000-00X
Yoo, All	0000-0000-000-00X
Jung, Jewerly	0000-0000-000-00X

Authors' Checklist

The following list will be useful during the final checking of a manuscript prior to sending it to the journal for review. Please submit this checklist to the KSOE when you submit your article.

< Checklist for manuscript preparation >

☐ I checked my manuscript has been 'spell-checked' and 'grammar-checked'.
☐ One author has been designated as the corresponding author with contact details such as
- E-mail address
- Phone numbers

☐ I checked abstract 1) stated briefly the purpose of the research, the principal results and major conclusions, 2) was written in around 300 words, and 3) did not contain references (but if essential, then cite the author(s) and year(s)).
☐ I provided 5 or 6 keywords.
☐ I checked color figures were clearly marked as being intended for color reproduction on the Web and in print, or to be reproduced in color on the Web and in black-and-white in print.
☐ I checked all table and figure numbered consecutively in accordance with their appearance in the text.
☐ I checked abbreviations were defined at their first mention there and used with consistency throughout the article.
☐ I checked all references mentioned in the Reference list were cited in the text, and vice versa according to the APA style.
☐ I checked I used the international system units (SI) or SI-equivalent engineering units.

< Authorship checklist >

JOET considers individuals who meet all of the following criteria to be authors:

☐ Made a significant intellectual contribution to the theoretical development, system or experimental design, prototype development, and/or the analysis and interpretation of data associated with the work contained in the article.
☐ Contributed to drafting the article or reviewing and/or revising it for intellectual content.
☐ Approved the final version of the article as accepted for publication, including references.

< Checklist for publication ethics >

☐ I checked the work described has not been published previously (except in the form of an abstract or as a part of a published lecture or academic thesis).
☐ I checked when the work described has been published previously in other proceedings without copyright, it has clearly noted in the text.
☐ I checked permission has been obtained for use of copyrighted material from other sources including the Web.
☐ I have processed Plasgiarism Prevention Check through reliable web sites such as www.kci.go.kr, http://www.ithenticate.com/, or https://www.copykiller.org/ for my submission.
☐ I agree that final decision for my final manuscript can be changed according to results of Plasgiarism Prevention Check by JOET administrator.
☐ I checked one author at least is member of the Korean Society of Ocean Engineers.
☐ I agreed all policies related to 'Research and Publication Ethics'
☐ I agreed to transfer copyright to the publisher as part of a journal publishing agreement and this article will not be published elsewhere including electronically in the same form, in English or in any other language, without the written consent of the copyright-holder.
☐ I made a payment for reviewing of the manuscript, and I will make a payment for publication on acceptance of the article.
☐ I have read and agree to the terms of Authors' Checklist.

Title of article	:	
Date of submission	: DD/MM/YYYY	
Corresponding author	:	signature
Email address	:	

※ E-mail this with your signature to ksoehj@ksoe.or.kr

Publishing Agreement

ARTICLE DETAILS

Title of article :

Corresponding author :

E-mail address :

DOI : https://doi.org/10.26748/KSOE.2XXX.XXX

YOUR STATUS

I am one author signing on behalf of all co-authors of the manuscript.

ASSIGNMENT OF COPYRIGHT

I hereby assign to the Korean Society of Ocean Engineers, the copyright in the manuscript identified above and any tables, illustrations or other material submitted for publication as part of the manuscript (the "Article"). This assignment of rights means that I have granted to Korean Society of Ocean Engineers the exclusive right to publish and reproduce the Article, or any part of the Article, in print, electronic and all other media (whether now known or later developed), in any form, in all languages, throughout the world, for the full term of copyright, and the right to license others to do the same, effective when the Article is accepted for publication. This includes the right to enforce the rights granted hereunder against third parties.

SCHOLARLY COMMUNICATION RIGHTS

I understand that no rights in patents, trademarks or other intellectual property rights are transferred to the Journal owner. As the author of the Article, I understand that I shall have: (i) the same rights to reuse the Article as those allowed to third party users of the Article under the CC-BY-NC License, as well as (ii) the right to use the Article in a subsequent compilation of my works or to extend the Article to book length form, to include the Article in a thesis or dissertation, or otherwise to use or re-use portions or excerpts in other works, for both commercial and non-commercial purposes. Except for such uses, I understand that the assignment of copyright to the Journal owner gives the Journal owner the exclusive right to make or sub-license commercial use.

USER RIGHTS

The publisher will apply the Creative Commons Attribution-Noncommercial Works 4.0 International License (CC-BY-NC) to the Article where it publishes the Article in the journal on its online platforms on an Open Access basis.
The CC-BY-NC license allows users to copy and distribute the Article, provided this is not done for commercial purposes and further does not permit distribution of the Article if it is changed or edited in any way, and provided the user gives appropriate credit (with a link to the formal publication through the relevant DOI), provides a link to the license, and that the licensor is not represented as endorsing the use made of the work. The full details of the license are available at http://creativecommons.org/licenses/by-nc/4.0/legalcode.

REVERSION OF RIGHTS

Articles may sometimes be accepted for publication but later rejected in the publication process, even in some cases after public posting in "Articles in Press" form, in which case all rights will revert to the author.

☑ I have read and agree to the terms of the Journal Publishing Agreement.

Corresponding author:

name signature

※ E-mail this with your signature to ksoehj@ksoe.or.kr (Papers will not be published unless this form is signed and returned)

2021년도 한 해 동안 한국해양공학회지에 투고된 원고를 심사하신 분들입니다.
심사위원 여러분께 감사드립니다.

강충현	경상국립대학교	**박영호**	창원대학교	**윤상준**	삼성중공업
강태순	㈜지오시스템리서치	**박영환**	부산대학교	**윤현규**	창원대학교
강희진	KRISO	**박정희**	고려대학교	**이강수**	KRISO
공유식	부경대학교	**박종용**	부경대학교	**이순섭**	경상국립대학교
구본국	창원대학교	**박종천**	부산대학교	**이승재**	한국해양대학교
구원철	인하대학교	**박종호**	성균관대학교	**이우동**	경상국립대학교
김국현	동명대학교	**박준수**	경남대학교	**이종락**	KRISO
김도균	서울대학교	**박지용**	KRISO	**이종무**	KRISO
김범일	한국선급	**박진영**	KRISO	**이탁기**	경상국립대학교
김성재	인하대학교	**배윤혁**	제주대학교	**장범선**	서울대학교
김연중	인제대학교	**백광준**	인하대학교	**전봉환**	KRISO
김영식	KRISO	**서대원**	한국선급	**전석희**	대우조선해양
김영훈	경남대학교	**서정관**	부산대학교	**정광효**	부산대학교
김윤해	한국해양대학교	**서정화**	충남대학교	**정상기**	한국해양대학교
김윤호	KRISO	**송기수**	한국해양대학교	**정석호**	창원대학교
김정록	제주대학교	**송창용**	목포대학교	**정성준**	KRISO
김정환	동아대학교	**신성원**	한양대학교	**정세민**	조선대학교
김종규	전남대학교	**신성철**	부산대학교	**정재환**	삼성중공업
김준영	한국해양대학교	**신승호**	KRISO	**조낙균**	서울대학교
김진욱	재료연구원	**안석환**	중원대학교	**진충국**	Texas A&M
김진환	KAIST	**안현정**	KRISO	**진태석**	동서대학교
김현식	동명대학교	**양경규**	KRISO	**최영명**	부산대학교
남보우	서울대학교	**양해상**	서울대학교	**최형식**	한국해양대학교
도기덕	한국해양대학교	**여태경**	KRISO	**추영민**	세종대학교
류용욱	전남대학교	**오대균**	목포해양대학교	**하태민**	강원대학교
박선호	한국해양대학교	**오민한**	현대중공업	**함승호**	창원대학교
박성주	인하대학교	**오승훈**	KRISO	**허선철**	경남대학교
박승민	(주)혜인이엔씨	**유재석**	DGIST	**황성철**	KRISO

(사)한국해양공학회 특별회원

한국해양공학회의 특별회원은 다음과 같으며, 귀사의 찬조에 진심으로 감사드립니다.(순서: 입회순)

한국선급 / 현대중공업(주) / 대우조선해양(주) /
한국해양과학기술원 부설 선박해양플랜트 연구소 / 대양전기공업(주) /
한국조선해양기자재연구원 / 한국조선해양플랜트협회 / 주식회사 파나시아 /
선보공업(주) / 에스케이에코플랜트 주식회사 / ㈜대영엔지니어링 /
㈜멀티스하이드로 / ㈜유에스티 21 / ㈜해양정보기술

한국해양공학회 특별회원 가입방법은 학회홈페이지(www.ksoe.or.kr)의
입회안내를 참고하시고, 기타사항은 학회 사무국으로 연락주시기 바랍니다.

Research and Publication Ethics

Journal of Ocean Engineering and Technology (JOET) adheres to the guidelines published by professional organizations, including Committee on Publication Ethics (COPE; https://publicationethics.org/)

1. Authorship

JOET considers individuals who meet all of the following criteria to be authors:

1) Made a significant intellectual contribution to the theoretical development, system or experimental design, prototype development, and/or the analysis and interpretation of data associated with the work contained in the article.
2) Contributed to drafting the article or reviewing and/or revising it for intellectual content.
3) Approved the final version of the article as accepted for publication, including references.

Contributors who do not meet all of the above criteria may be included in the Acknowledgment section of the article. Omitting an author who contributed to your article or including a person who did not fulfill all of the above requirements is considered a breach of publishing ethics.

Correction of authorship after publication: JOET does not correct authorship after publication unless a mistake has been made by the editorial staff.

2. Originality and Duplicate Publication

All submitted manuscripts should be original and should not be in consideration by other scientific journals for publication. Any part of the accepted manuscript should not be duplicated in any other scientific journal without permission of the Editorial Board, although the figures and tables can be used freely if the original source is verified according to the Creative Commons Attribution License (CC BY-NC). It is mandatory for all authors to resolve any copyright issues when citing a figure or table from other journal that is not open access.

3. Conflict-of-Interest Statement

Conflict of interest exists when an author or the author's institution, reviewer, or editor has financial or personal relationships that inappropriately influence or bias his or her actions. Such relationships are also known as dual commitments, competing interests, or competing loyalties. These relationships vary from being negligible to having a great potential for influencing judgment. Not all relationships represent true conflict of interest. On the other hand, the potential for conflict of interest can exist regardless of whether an individual believes that the relationship affects his or her scientific judgment. Financial relationships such as employment, consultancies, stock ownership, honoraria, and paid expert testimony are the most easily identifiable conflicts of interest and the most likely to undermine the credibility of the journal, the authors, or of the science itself. Conflicts can occur for other reasons as well, such as personal relationships, academic competition, and intellectual passion. If there are any conflicts of interest, authors should disclose them in the manuscript. The conflicts of interest may occur during the research process as well; however, it is important to provide disclosure. If there is a disclosure, editors, reviewers, and reader can approach the manuscript after understanding the situation and the background of the completed research.

4. Management Procedures for the Research and Publication Misconduct

When JOET faces suspected cases of research and publication misconduct such as a redundant (duplicate) publication, plagiarism, fabricated data, changes in authorship, undisclosed conflicts of interest, an ethical problem discovered with the submitted manuscript, a reviewer who has appropriated an author's idea or data, complaints against editors, and other issues, the resolving process will follow the flowchart provided by the Committee on Publication Ethics (http://publicationethics.org/resources/flowcharts). The Editorial Board of JOET will discuss the suspected cases and reach a decision. JOET will not hesitate to publish errata, corrigenda, clarifications, retractions, and apologies when needed.

5. Editorial Responsibilities

The Editorial Board will continuously work to monitor and safeguard publication ethics: guidelines for retracting articles; maintenance of the integrity of the academic record; preclusion of business needs from compromising intellectual and ethical standards; publishing corrections, clarifications, retractions, and apologies when needed; and excluding plagiarism and fraudulent data. The editors maintain the following responsibilities: responsibility and authority to reject and accept articles; avoiding any conflict of interest with respect to articles they reject or accept; promoting publication of corrections or retractions when errors are found; and preservation of the anonymity of reviewers.

6. Hazards and human or animal subjects

If the work involves chemicals, procedures or equipment that have any unusual hazards inherent in their use, the author must clearly identify these in the manuscript. If the work involves the use of animal or human subjects, the author should ensure that the manuscript contains a statement that all procedures were performed in compliance with relevant laws and institutional guidelines and that the appropriate institutional committee(s) has approved them. Authors should include a statement in the manuscript that informed consent was obtained for experimentation with human subjects. The privacy rights of human subjects must always be observed.

Ensure correct use of the terms sex (when reporting biological factors) and gender (identity, psychosocial or cultural factors), and, unless inappropriate, report the sex and/or gender of study participants, the sex of animals or cells, and describe the methods used to determine sex and gender. If the study was done involving an exclusive population, for example in only one sex, authors should justify why, except in obvious cases. Authors should define how they determined race or ethnicity and justify their relevance.

7. Secondary publication

It is possible to republish manuscripts if the manuscripts satisfy the conditions of secondary publication. These are:

- The authors have received approval from the Editorial Board of both journals (the editor concerned with the secondary publication must have access to the primary version).
- The priority for the primary publication is respected by a publication interval negotiated by editors of both journals and the authors.
- The paper for secondary publication is intended for a different group of readers
- The secondary version faithfully reflects the data and interpretations of the primary version.
- The secondary version informs readers, peers, and documenting agencies that the paper has been published in whole or in part elsewhere, for example, with a note that might read, "This article is based on a study first reported in the [journal title, with full reference]"
- The title of the secondary publication should indicate that it is a secondary publication (complete or abridged republication or translation) of a primary publication.

8. Complaints and Appeals

The process of handling complaints and appeals follows the guidelines of the COPE available from: https://publicationethics. org/appeals

9. Post-publication discussions and corrections

The post-publication discussion is available through letter to editor. If any readers have a concern on any articles published, they can submit letter to editor on the articles. If there found any errors or mistakes in the article, it can be corrected through errata, corrigenda, or retraction.

The Korean Society of Ocean Engineers